Dissertation Advisor:
Professor Pablo Jarillo-Herrero

Author:
Patrick Kenichi Herring

LOW DIMENSIONAL CARBON ELECTRONICS

Abstract

This thesis covers several different experiments that comprised my graduate career. The main focus of these experiments was the use of carbon as an electronic material and a steady evolution of fabrication recipes that allowed us to perform reliable and consistent measurements. The second chapter describes experiments with carbon nanotubes, where our goal was to produce devices capable of manipulating electronic spin states in order create quantum bits or "qubits." The third chapter covers the development of fabrication recipes with the goal of creating qubits within Si-Ge nanowire, and the bottom-gating approach that was developed. The fourth chapter begins graphene related research, describing one of the simplest uses of graphene as a simple transparent electrode on a SiN micromembrane. The remainder of the thesis describes experiments that develop graphene based optical and infrared detectors, study their characteristics and determine the physics that underlies their detection mechanism. Key in these experiments were the fabrication recipes that had been developed to create carbon nanotube and Si-Ge nanowire devices. Finally, we demonstrate how engineering of the device's thermal characteristics can lead to improved sensitivity and how graphene can be used in novel applications where conventional materials are not suitable.

Contents

List of Figures

Citations to Previously Published Work

Chapter 4 of this thesis has been adapted from:

"Single-layer graphene on silicon nitride micromembrane resonators"

Silvan Schmid, Tolga Bagci, Emil Zeuthen, Jacob M. Taylor, Patrick K. Herring, Maja C. Cassidy, Charles M. Marcus, Luis Guillermo Villanueva, Bartolo Amato, Anja Boisen, Yong Cheol Shin, Jing Kong, Anders S.Sørensen, Koji Usami, and Eugene S. Polzik

Journal of Applied Physics **115**, 054513 (2014)

Parts of Chapter 6 of this thesis appeared previously in:

"Photoresponse of an Electrically Tunable Ambipolar Graphene Infrared Thermocouple"

Patrick K. Herring, Allen L. Hsu, Nathaniel M. Gabor, Yong Cheol Shin, Jing Kong, Tomás Palacios, Pablo Jarillo-Herrero

Nano Lett., **2014**, *14* (2), pp 901–907

Acknowledgements

No physicist works in a perfect vacuum, and I am no exception. I owe a lot to my fellow graduate students, post-docs and professors. In particular, Allen Hsu has been instrumental in the Mid-IR experiments, both in analyzing data, measuring, and fabricating devices. Nathaniel Gabor, the post-doc who got me started with graphene optoelectronic devices and supplied a lot of the ideas for experiment and subsequent analysis. Qiong Ma, who helped me run a lot of the initial optical experiments and learn how to use the setup. Javier Sanchez-Yamagishi acquainted me with a lot of the lab made me feel welcome, and provided a lot of helpful tips on fabricating graphene devices. Valla Fatemi provided a lot of useful conversations regarding fabrication and future career planning, and was working in Charles Marcus' lab as the lab was moving. Monica Wolf for making me feel like part of the group and sorting out all of the difficult forms and financial details necessary for me to work at MIT and in the group. And of course, Pablo Jarillo-Herrero, who guided me through the final portion of my graduate career and provided a lot of the most important lessons on how to be a scientist.

In the first half of my graduate school education, I am especially indebted to Hugh Churchill for teaching me so many different fabrication techniques and his patience as I learned about how to work as a graduate student. Maja Cassidy and Jim Medford were a source of encouragement and friendship through the toughest times as I worked to find a path forward, and provided mental sanity in a crazy time of my life.

Charles Marcus, as my advisor for the first part of my graduate career taught me a lot about hard work and the ambitious nature of research. Amir Yacoby, who was a constant throughout my PhD, and provided the continuity and encouragement that I needed to finish my thesis work and confidence to step out into the world. Carolyn Moore, for helping me to sort out all of the necessary details as I worked toward my thesis defense. Bertrand Halprin, for sitting on my committee during the change-over process.

I would like to especially thank my family for all of their help and support during my journey through graduate school. I would never have become a scientist without my father's influence, constantly providing encyclopedic knowledge of science and engineering, showing me the way. My mother's tutoring gave me the drive and discipline to get me where I am. My sister Marie, for seeing my through the entire time I was at Harvard and connecting me to so many of the people that have made graduate school a fun time. My brother George, for his constant conversations on electrical engineering, popular science and the coolest developments in technology, giving me constant motivation to work on new and interesting problems. I owe the most to my fiancé, Kimberly Le, for her patience, encouragement and advice on how to handle everything during one of the more stressful times of my life. Without her this thesis might never have been written.

Dedicated to Kim

Chapter 1

1. Introduction

1.1 Introduction and Foreword

My graduate work has focused in large part on the use of carbon as an electronic material. In particular, the first 2-3 years of my work focused on carbon nanotube quantum dots, while the last 3-4 years has focused on graphene as an infrared detection material. Throughout this process it has been necessary to engineer the materials properties and fabrication recipes to eliminate unwanted impurities, reduce doping, increase the control or create a more advantageous geometry, among a host of other characteristics. It has also been important to engineer or create experimental setups that allow simple and effective measurements to be made with a minimum of difficulty. Although this kind of work rarely results in publications or recognition, I have found it to be the more rewarding and interesting part of my research. As a result this thesis will focus on many of the fabrication and experimental details that have gone into my experiments. I believe that this best reflects the material and overall focus of my graduate career.

Carbon is one of the most important and versatile elements from both a materials science perspective and a chemistry perspective. Its use in chemical structures ranges from simple molecules to polymers and protein structures of immense complexity. Its utility stems in part from the strength of its covalent bond and its hybridization allowing the formation of chains [1]. Carbon based structures such as fullerenes and nanotubes are often referred to as molecular electronics since they occupy a regime between bulk semiconductor devices and single atoms with sizes of just a few nanometers [2]. They have been studied for several decades, both for their electronic and for their mechanical properties and their ability to realize unique physics. Initially they were synthesized in a haphazard manner, with desirable structures in the midst of amorphous carbon masses. Additionally, these carbon structures had a wide distribution of sizes and number of walls, consisting of nested shells of carbon.

The development of better growth techniques with deposited catalyst pads allowed the growth of single walled carbon nanotubes (SWNT) with a relatively small distribution of diameters [3]. The basic technique involves a metallic or metal complex catalyst and a gaseous precursor that breaks down upon interaction with the catalyst particle. This interaction requires very high temperatures (~1000°C) for breakdown of the gaseous precursor, usually methane. Growth times are typically on the order of 10-30 minutes at atmospheric pressure. While the furnace is heating, flowing Ar through the growth chamber maintains an Ar atmosphere free of O_2. Since simple tube furnaces can reach these temperatures and pressures, growth of nanotubes can be done

with inexpensive equipment and supplies. Other materials that are often studied as next generation electronics, such as gallium arsenide 2D electron gases, require growth with molecular beam epitaxy systems that are far more complex, expensive and difficult to maintain [4].

In a similar manner it is possible to grow a single atomic layer of graphite, referred to as graphene, with simple tube furnaces. This growth is typically done on a copper foil that serves as the supporting substrate during growth and acts as the catalytic metal, as shown in Figure 1.1, for breakdown of the methane (or other carbon compound) feedstock [5]. Growth is also done around 1000°C but usually at reduced pressures, as a way of controlling the growth rate and individual crystal sizes [6].

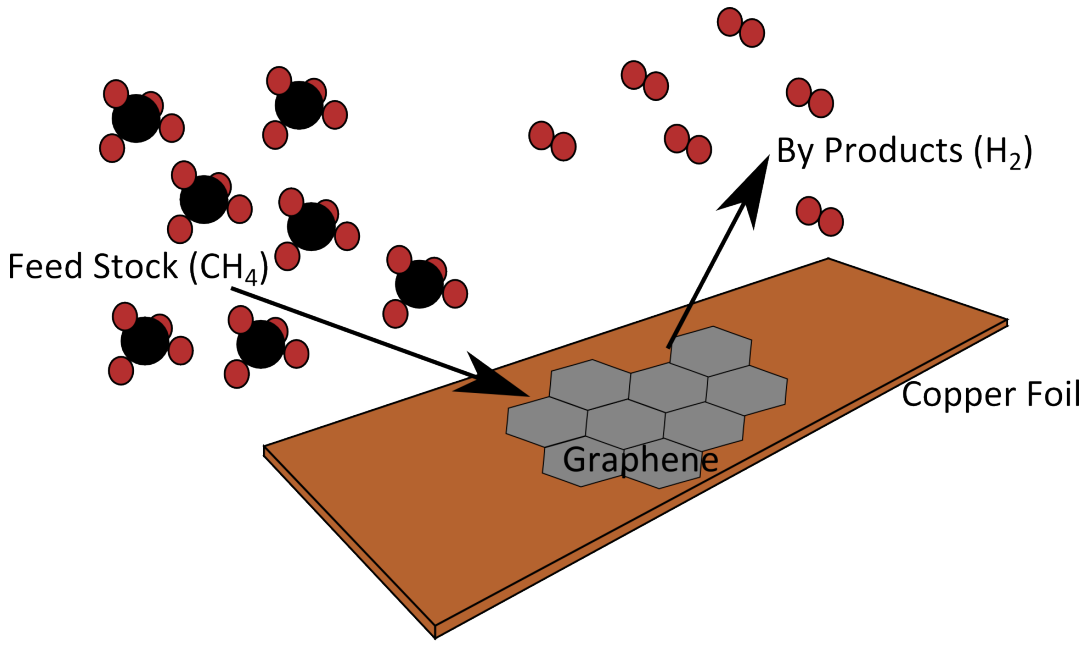

Figure 1.1 Schematic of Graphene Growth Mechanism
The carbon feed stock is broken down catalytically on the surface of the copper foil substrate, the carbon nucleates and forms graphene while the gaseous by-products are carried away in the gas stream.

It is possible to characterize the resulting carbon structures with transmission electron microscopy (TEM) and determine diameter, number of walls or layers and size of the grown structures. Unfortunately this method can easily cause contamination or damage to the nanotubes, to the extent that it is generally considered a destructive imaging technique. Performing TEM imaging also requires transfer to a substrate that allows the transmission of the electron beam, usually a thin carbon or SiN membrane. As a result TEM is not a preferred method for characterizing nanotubes prior to electrical measurements. A far less destructive and non-invasive technique is atomic force microscopy, which uses a nanostructured tip to tap along the surface of a wafer and measure the vertical displacement of that tip. This method of measurement can also be used to introduce bends and kinks into carbon nanotubes, either creating defects or bends within the structure [7].

The relative ease with which carbon electronics can be grown is one of the reasons that they are an attractive area of research. A simple setup with a cost of a few thousand dollars can allow a researcher to grow electronics with dimensions of just a couple of nanometers, far beyond the current size of lithographically defined commercial structures. The parameters of these electronics potentially far exceed the current technology. For instance, a far higher transconductance and smaller charging energy for these devices imply lower energy consumption for each computational operation [8]. Due to increasing energy costs, computation might be one of the most important applications for future carbon electronics. Additionally, the superior thermal

characteristics of carbon electronics could be useful in high temperature and harsh environments.

Other potential applications of carbon nanotubes involve their 1D nature. One promising direction is the use of carbon nanotubes mats as flexible, transparent electrodes that can be deposited on a wide variety of substrates and materials. This class of electrodes is a significant improvement over other transparent bulk conductors such as indium tin oxide (ITO) that are brittle or exhibit fatigue failure with repeated mechanical flexure [9]. The nanotubes can be grown on a SiO_2 substrate material and then suspended in a solution by sonicating the substrate chip in a methanol or similar solvent. This suspension can then be spun onto a chip and allowed to dry, creating a dense mat of carbon nanotubes. By using standard liftoff techniques the mat can be patterned into antennas, interconnects, etc. It is also possible to pattern via oxygen-plasma etching techniques although care must be taken during this process avoid over etching the mask and destroying the underlying layer.

Graphene has also been advanced as a promising candidate for flexible electronics although its sheet-like nature means that it is not as mechanically durable as a carbon nanotube mat. It does, however, have the ability to form much more reliable and complex electronics than is possible from the carbon nanotube mats [10]. An additional possibility would be to create graphene devices or sensors and then use a carbon nanotube mat for the electrical interconnects.

In the carbon nanotube experiments that I preformed we were interested primarily in the high level of confinement that the 1D nature of a carbon nanotube

offers. The fact that the electrons are confined in the lateral dimension to a very high degree means that you can create an electronic "box" by only supplying confinement along the length of the nanotube. By creating an electronic box small enough, the allowed states of the electrons in the box become quantized with spacing larger than the thermal distribution of energies. This confinement allows for the control of single electrons within sections of the nanotube, soley via the electrostatic influence of gates. The control and manipulation of electrons with applied voltages is one of the main advantages for this class of quantum dots. Applications of quantum dots include devices such as single photon sources, quantum bits (qubits) and sensing applications [11]–[13]. Our particular line of research focused on creation of qubits using electron spins and manipulation of these states via electrostatic gates.

1.2 Motivation behind Carbon Nanotube Double Dot experiments

Interest in qubits, and related quantum information processing schemes, stems primarily from the limitations of a class of modern algorithms whose computational time grows exponentially with the problem size. The solutions to these problems can be verified quickly however, in a time that grows only as some polynomial of the size of the problem [14], [15]. Although this may seem to be a relatively esoteric problem to inspire such concerted effort, there are a great many practical applications of these algorithms that are encountered in everyday life. The most cited such example is public key encryption, which underlies almost all secure-web traffic. At its heart this algorithm relies on the problem of factoring a large number into two primes [16].

While it is relatively straightforward to verify that two numbers when multiplied together give a product, it is difficult to find the two factors given only the product. This asymmetry in the calculation is what makes easy, strong encryption possible.

For longer numbers, an ordinary computer would take exponentially longer to solve this kind of problem. However, by using a quantum computer, in which individual bits are manipulated as a superposition of states, it is possible to solve this kind of factoring problem in polynomial time [17]. A handful of other quantum algorithms creates the possibility of solving specific problems substantially faster than is possible using an ordinary or classical computer. Thus the ability to perform a complete set of operations with quantum bits has the potential to open an entirely new area of computation. It is this possibility that has spurred extensive research into the manipulation and measurement of individual quantum states and efforts to implement specific manifestations of qubits. This application is at a somewhat far remove from the day-to-day considerations of designing and performing qubit manipulations but is nevertheless the underlying motivation. As hinted previously, the specific manifestation of a qubit on which our carbon nanotube research focused, was the electronic spin degree of freedom for a single electron within a quantum dot. By utilizing the inherent symmetries of the electron wavefunction, it is possible to manipulate the electronic spin states purely through electrostatic control of the spatial wavefunctions shown in Figure 1.2 [12].

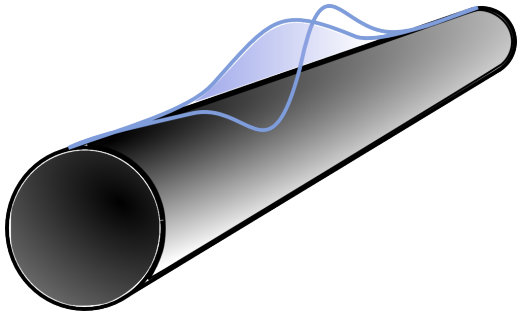

Figure 1.2 Lowest Order Spatial Wavefunctions in Carbon Nanotube
The first and second order longitudinal modes are shown in blue, a quantum dot defined electrostatically in the tube with tight longitudinal confinement has a lower energy first order wavefunction. With two electrons in the dot, the spin singlet then becomes the favorable over the spin triplet. Relaxation of the confinement can then allow each electron spin to evolve independently.

While the nanotube research was not ultimately able to achieve a suitable incarnation of a single occupancy double dot, it did yield significant progress in terms of fabrication techniques and materials science analyses of our devices. All of this capability was critical to the development of the subsequent project, graphene mid-IR detectors.

1.3 Motivation behind Graphene Mid-IR experiments

The mid-infrared is a part of the electromagnetic spectrum that has a large number of potential applications. Various groups have different definitions of what wavelength range corresponds to the mid-IR but here I will assume that it roughly corresponds to a window of 5-14μm in wavelength. First of all, this is an energy regime that corresponds to peak blackbody emission for objects at or near room temperature. Passive or thermal imaging of people and objects has many uses, for instance in night vision, or in failure detection of electrical or mechanical equipment.

Failure points for operating equipment often correspond to excess friction or resistance, which can be seen via thermal emission.

Additionally, many molecules have vibrational modes with energies in this regime. This is one of the reasons that Fourier Transform Infrared Spectroscopy (FTIR) is so useful in characterizing unknown molecules or substances. The rich spectroscopic fingerprint that can be gathered rapidly makes it feasible to build relatively compact equipment that can assay materials. Further miniaturization might make this capability handheld, opening the possibility that holding an instrument up to a material can determine its composition or allow the quick and easy detection of natural gas leaks.

Unfortunately the current detectors for these wavelengths have significant limitations. These detectors can be effectively divided into two classes. The first operate photovoltaically, wherein a photon is absorbed into the material and generates an electron-hole pair within the semiconductor material. For the process to be possible with mid-IR wavelengths it is necessary to have a relatively small bandgap material (on the order of ~100meV) so conventional semiconductors are not appropriate. Instead it is necessary to use a material such as mercury-cadmium telluride (MCT) where the bandgap of the CdTe material is reduced by inclusion of some percentage of mercury [18]. The problem with these materials is that they are highly toxic (as you can imagine) so that processing them and creating the imager is very expensive. In addition, the photovoltaic detection mode requires that the detector be cooled, usually to liquid nitrogen temperatures. This is because the thermal activation of carriers

across the small bandgap produces a large dark-current at room temperatures. The result is a sensitive but very expensive and bulky thermal imager. The other class of detectors operates thermally, i.e. it senses localized increases in the temperature of the imager surface due to irradiation with the mid-IR light focused onto it with a lens. Among this class of sensors there are a wide variety of detection mechanisms. Most prominent are microbolometers, frequently made from amorphous silicon or vanadium oxide. When heated, these materials significantly change their resistance, in the case of vanadium oxide due to a phase transition between metal and insulator [19]. Because they require a change in their temperature it is usually necessary to thermally isolate the active area of the pixel from the underlying substrate, typically by suspending the amorphous silicon or vanadium oxide layer using MEMS processing steps. The fact that they have to change their temperature also makes them relatively slow to respond to changing illumination, as well as making them inherently less sensitive than the photovoltaic detectors. However, they are less expensive and can be operated at room temperature, which is advantageous for many applications.

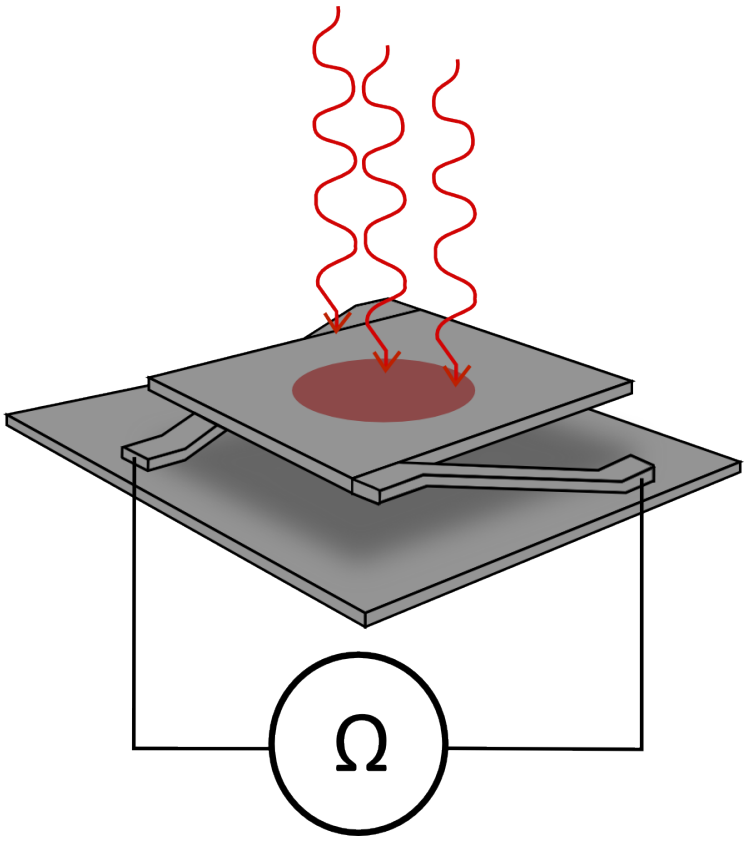

Figure 1.3 Schematic of Common Microbolometer Geometry
The bolometer material, suspended above the substrate, absorbs IR radiation and changes temperature. The change in temperature alters the electrical resistance of the element and can be detected with readout circuitry.

Based on previous experiments it is known that a graphene p-n junction generates a current under optical and near-IR illumination due to a photo-thermoelectric mechanism and that hot carriers, not in thermal equilibrium with the lattice, are important in this response [20]. Our motivation in using graphene for detection of mid-IR wavelengths was two-fold. First, that graphene, by absorbing photons at these energies might produce a larger signal than otherwise expected. This

possibility is due to the poor coupling of conduction electrons to the lattice causing slow transfer of their kinetic energy to phonons, so that hot electrons generated by absorption of photons can transfer their energy to other electrons (carrier multiplication) leading to a larger signal. Optical phonons that provide good coupling between the electrons and the lattice have a minimum energy of ~200meV, significantly above the 117meV energy of photons at 10.6μm [21], [22]. Because this cooling path is not available, hot electrons might diffuse further than in optical devices and potentially have a larger impact on the performance of the detector. Secondly, since graphene is nontoxic and relatively easy to grow, it would be substantially cheaper to produce detectors from graphene than from other substances. Although graphene growth for this experiment was done using individually grown samples, there are plans to make large scale, cheap production of graphene possible using reel-to-reel systems and compatible furnace configurations [23].

An additional cost advantage might be possible due to simplified fabrication steps of the sensing electronics and increased functionality of the detector. Because the signal is produced almost exclusively in the p-n junction, it is possible to turn the junction on and off with application of appropriate gate voltages and modulate the detector signal electrostatically. Since this is a unique property of graphene there are potential applications that would not be possible with other materials and/or sensor types.

Our goal was to determine if graphene would produce a response under mid-IR illumination, and to determine the mechanism of that response. Since a majority of our

motivation stemmed from a desire to make a "better" thermal imaging system, most of our overall goals focused primarily on engineering the response and readout of our detector. We wanted to consider not just sensitivity, but the integration time necessary to produce an image and the electronics necessary for the readout. The physical size and power consumption of a potential imager chip were also considered as we developed this technology.

Chapter 2

2. Carbon Nanotubes for Single Spin Electronics

2.1 Introduction

The effective 1-D confinement of electrons in a carbon nanotube presents unique possibilities for single-spin manipulation and charge sensing using purely electrostatic control via local metallic gates [24]. Additional considerations such as mechanical rigidity and a band structure controlled by chirality and strain provide a wide variety of potential devices and applications [2]. The primary problem in this field has been the controlled and reliable growth of single-walled carbon nanotubes (SWNT) with a specific diameter and chirality. It is possible to exercise rough control over the diameter and number of walls via the growth technique but fine-tuning the electronic characteristics remains challenging.

The band structure of a carbon nanotube can be derived via a tight binding approximation. This band structure's chirality dependence can be divided roughly into two classes, semiconducting and metallic. This property is determined by the

quantization conditions that are imposed when the graphene sheet is rolled and joined to itself, creating the nanotube. In k-space, this corresponds to effectively creating a series of discrete, allowed k-vectors perpendicular to the axis of the nanotube, i.e. in the same direction as the chiral vector that defines the circumference of the nanotube.

The allowed k vectors define lines that bisect the normally allowed k-states of the graphene sheet; if those lines intersect the Dirac points then the nanotube is conducting (i.e. metallic), if not the nanotube will be semiconducting. There is an additional class of nanotubes that are metallic intrinsically, but have a curvature or strain induced gap that causes a small gap in the band structure. These small gap tubes are desirable for our electron-spin experiments, since it is possible to form a potential well where a single electron is confined and controlled by an electrostatic gate. The primary goal of this project is to create a qubit based on the ½ spin of a single electron. In creating any qubit, one of the primary concerns is decoherence introduced by unwanted interactions of the quantum system with the environment. For a qubit based on an electron spin, one of the primary sources of decoherence is the magnetic dipole-dipole interaction of the electron with the nuclear spins that exist in the material. This effect can be studied and potentially controlled if the electronic material has a spinful isotope whose concentration can be varied. For this reason carbon nanotubes are an ideal candidate system, since the primary constituent isotope of carbon is spinless (^{12}C) and the spinful isotope (^{13}C) can be separated using gaseous enrichment techniques. The nanotubes can thus be grown out of the ^{12}C or ^{13}C methane and the nuclear effects on the decoherence can be studied in a controlled setting.

2.2 Carbon Nanotube Growth

Due to the uncontrolled nature of nanotube growth it is often necessary to grow a large number of potential devices before a candidate can be found that has the desired properties. Additionally, the subsequent processing steps can damage tubes by either destroying them entirely or doping them in such a way that the electron density cannot be controlled all the way down to a single electron. In our design a large number of tubes are grown on Fe catalyst pads, deposited via electron-beam lithography and subsequent evaporation of approximately 5nm of Fe. After performing liftoff the chips are placed into a tube furnace under an Ar atmosphere. The tube is heated to ~950°C and a mixture of methane and hydrogen gas is flowed for 15 minutes. The time and concentration of the gases can be adjusted to increase or decrease the number of nanotubes that are grown, but again the control is only statistical in nature. The diameter of the tubes is approximately controlled by the thickness of the Fe pads, with thicker pads leading to larger Fe droplets. These droplets catalyze the breakdown of the methane into soluble carbon which then precipitates from the Fe droplet and forms the nanotube [25]. As the nanotube grows either underneath the Fe droplet lifting the droplet up, or grows up off of the droplet (which remains on the surface), the nanotube extends upward into the gas flow. Eventually the nanotube reaches a length where it is no longer able to support itself, and it falls back to the substrate chip where it can continue to grow along the surface. During later growth processes we also utilized a catalyst composed of a solution of $Fe(NO_3)_3 9H_2O$ and $MoO_2(acac)_2$ with alumina power suspended in the solution [3]. This catalyst worked in a similar manner

as described above, but over the course of our experience seemed to give more uniform and reliable results.

Typically we image the growth of nanotubes using a scanning electron microscope (SEM) to locate nanotubes that have the potential to form good devices. These are relatively short (less than 10μm) and straight along the length of the device to make further lithography steps easier. The SEM imaging itself is best done at a very low acceleration voltage of around 0.7-1.5kV. This allows the electrostatic effects of the conducting nanotube to show up against the insulating substrate (Figure 2.1).

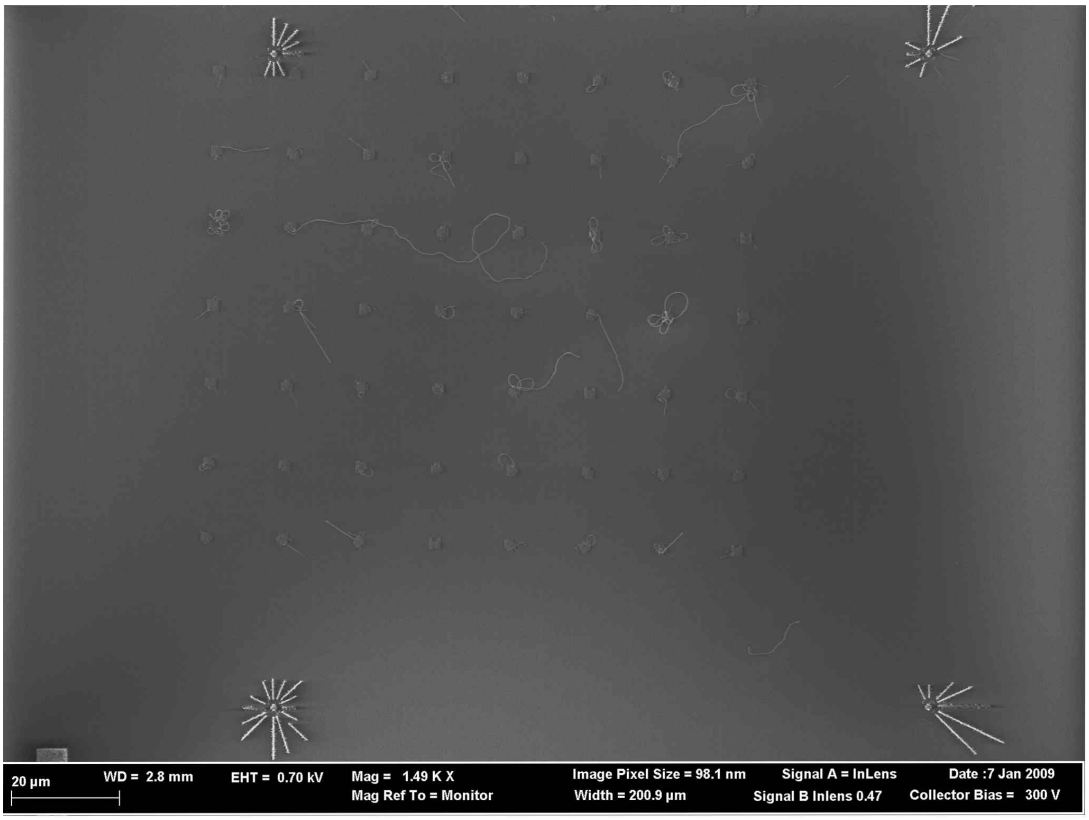

Figure 2.1 Good Growth of Carbon Nanotubes
SEM image showing typical growth of nanotubes off of the Fe-based catalyst. Good candidate devices are visible.

Occasionally no nanotubes will grow at all, which was most common when growth was attempted with the ^{13}C methane. Although no direct evidence was found, this was presumably due to a small amount of oxygen present in the system, poisoning the catalytic process in the Fe droplet that allows growth (see Figure 2.2). The configuration of the system meant that although the line was purged with Ar, there was a dead space between the ^{13}C methane bottle and the manifold that led to the growth chamber. Additionally, the number of connections between the bottle and the growth chamber greatly increased the probability of a leak. Even if the gas lines and manifold are maintained at a positive pressure during the growth process, leaks are anecdotally known to poison the growth process in graphene CVD chambers utilizing a similar gas chemistry and growth apparatus. Leak checking was also not possible since it would be difficult and potentially dangerous to put the gas lines under vacuum. Precautions during assembly of the systems were the best measure against potential leaks. Another complication was the fact that the catalyst would occasionally have problems or become inactive after long periods of time.

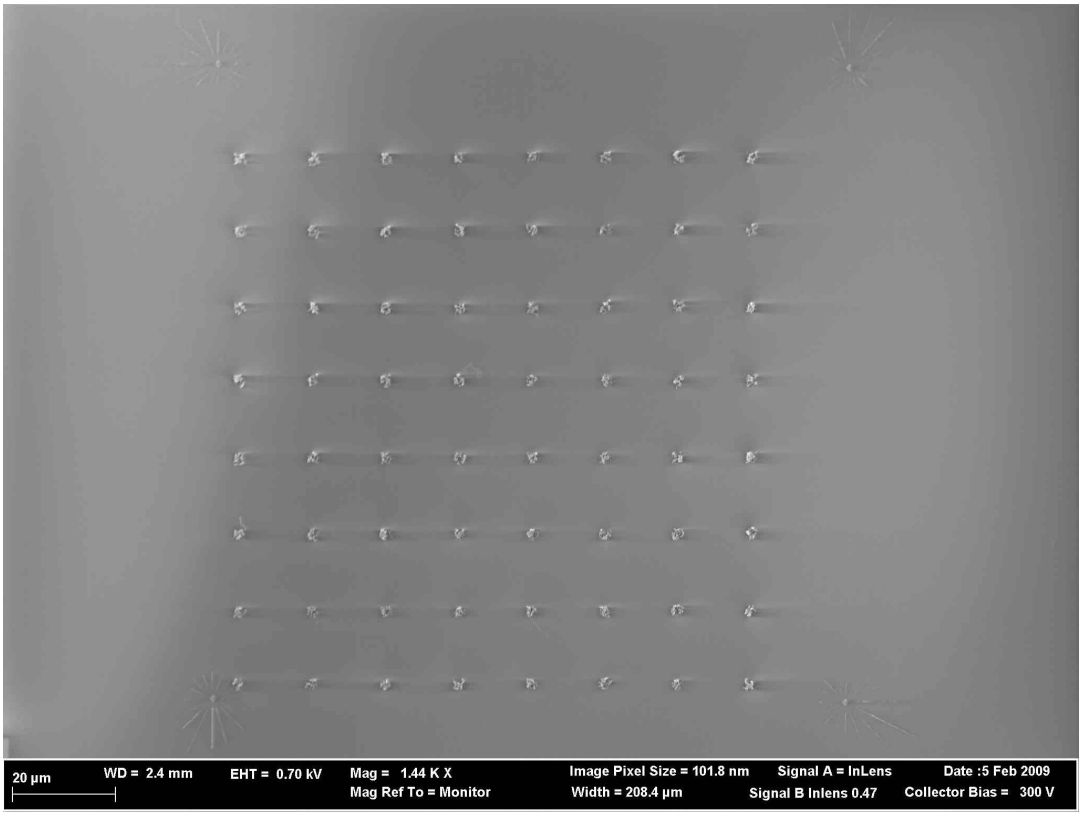

Figure 2.2 Poor or Poisoned Growth
SEM image of after growth process showing little or no growth of nanotubes off of the catalyst islands on the surface of the chip.

2.3 Gate Dielectrics

In creating a carbon nanotube device one of the primary considerations is creation of a gate structure that can both define a quantum dot and deplete it down to a single electron or hole. The voltage that can safely be applied is dependent on the type and permittivity of the gate dielectric that is deposited. Another consideration is the fact that the cylindrical nature of the nanotube makes coverage of the sides and bottom of the tube problematic unless a large amount of dielectic is deposited. Such a large amount of dielectric reduces the capacitive coupling of the metallic gate and the

nanotube, requiring higher voltages to be applied to the device. To avoid these issues, we deposited an aluminum oxide (Al_2O_3) dielectric layer via an atomic layer deposition (ALD) technique. This technology utilizes the few molecule thick layer of water (H_2O) that normally resides on the surface of a chip due to chemisorption on the substrate [26]. This thin layer of water exists even under vacuum, although it can partially be desorbed from the surface over a longer time scale.

At its most basic, ALD deposition occurs in a cyclical process, first absorbing a layer of water, evacuating the chamber, and then releasing an organometallic such as trimethylaluminum (TMA), which reacts with the water. This yields a solid byproduct, Al_2O_3 on the surface of the chip, and various gases that are then evacuated from the chamber. Finally, water vapor is released into the chamber and a new layer of water forms on the surface of the chip. Because the process evenly coats the entire exposed surface it has excellent conformal covering of the surface as long as nucleation of the coating can occur.

Nucleation is determined by the adsorption of water on the surface, a temperature-dependent process that tends to be suppressed on the surface of the nanotube due to its inert chemical nature [27]. A similar problem occurs on the surface of pristine graphene sheets, where only the edges and defect sites can bind the precursor molecules and initiate growth. There are several ways in which this obstacle can be overcome, most notably through functionalization of the carbon surface with a chemical that has a higher affinity, allowing it to adsorb onto the carbon surface in either a gas or liquid phase [27], [28].

2.4 NO_2 Functionalization

The initial experiments involved chemical bonding that altered the electronic and material properties of the carbon nanotube or graphene layer. As a result these subsequent processing steps were degrading the very properties that make these materials so interesting and useful. The natural progression was to use a functionalization layer that did not bond strongly enough to chemically affect the carbon surface. For the growth of aluminum oxide (Al_2O_3) ALD nitrogen dioxide (NO_2) as an oxidizing agent for the trimethylaluminum allows a stable oxide to form on the surface of the nanotube without destruction of its electronic properties [27].

In our experiments we utilized a Cambridge Nanotech ALD system outfitted with a NO_2 bottle and a gas manifold that allowed the introduction of trimethylaluminum. After 5 to 50 cycles of NO_2 the coating was continued with H_2O as a precursor chemical instead of the NO_2. The other important parameter of the process is the temperature of the sample and the chamber during the deposition. A higher temperature leads to a denser and more uniform oxide coating but a lower deposition thickness per cycle. To have effective gating characteristics it is necessary for the thickness and dielectric constant of the insulator to be highly uniform over the area of the gate [29]. As a result, once the nucleation of the ALD layer with NO_2 was finished, the temperature of the reaction chamber was raised for the remainder of the deposition, allowing a denser and more uniform Al_2O_3 layer.

The other aspect of the NO_2 functionalization is its effect on the electronic characteristics of the carbon nanotube. The adsorption of NO_2 onto the surface of

single walled carbon nanotubes causes significant changes in the conductance of the nanotube [30]. It is therefore unsurprising that the nanotube changes its electronic properties as the ALD deposition involves partial adsorption of NO_2 onto the surface. The chemical moiety is altered through the competing electron-donation of the TMA and the electron acceptation of the NO_2, an effect that can be used to minimize the doping effect of ALD deposition [31]. However, in our experiments the variability of the nanotube characteristics demonstrated a somewhat unpredictable process as shown in Figure 2.3. For all of the traces nanotube growth and ALD recipes were effectively identical. However, the same starting point leads to such different results that it is virtually impossible to provide reproducible and reliable devices. The solution was to try a large number of potential devices and screen them for the desired characteristics.

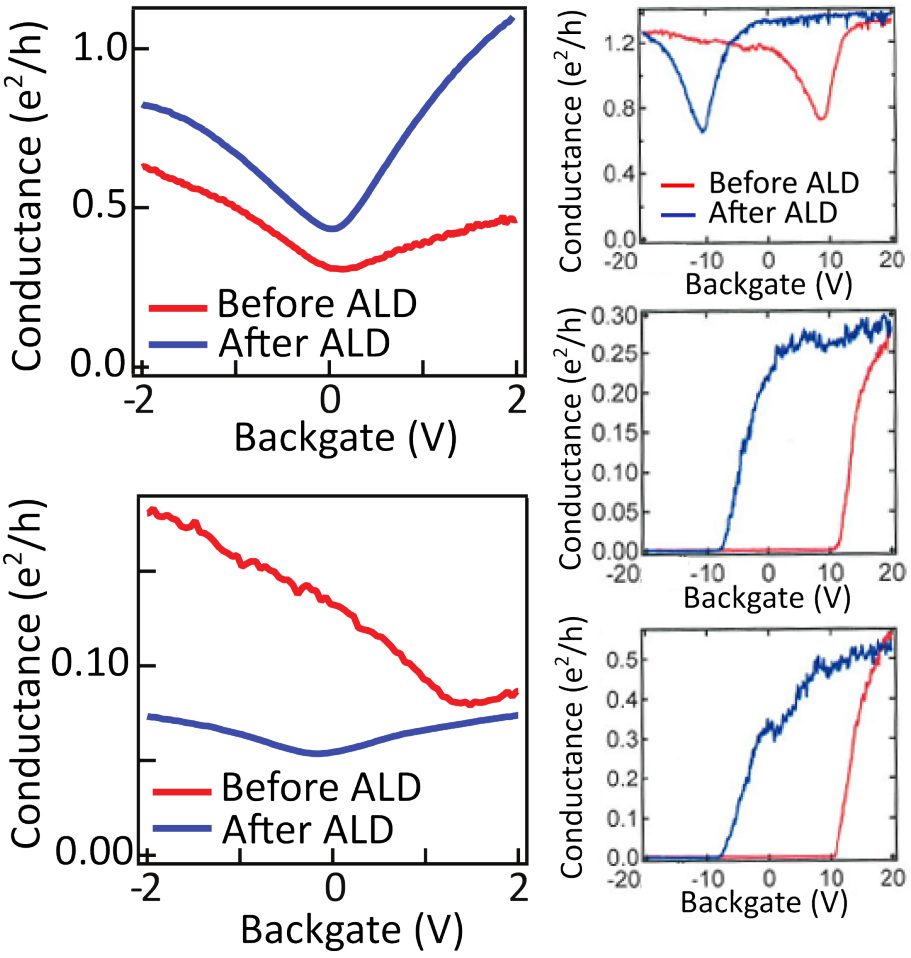

Figure 2.3 Comparison of Carbon Nanotube traces Before and After ALD
There is a large amount of variability in response to ALD deposition. Conductivity can increase or decrease and doping can shift the conductance minimum positive or negative. Even with identical growth and ALD recipes the results are largely random.

The NO_2 functionalization eventually proved to be unnecessary and undesirable as we moved to more complicated process recipes. Some of these recipes involved etching the ALD dielectric and we found that the functionalization layer was not etched by any of the aqueous processes that we had available. Instead, we used an ALD process where initially isopropyl alcohol (IPA) is used at a lower temperature to

begin the growth of the oxide before switching back to H_2O and higher temperatures [32]. This method for ALD growth also proved useful in my later work on graphene devices since growth of uniform ALD on graphene seemed to be enhanced with IPA as a precursor chemical for the first 10-50 deposition pulse cycles.

2.5 Disorder and Undesirable dots

The ability to create a well-behaved double quantum dot is a matter not only of creating an appropriate structure, but also of controlling where quantum dots form in the nanotube. This can be much harder than one might expect based on a naïve understanding of the electronic environment of the nanotube. Defects in the nanotube, variations of the dielectric, charge traps in the oxide and Schottky barriers at the contact interface can all effect the position and placement of the quantum dots that form as the nanotube is depleted under the electrostatic influence of the various gates. In particular, a reoccurring problem in our experiments was the appearance of unwanted quantum dots that disrupted the honeycomb conductance structure (Figure 2.4) that characterizes a well-behaved double quantum dot [33].

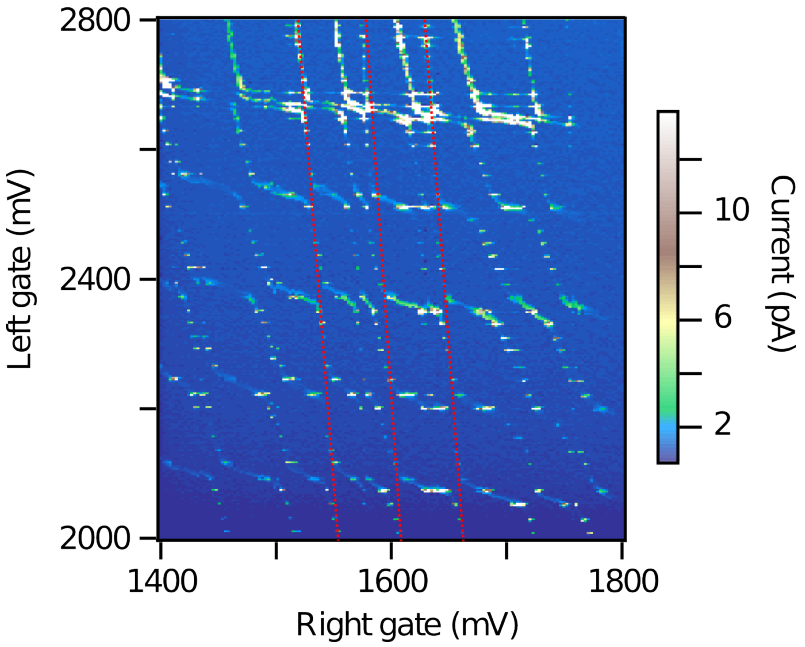

Figure 2.4 Third Dot near Right Gate
An additionally transition line is visible in the gate voltage map of the transport current. Since it disrupts the transitions of the dot coupled more strongly to the right gate we infer that it is near the right contact.

Under many circumstances we inferred this quantum dot formed under the contact junction between the metal and the carbon nanotube. There are multiple possible causes for an extra quantum dot to form at this location. The most obvious is the mismatch in work-function at this junction leading to a Schottky barrier. The quantum dot formed within this well is highly localized and difficult to control with any of the electrostatic gates of the device. As a result most of the time it was impossible to find a gate potential configuration that allowed us to completely eliminate this dot. At times we pursued various strategies to mitigate the effect of these extraneous dots by either isolating them from the double dot in the middle of the device or by making them as small as possible. These extra dots were not desirable for

use in our experiments, since the small amount of gate control made them difficult to control and their large coupling to the leads would introduce a significant amount of decoherence in any spin manipulation experiments [34], [35].

2.6 Suspended Devices

Other sources of disorder could also introduce unwanted dots, and charge traps in the SiO_2 oxide layer were a well-known source of unwanted variation in the potential landscape. The cleanest, most controllable devices were those grown as suspended nanotubes where no further processing occurred after the growth of the nanotube [36]. These devices were known among our group as "growth-last" devices and inspired us to attempt a related fabrication approach. One of the major limitations of the growth-last devices is that they generally cannot have a complex gate structure owing to limitations of the geometry. The gates have to either be buried underneath a dielectric layer, or separated by suspension of the nanotube over the gates. The fact that the growth process involves high temperatures (~900-1000°C) poses an additional complication since materials often undergo phase transitions or other phenomena at these temperatures. Of particular concern to us was the fact that dielectric materials often begin leaking electrically or change from an amorphous to a crystalline state when subjected to these temperatures. Additionally, many metals will partially melt or creep at these temperatures, even if their bulk melting point is substantially higher. For instance, Pt has a melting point of 1768°C but our 100nm features will turn into amorphous blobs if heated above 900°C (Figure 2.5). It is possible to prevent this from

happening by including a thin layer of W in the middle of the Pt but care must be taken to prevent too much of the W surface from being exposed since it can poison the growth.

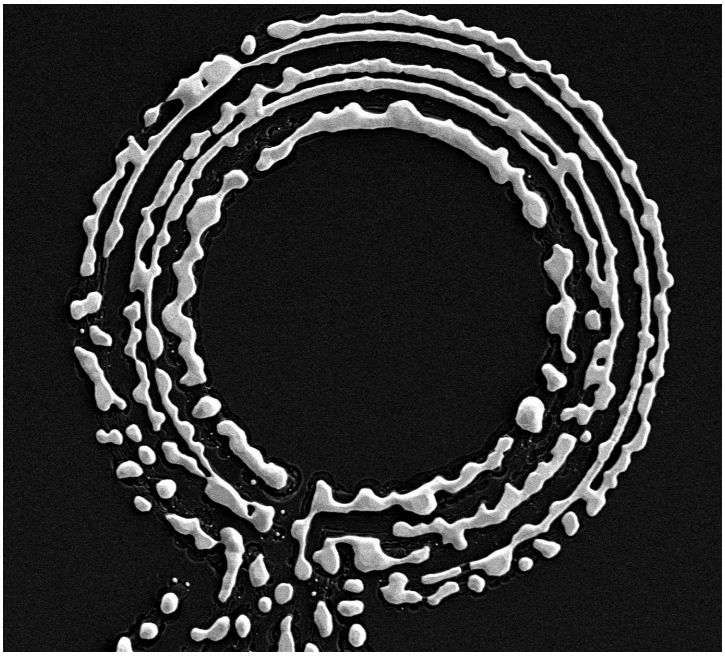

Figure 2.5 Melted Platinum Ring Structure
Without an internal tungsten reinforcement layer the Pt will melt during carbon nanotube growth.

The complications of trying to include a growth-last fabrication with complicated and precise gate structure motivated us to try several intermediate approaches. This first was to contact the nanotube on the SiO_2 substrate, then define a window using e-beam lithography right around the device and etch away the supporting SiO_2. This necessitated the use of a critical point dryer to ensure that the structure did not collapse due to capillary forces. The suspended nanotube device was then covered by Al_2O_3 ALD, which is believed to be cleaner (that is more free of

charge traps and disorder) than the SiO_2 substrate. After this step, fabrication could proceed normally. However, this procedure did not remove the unwanted disorder from the device. Additionally, the critical point drying procedure is time consuming and requires constant monitoring to succeed [37]. We thus abandoned this approach and moved onward.

Our next attempt to remove disorder was to grow the nanotubes in a suspended state. This required that we provide some sort of support structure off the surface of the substrate. Ideally, the structure would also provide electrical contact to the nanotube and be high enough to prevent the nanotube from falling down and touching the substrate (a height of ~10% of the unsupported length is recommended). To satisfy this requirement we used a structure where the contact metal (a Cr/W/Pt stack) is patterned first on the SiO_2 substrate, supported by ~50nm of evaporated SiO_2 to ensure that the surface of the metal is elevated far enough above the surface of the chip. After patterning these structures all over the surface of the chip, the catalyst is deposited in the center of the structure and growth is preformed as normal. Since the nanotubes tend to grow up and then fall across the surface there are a significant number that end up supported by the metallic contacts. By immediately doing ALD growth of Al_2O_3, we tried to protect the nanotube from further contamination and ensure that the nanotube was not subjected to the disorder potential of the SiO_2 substrate. By making the Al_2O_3 thick enough it's possible to "fill" the gap between the tube and the substrate so that continuous gates (from the nanotube to distant bond pads) can be deposited in later steps. Since the contacts to the nanotube are now coated in an

insulating material it is necessary to etch a via through the Al_2O_3 to the metal, while avoiding the nanotube. Earlier experience had shown that aqueous etch chemistries were enhanced and tended to spread along the surface of the nanotube, completely removing the dielectric around the nanotube.

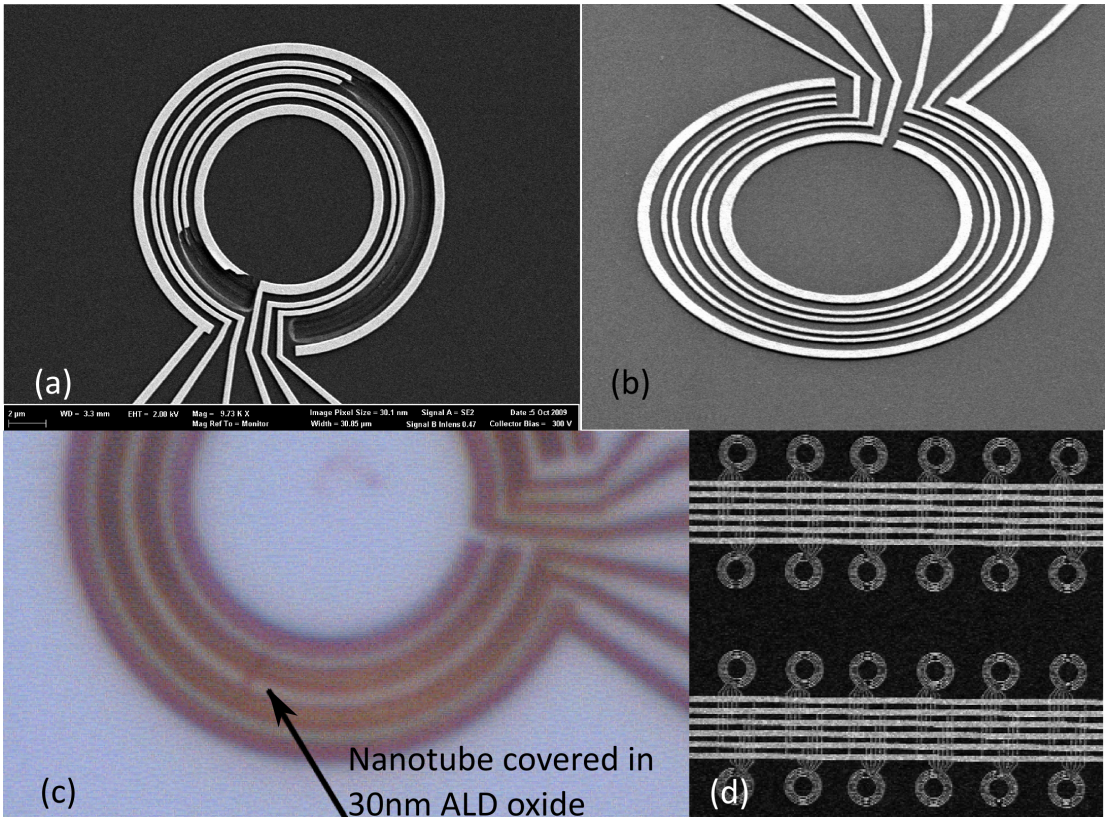

Figure 2.6 First Iteration of Rings for Suspended Nanotubes
SEM and optical images of Ring structures (a) Ring after breaking to remove unnecessary portions (b) Full Ring structure before growth (c) Optical image showing and ALD covered suspended nanotube (d) Array of Ring structures before growth

The etch step itself often encountered significant problems, mostly in terms of the recipes that we needed to use. An early problem was the cracking of the ZEP resist layer after exposure to the aqueous etch, causing etching in undesirable areas. We also

saw delamination of the ZEP layer during the etching, prompting us to use a sticking layer of Cr (which had to be removed before the oxide etch). Both of these phenomena point to significant stress in the ZEP resist upon exposure to the KOH etch. Process variation was another problem with this step, presumably due to temperature variation or etchant concentration variation. We guessed this parameter variation, since the same etch time would sometimes under-etch and not fully expose the contact pads, and other times over-etch and remove the oxide from around parts of the nanotube. In general, we finally concluded that aqueous etching should be avoided if possible. Dry etching processes, although potentially more damaging to surfaces, are significantly more reliable and controllable, especially in a shared-facility setting.

Once the contacts of the device were exposed, the gates and contact lines were patterned with e-beam lithography and deposited using a rotating-tilt stage. This was necessary to get a more conformal coating of the metal over the uneven surface, especially in the area right around and on top of the nanotube. The resulting structures could then be characterized electronically. The downside of this process is that electronic characteristics can only be determined at the end, after a lengthy fabrication process. In the end, the process yield was not high enough to produce an effective device for our experiments.

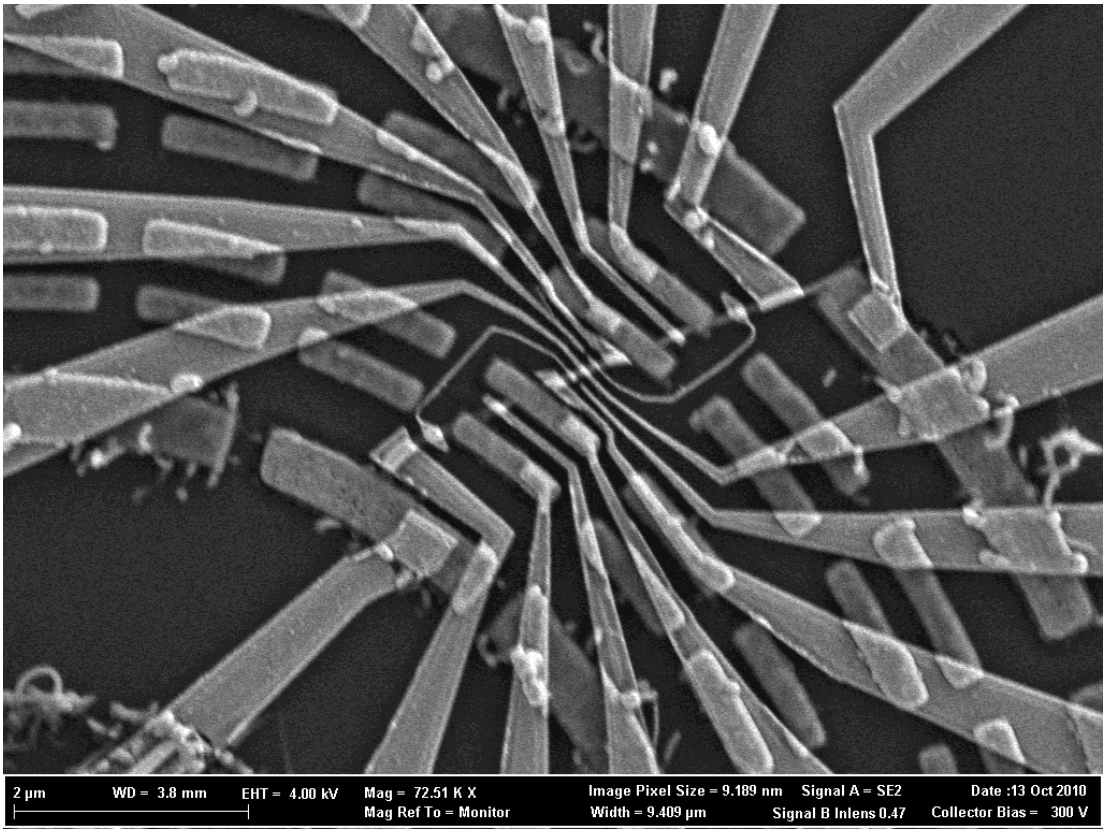

Figure 2.7 Dashed Ring Device Completed
A second iteration of the ring structure with only dashed contacts so that breaking the rings was no longer necessary. Holes etched through the ALD are visible with contact lines running to the contact pads. The ALD covered nanotube and gates for defining and controlling the double dot and integrated charge sensors are also visible.

2.7 Effect of ALD on Carbon Nanotube Transport Characteristics

As a complement to this work on suspended devices, and because one of our major assumptions was that the ALD Al_2O_3 did not contribute to disorder, I undertook a series of measurements to study the effect of ALD growth on the electrical transport characteristics of carbon nanotubes. Although there has been a significant amount of prior work on the effect of ALD deposition on the surface of carbon nanotubes [27], [38], these studies do not typically make detailed measurements at low temperatures

where the individual electronic energy levels are visible. They also do not always measure the kind of nanotubes that we were interested in, and differences in processing recipes can make a significant difference to the results that are achieved. All of these considerations motivated us to make our own measurements.

The measurements were conducted on carbon nanotubes grown via our early, standard technique described above and contacted with Pd. Since we used a Si/SiO_2 substrate, the doped Si acted as a global backgate for all of our devices. We measured a number of devices in a dilution refrigerator at ~112mK (a measurement extracted from the edge of a coulomb blockade diamond) and for specific transitions of interest, checked their behavior as a function of the applied magnetic field. For several of the devices clearly distinguishable 4-fold transitions were observed as each of the longitudinal modes is sequentially filled (Figure 2.8).

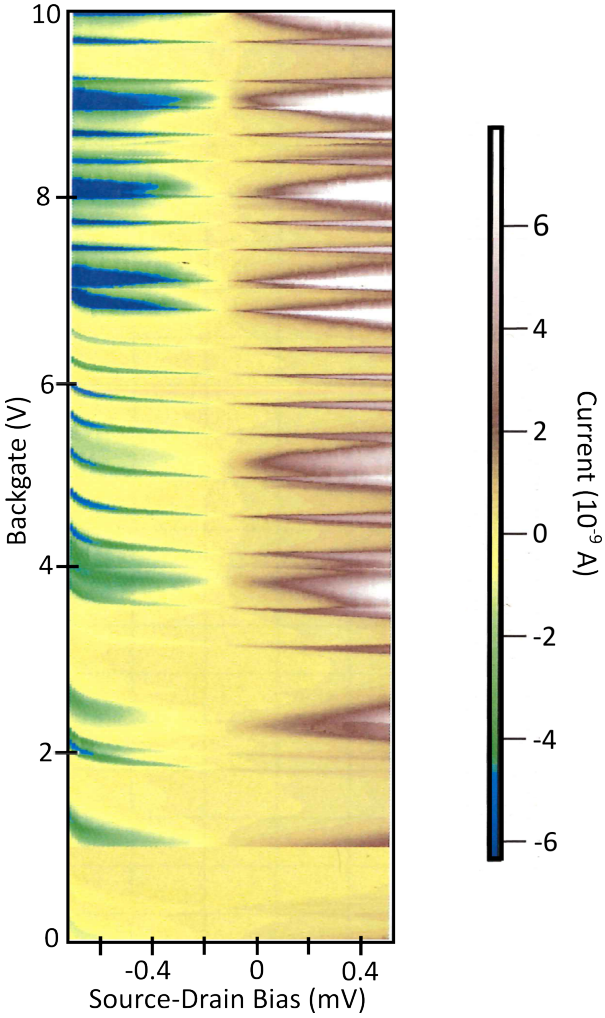

Figure 2.8 4-Fold filling of Carbon Nanotube Dot

Close 4-fold transitions in a carbon nanotube dot are visible. Second set of broader features are due to a second carbon nanotube dot that was also connected in parallel between the two contacts.

Unfortunately the variability in the behavior of the individual carbon nanotube devices complicates our ability to draw direct conclusions about the effect of ALD gate dielectric. In general ALD deposition degrades the transparency of the contacts on the p side as evidenced by the lower conductance at negative gate voltages after the ALD (Figure 2.9 and Figure 2.10). ALD deposition can also dope the nanotube since

several of the features clearly shift after the deposition. Finally, the closer spacing of several of the transitions indicates that charge screening by the dielectric is reducing the charging energy of the dot. But the variability of the nanotube behavior combines with the variability in the ALD effect, resulting in a large amount of data, a portion of which is shown here, but with scant general conclusions.

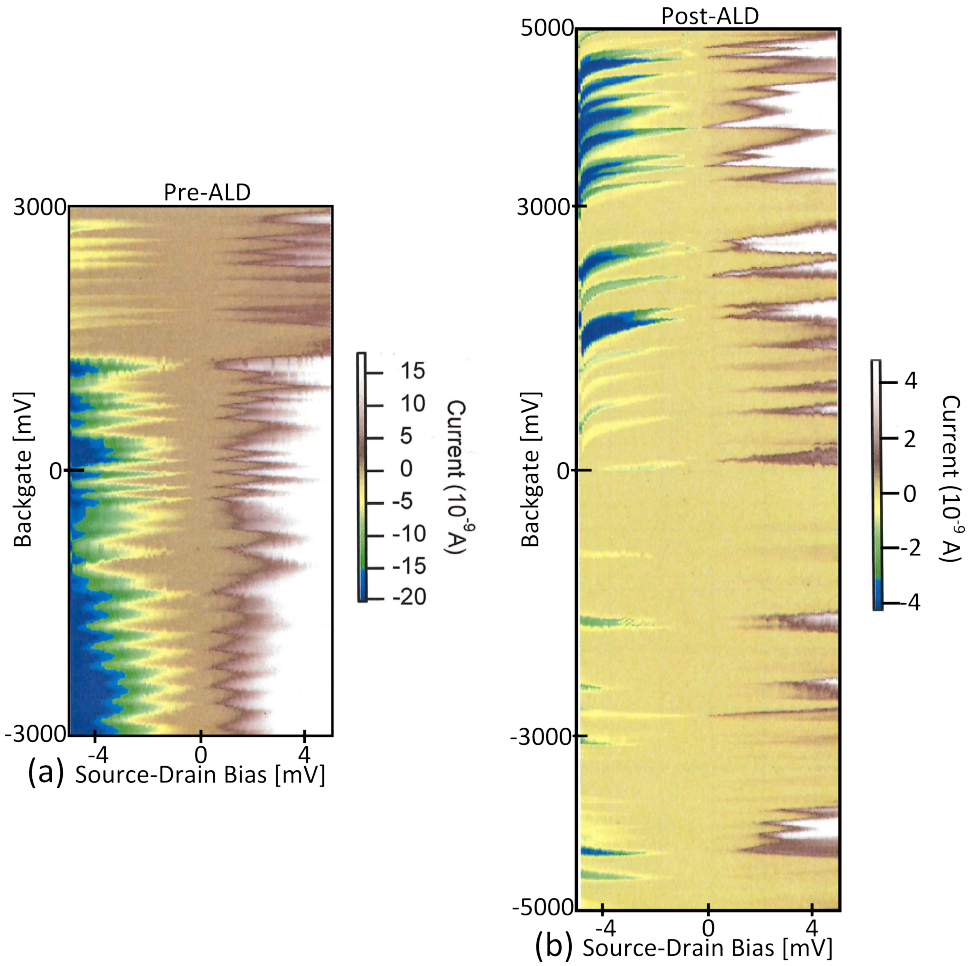

Figure 2.9 Device 15-19 Pre and Post ALD deposition.
(a) Initially the device has a larger conductance at negative gate voltages (b) The device shows a significant degradation in conductance at negative gate voltages Post ALD. In addition, the gap (transition between carrier types) seems to have shifted to lower gate voltages.

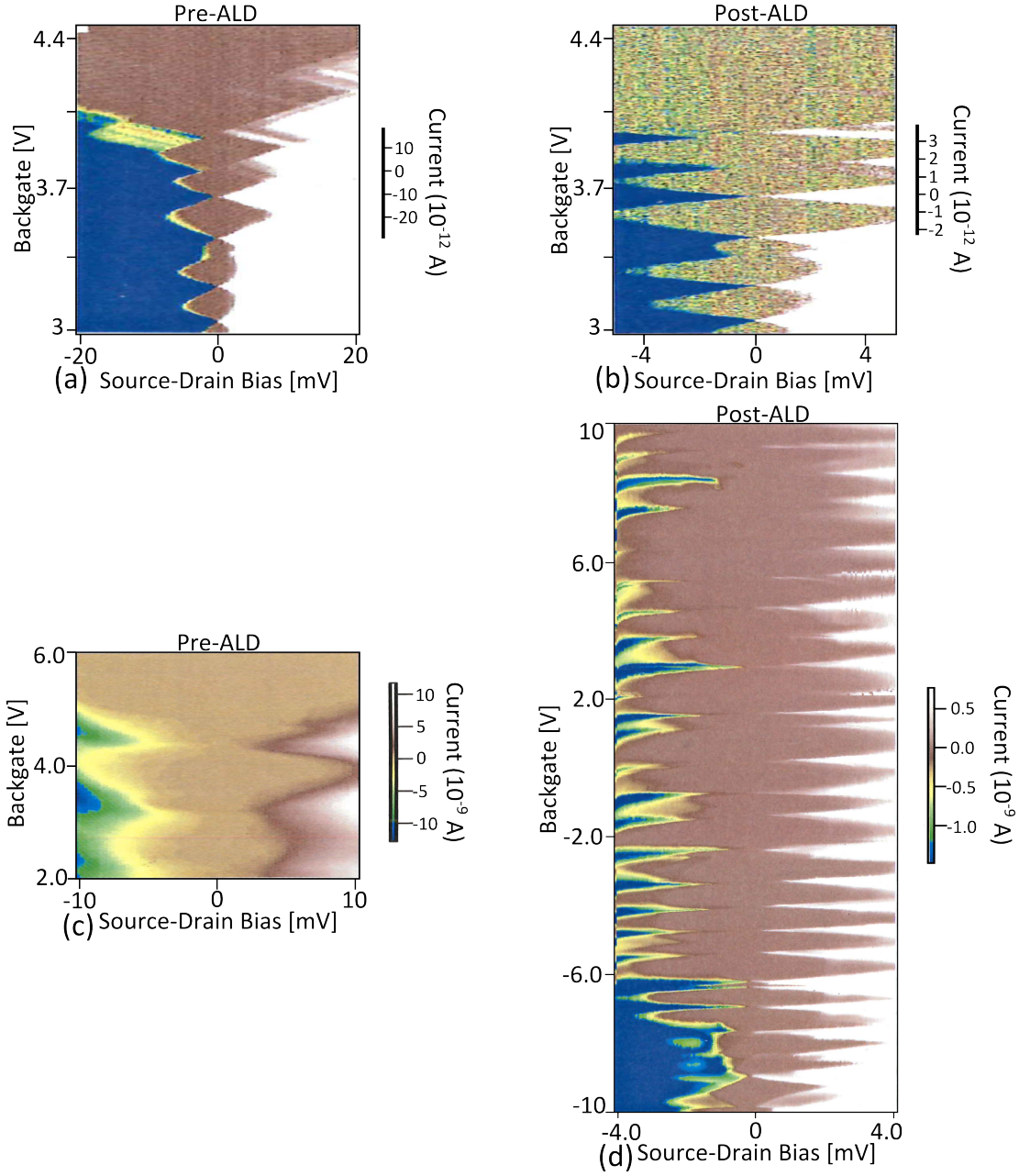

Figure 2.10 Devices 15-19 and 6-9 Pre and Post ALD

(a)&(b) Device 15-19 conductance drops significantly after ALD deposition (c)&(d) Device 6-9, gap position and level spacing change after ALD deposition. Conductance also drops in this device.

2.8 Conclusions

The end result of our experiments yielded a great deal of data on the properties and operation of carbon nanotube double quantum dots. It also provided a large "toolbox" of recipes, processes and failure modes that could be applied to different projects. One of the major lessons that I learned is that research projects are almost always constrained by what is technologically possible. If you can create useful structures that no one else can, it will almost always have an application to some more advanced experiment. And the research that is done is often dictated by the available techniques and technologies.

Chapter 3

3. Bottom-Gated Si-Ge Shell-Core Nanowires

3.1 Introduction

After developing advanced fabrication techniques for carbon nanotube devices, it was natural to turn to another electronic material with many of the same characteristics. Experiments on Si-Ge nanowires had been conducted in a manner similar to the carbon nanotube research and many of the fabrication recipes were shared. For instance, these experiments utilized an ALD high-k dielectric and e-beam lithography defined top gates. However, since the nanowires were grown separately and then deposited on the substrate, it was more natural to adopt a bottom-gating approach where the only fabrication processing that occurred on the nanowire was the deposition of the contact metal. Additionally, since growth was done separately, there were far fewer materials constraints vis-à-vis high temperature processing.

3.2 Overview of the structure and properties of Si-Ge Nanowires

Si-Ge nanowires consist of a Ge core grown with an MOCVD technique [39], where the catalytic metal particle usually defines the diameter of the Ge wire to be 10-15nm. These nanowires grow vertically off of the substrate so once the Ge growth is finished (producing wires on the order of 10μm long) it is possible to coat them uniformly with intrinsic Si by flowing a silane precursor gas in the same tube furnace. This coating was typically 2-5nm thick and its purpose was to induce a band-bending effect similar to that seen in GaAs epitaxially grown heterostructures. This effect creates a hole-gas in the Ge wire at the Si-Ge interface while avoiding the inclusion of actual dopant atoms in Ge. Because no dopants are present, the disorder in the nanowire is substantially reduced and transport can occur ballistically, with no scattering between the contacts [40]. The growth technique also provides unique opportunities to engineer the band structure and properties along the length of the wire by changing the precursor chemicals, resulting in advanced heterostructures where effective mass can be modulated or where electron-hole recombination can enable optical coupling out of the electronic system [41]. And finally, because the actual volume of the electronic material is so low, it is possible to synthesize structures that are effectively defect-free and atomically perfect.

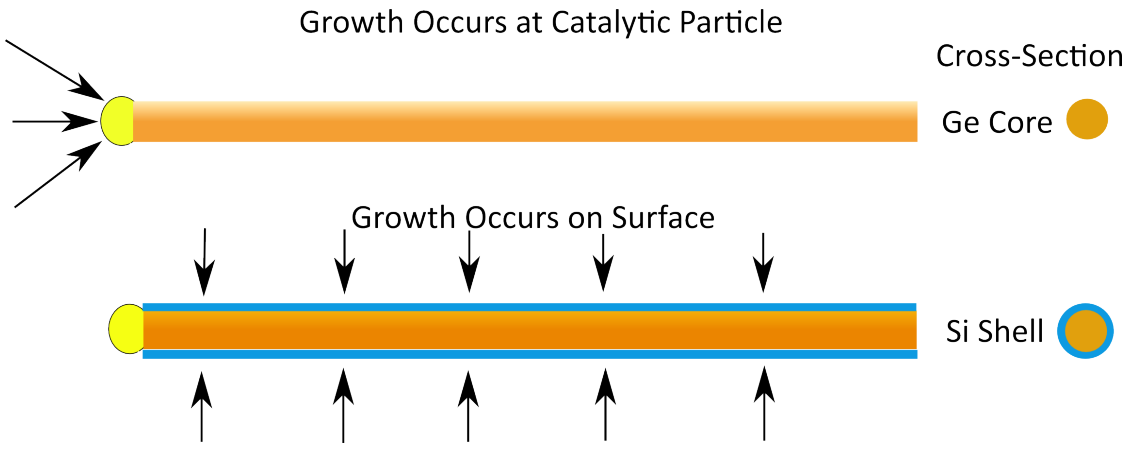

Figure 3.1 Schematic of Si-Ge Shell-Core Growth
The first stage of the growth occurs as the precursor is absorbed into the catalytic particle and forms the Ge core behind it. Second stage is growth of the Si shell on the surface of the core, creating the Si-Ge shell-core structure.

The hole band in Ge was of particular interest since it consists of a heavy hole (HH) band, light hole (LH) band and split off band. Each of these has different effective g-factors and effective masses that can be utilized to create a spin qubit. For instance, confinement can selectively allow tuning of the effective g-factor for holes, presumably by breaking the degeneracy between heavy and light holes that exists at the gamma point [42]. In our case, experience with decoherence in GaAs double dots had shown that hyperfine interaction with the nuclear spin bath was a significant problem [12], [34], [43]. Ge promised to offer a significant improvement since there is a smaller natural abundance of isotopes that have a nuclear spin. Only 7% of Ge is ^{73}Ge with a nuclear spin of +9/2. The same is true of Si, where only 5% is ^{29}Si with a nuclear spin of +1/2 [44], [45]. Additionally, these nuclear spins should have a smaller

coupling to the hole-states since the contact hyperfine term should be absent in these particular bands.

Previous experiments had explored the few-hole regime, with occupancies estimated to be a few hundred or less. Electrostatic gates allowed the creation of a double dot with an integrated charge sensor. Transport measurements corroborated the charge sensing data and a tunable coupling in the double dot was demonstrated [46]. Our goal was to move beyond this experiment and generate a spin qubit with single electron occupancy. Additionally, since spin-orbit coupling is large for these hole bands, we hoped to perform EDSR manipulations of the hole spin. This can be simply understood as an effective magnetic field on the hole when it is moving along the length of the nanowire. By shaking the electron spin spatially with an applied gate voltage it is possible to generate the same effect as an oscillating magnetic field, and rotate the spin through prescribed angles on a Bloch sphere. The advantage of manipulating the spin with an electric field is that the effect can be highly localized to one spin in a double dot while leaving the other untouched. Also, electrostatic control is generally simpler than generation of an oscillating magnetic field.

3.3 Bottom-Gate Fabrication Approach

For this project, many device qualities mentioned previously in the carbon nanotube research were desirable and necessary for the successful creation of a spin qubit. First, the desire for low disorder and defects prompted me to opt for a bottom gating approach where the gates are patterned first and covered with a dielectric. Since

the nanowire is deposited on top of the structure and then contacted with an appropriate metal, it is exposed to only one lithography step, which should reduce contamination and disorder [47]. Second, since a high degree of confinement is desirable, it is necessary to create a very small and closely packed gate structure with the smallest pitch possible. These are challenging but not incompatible goals for the design and fabrication tools that we had available.

There are several problems with a bottom gating approach. The first is that the deposition of nanowires is essentially random. Subsequent to the growth of the nanowires on a separate chip, that chip is placed in methanol and sonicated. This breaks off the nanowires, which are then left suspended in the methanol. A drop of the nanowire/methanol suspension is then placed on the chip with pre-patterned gates and allowed to dry. This deposits nanowires randomly over the surface of the chip. The only real control that is possible is the density of the nanowires in the solution. Obviously, since you are relying on a nanowire happening to fall in the right place, it is necessary to create a large number of gate structures all over the surface of the chip. Since writing bond pads occupies a large amount of area and is time consuming, this part of the process was left to the end, after the potential devices had been identified; where a nanowire had landed in a good orientation on the gates. Instead, only the fine gates are patterned in the first step.

An incidental effect of bottom gating is that it is not generally possible to create an integrated charge sensor on the same nanowire. This can make measurement of the charge state of the device significantly more difficult since transport through the

device is very small at low occupancies. A solution to this problem that we planned to employ was the use of a resonant circuit connected to one of the leads. The resonant circuit can be measured using RF reflectometry and the change in the quantum capacitance of the dot can be measured as a phase shift in the signal [48]. Appropriate tank circuits on PCB boards were constructed and measured to verify this operation.

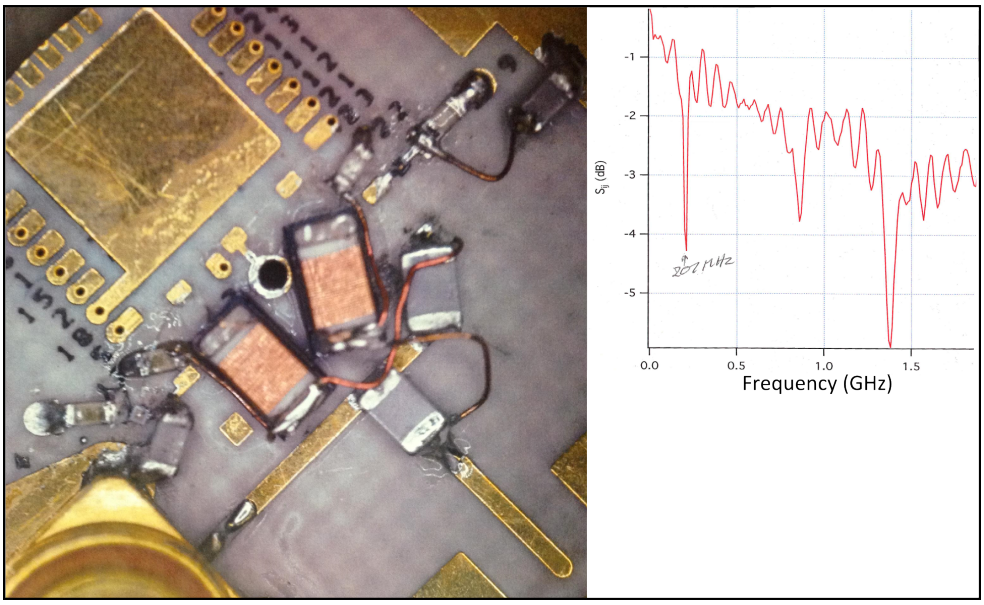

Figure 3.2 PCB tank circuit and Resonance Line
Image shows the circuitry of the tank circuit and line trace of the transfer characteristics. Resonance line is at 207MHz.

Because a large number of gate structures need to be written, I went to great lengths to ensure that this process was reliable and could be done with a minimum of effort. Testing showed that it was possible to write gates with a 20nm width and 20nm gap (40nm pitch) with ~70% reliability, however in the interests of making the process as foolproof as possible I ultimately decided on a 60nm pitch for the structure. The

structure itself consists of a set of interdigitated lines widened at one end so that alignment to the bond pad structure is easier later on.

One significant issue that was encountered at these very fine pitches is the high aspect ratio of the resist mask. This initially manifested itself as stray metallic filaments and mysteriously crooked or gapped gates on the surface of the chip (Figure 3.3). This was found to be due to the fact that the resist mask consisted of a series of upright "walls" that would fall over under some circumstances after the development process. To correct this problem, I modified our standard ZEP recipe to decrease its viscosity, resulting in a thinner layer after spinning. With this modification, the gate writing process was extremely reliable (~95%) and could be run after only a few minutes of setup.

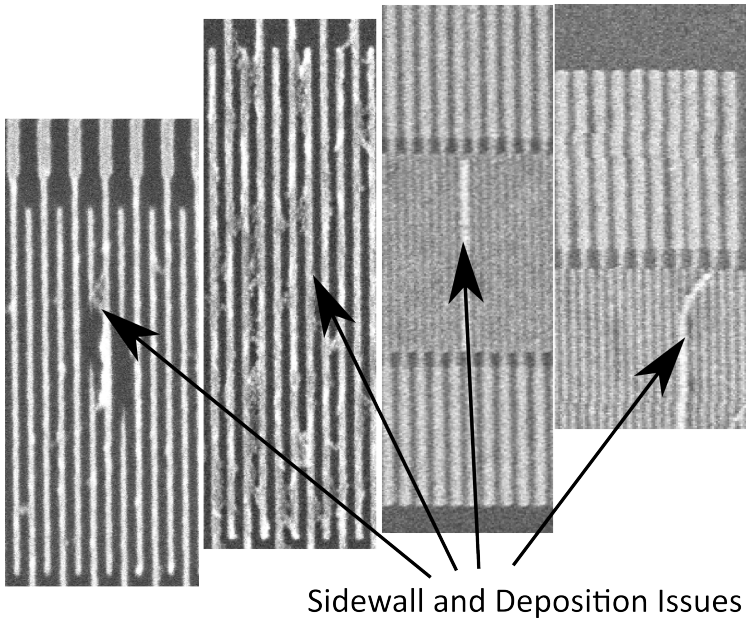

Figure 3.3 Sidewall and Deposition Issues
Filaments and gaps in gates as well as incomplete liftoff problems caused due to high aspect ratio resist mask and metal evaporation.

After writing and depositing gates, the "windows" were patterned over the interdigitated part of the gate structure across the full surface of the chip and a dielectric was deposited to electrically insulate the nanowire from the gates. ALD deposition was attempted initially, however problems with liftoff after this process prompted a change to sputtered SiN, which has less conformal coverage. Next, the nanowires were deposited on the chip and potential devices identified via imaging with SEM. This was by far the most time consuming and annoying part of the fabrication since it took ~2 hours of constant attention to image a full chip of devices. It was also one of the steps most likely to produce disorder and contamination since SEM imaging typically deposits some amount of amorphous carbon. This was minimized by taking only one single scan image of the device for placement of the pattern. Once the potential devices were identified it was possible to choose the best candidates and design the pattern that would connect to the gates and contact the nanowire. After writing and metal deposition it was possible to characterize the wires.

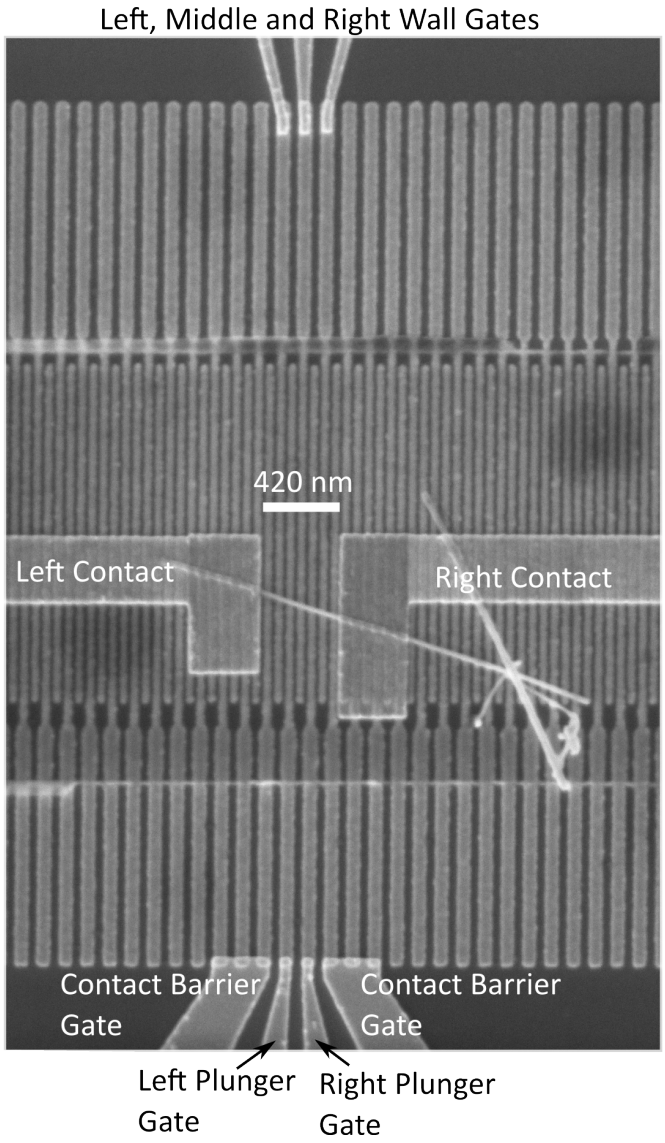

Figure 3.4 Completed Nanowire Device
SEM image of a completed bottom-gated nanowire device with Contacts and Gates labeled. The metal lines leading out of the image are connected to larger bond pads. Alignment between the two lithography steps was generally good enough to produce workable devices.

Electrical characterization of the devices was initially preformed using a cryo probe station with the sample under vacuum. However, the testing showed that the devices had very high resistances (order of MOhms) when they conducted at all. Two

possible issues suggested themselves, the first is that the contact leads themselves were broken as they ran over the edge of the dielectric "window" that covers the fine area of the gates. This was possible since sidewall deposition of the dielectric material would cause a raised lip, breaking the continuity of the metal lead. The other possibility was that contact to the nanowire was faulty either due to surface oxidation. To address the second possibility, a recipe was adopted that involved a brief hydrofluoric acid dip to remove the oxide, followed by immediate removal to an evaporator where metal deposition occurred. We also sought to increase the transparency of the contacts by changing the adhesion layer for the metal. To address the issue of metal continuity we tried performing a rotating, tilted evaporation to eliminate shadowing effects at the edge of the window. However, together these two fixes failed to establish good contact to the nanowires despite repeated attempts.

3.4 Conclusion

In conclusion, we developed a robust fabrication recipe for the production of bottom-gated devices, with extremely fine features for the formation and manipulation of quantum dots. We were unable to overcome difficulties in establishing good contact to the nanowires, which is not altogether surprising since several other groups have reported problems with establishing good contact to the nanowires. The small area available for contact and problems with the choice of contact metal and deposition method for the contact metal could also contribute to problems. For instance, one possible solution would be to use a sputtering system to etch the surface of the

nanowire and then immediately deposit metal, without breaking vacuum. These kinds of further efforts might prove successful in creating working devices and manipulating single spins.

Chapter 4

4. Graphene on Dielectric Micromembrane for Optoelectromechanical Hybrid Devices

4.1 Introduction

The ability to couple different quantum systems is of interest for several possible measurement, detection, and state manipulation schemes. Of particular interest are silicon nitride (SiN) membranes suspended in a Si frame. These membranes have exceptional mechanical quality factors and optical properties that enable an amazing level of control, for instance the ability to optically cool the membrane and manipulate its energy eigenstate. To create a hybrid device it is necessary to have efficient capacitive coupling of the motion of the membrane to an electrical system. To facilitate this coupling it is desirable to have a conductive coating on the membrane without impeding its mechanical and optical properties. For this

application, graphene is a very promising material. Its atomic monolayer nature produces a negligible impact on the mechanical motion due to its very low mass and its relatively high optical transparency does not impede the finesse of the optical cavity in which the membrane rests. The use of graphene as a transparent and flexible conductor is one of the most promising near term commercial applications of graphene so it is entirely appropriate that this project preceded the graphene photodetector work, where graphene is the active material.

In this project we compared SiN membranes with mechanical quality factors in the range of 10^6-10^7 and optical losses in the range of 10^{-5} (for near infrared wavelengths of approximately 930nm) [49], [50]. To explore the effect of a conducting layer we tested bare membranes (SiN), membranes with a thin layer of aluminum (SiN-Al) and membranes with a single layer of graphene (SiN-G) [51]. In the experiments the graphene shows superior electromechanical coupling without deteriorating the very desirable properties of the SiN membranes. Of note is the fact that the graphene is not contacted directly and acts as a floating gate. This eliminates the need to contact the graphene along with the inherent fabrication difficulties associated with that process. It also means that the inherent graphene properties can be utilized without worry about the contact resistance between the graphene and a metallic electrode [52].

4.2 Fabrication of Graphene on SiN membrane

We used commercial high and low-stress 50 nm thick Si_3N_4 membranes (Norcada, Inc.) for both the SiN and SiN-G resonators. Single layer graphene was grown on copper foil using standard CVD techniques [5]. The graphene-on-copper was spin-coated with a thin PMMA film, cut to an appropriate size; and the copper was removed by a wet etching processes. The graphene/PMMA film was then cleaned in a water bath and pulled out of the water using the SiN membrane. The water was carefully removed from beneath the graphene/PMMA membrane with an N_2 air gun and heated on a hotplate for ~30min. During this process it is critical to avoid capillary forces between the PMMA/graphene layer and the SiN membrane since they can easily crack the membrane as the water evaporates. Once the membranes were dry, the PMMA layer was removed via acetone vapor dip, again avoiding capillary forces, and the graphene was left on the surface of the membrane. The final structure is robust enough for subsequent fabrication steps, for instance electron beam lithography to define structures in the graphene. As an example, a sample was prepared with a hole defined in the graphene, centered in the middle of the membrane. This was done by spinning a layer of ZEP resist onto the surface of the SiN-G chip while being careful to avoid applying pressure to the membrane, then writing a circle using the Elionix lithography system. After development, the graphene was etched in an oxygen plasma and resist removed. The resulting round window of bare SiN could be used to pass an optical beam without even the minimal absorption of a graphene layer. Future devices could utilize patterned structures and gates that exploit plasmonic effects or allow the

creation of an integrated LC circuit on the SiN membrane. Devices where graphene is doped into a p-n junction are also an interesting future direction.

However, in these experiments a simple graphene covered membrane was used to evaluate potentialities and provide a baseline comparison (Figure 4.1 (b)) and the sample with an opening in the graphene was kept for future experiments (Figure 4.1(c)). The samples with an aluminum layer fabricated at DTU using standard clean room techniques. The high stress, stoichiometric SiN membranes were 100nm thick. The aluminum layer is 50nm thick, deposited via evaporation and subsequent lift-off. The Al layer is fabricated with a round hole in the center of the membrane for improved optical access. One problem with depositing a material on the SiN membrane is that it can significantly damp the drumhead motion of the membrane. To minimize this effect no aluminum was deposited in the region where the membrane joins the Si frame, since the mechanics of the clamping are critical to damping (see Figure 4.1(f)) [51], [53].

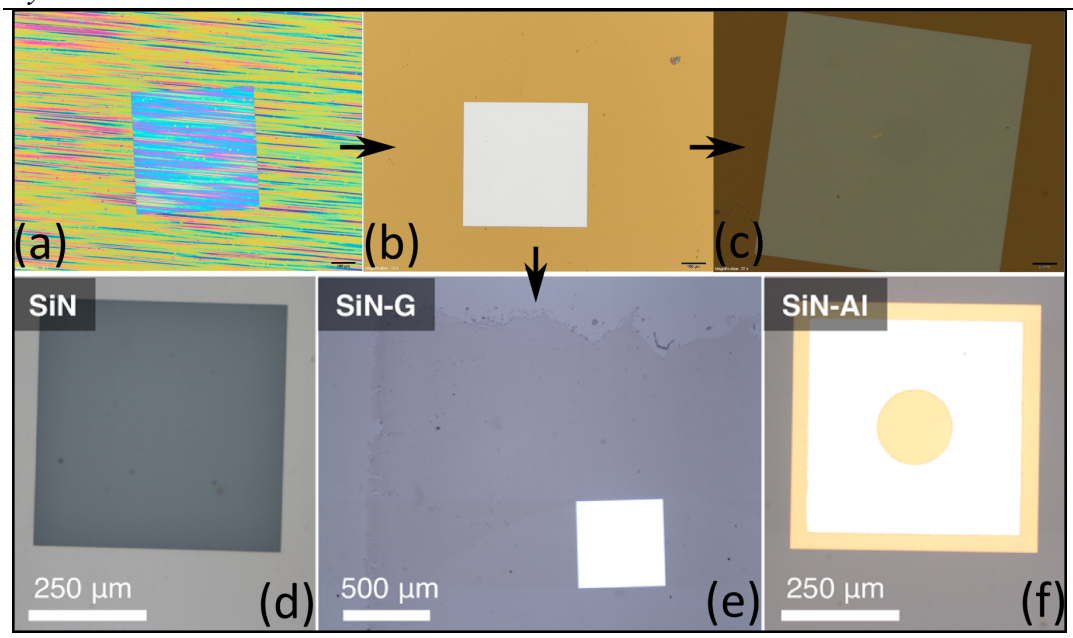

Figure 4.1 Graphene and SiN Membranes
(a) A bare SiN membrane is covered with the PMMA/CVD Graphene film using wet transfer techniques (b) after removal of the PMMA, the SiN-Graphene membrane is primarily transparent and one of these membranes was used in the experiments described (c) an additional membrane was patterned with a hole for optical access. A bare SiN membrane (d), a SiN-G membrane (e) and a SiN-Al membrane (f) were all tested in this experiment.

4.3 Experimental Setup and Measurement Apparatus

To electrostatically couple to the SiN membrane, a coplanar electrode chip is used, with electrodes in either a quadrant arrangement or an interdigitated geometry. The electrodes are depicted schematically in Figure 4.2. The electrodes were again fabricated with standard cleanroom techniques. They consist of 200nm of Au pattered via liftoff onto either a borosilicate glass substrate material or a standard Si chip with a layer of SiN to act as an insulator. The membranes are placed face downward onto this electrode chip, held above the surface using pillars that are either 600nm or 1um tall.

The pillars define a gap between the SiN membrane chip and the electrodes that is critical for the capacitive coupling. A measurement of the gap distance *d* was performed optically using a white-light interferometer (vibrometer MSA-500 from Polytec GmbH). In these measurements the gap distance ranged from 3.5 to 14um, a distance much larger than the height of the pillars designed to define the gap. The larger distance and variation in gap can be attributed to the unevenness in the electrode substrate due to dirt contamination and stress gradients causing warping of the substrate. In subsequent measurements the gap distance was gradually reduced to the height defined by the pillars.

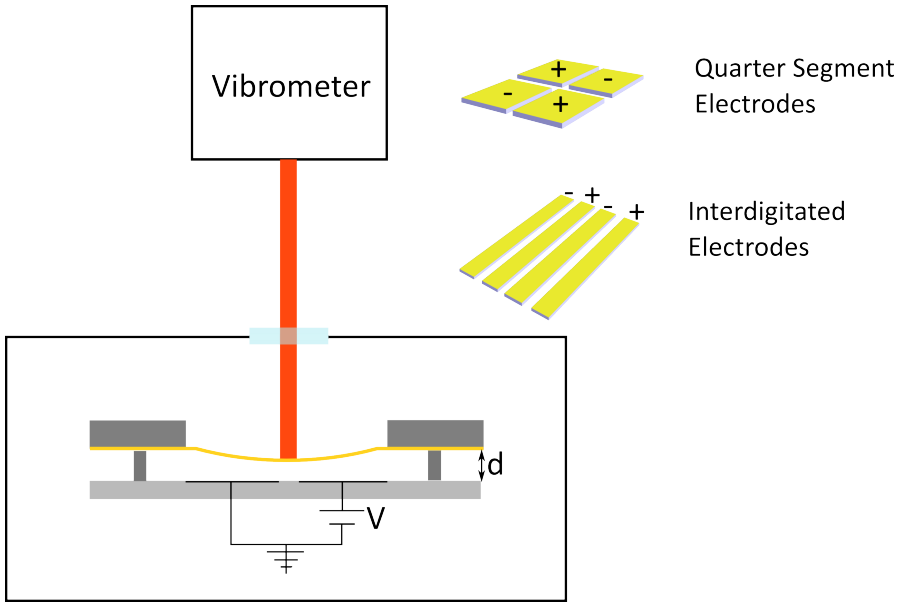

Figure 4.2 Schematic of Vibrometer Setup and Electrodes
The white-light vibrometer is used to measure the deflection of the membrane while the electrodes provide electrostatic control of the position, frequency and modes of the membranes.

The schematic of the experimental setup shows the basic arrangement of the chip and optical vibrometer used to measure deflections. The membrane-and-electrode sandwich is placed in a vacuum chamber, and the chamber is then evacuated down to 10^{-5} mbar to reduce viscous damping. The electrode array is connected to an external voltage source so that appropriate control potentials can be applied. For quality factor measurements, the membranes were placed on a piezoelectric stage to provide a vertical drive motion. The quality factors were extracted from the ring-down time of the membrane and the -3dB bandwidth of the resonance peak.

As mentioned previously, a key feature of these SiN micromechanical membranes is their quality factors that can reach several million. Such high quality factors are a requirement for strong optomechanical coupling. As a first step in our experiment we compared the quality factors of the SiN, SiN-Al and SiN-G membranes using the vibrometer. In the plot there are two groupings of the data in the vertical direction (quality factor), these two groups correspond to different loss regimes. The lower one corresponds to losses dominated by the clamping of the membrane chip to the electrode substrate, and the higher one to losses dominated by intrinsic flexural losses of the SiN membrane. In either case there is little to no difference between the bare SiN and the SiN-G membranes that were measured. The SiN-Al membranes show slightly lower overall quality factors.

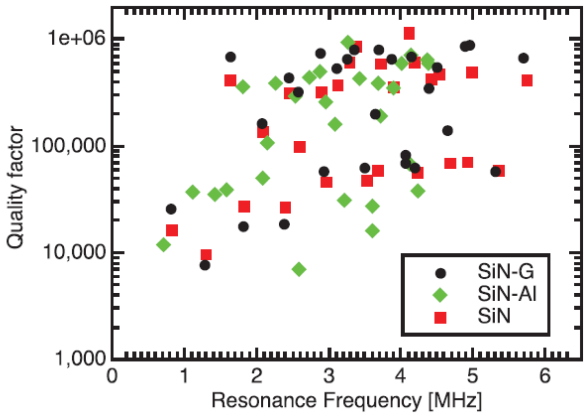

Figure 4.3 Scatter Plot of Quality Factors and Resonance Frequencies
There is virtually no difference between the SiN and SiN-G membranes performance characteristics. SiN-Al membranes tend to be slightly lower in quality factor.

The next portion of the experiment focused on the electromechanical coupling of the membrane's mechanical modes to an electrical circuit. For potential future applications it is desirable to make this coupling as large as possible. The electrostatic interaction for the bare SiN membranes occurs through the dielectric polarization forces [54], [55]. For both the SiN-Al and SiN-G membranes the electrostatic interaction occurs via the image charges on the conductors. Neglecting the effect of free charges on the membrane, the electrostatic force between either a dielectric or thin conducting layer can be modeled as:

$$F = cAf(d)V^2 \tag{4.1}$$

Where c is an electrostatic force constant characterizing the coupling, A is the area of the membrane, *f(d)* is a function describing the distance dependence of the

force with units of inverse area, and V is the potential difference between the electrodes.

In order to extract the value of the coupling constant c we measure the mechanical frequency shift due to the so-called spring softening effect, which causes a quadratic frequency drop when a DC voltage bias is applied (V_{DC}). The relative frequency shift is given by:

$$\frac{\Delta\omega}{\omega_0} = -\alpha V_{DC}^2 \tag{4.2}$$

Using α found from the frequency shift as a function of applied gate voltages we find the electrostatic force constant from the expression:

$$c = 2\alpha[-f'(d)]^{-1} h\rho\omega_0^2\eta^{-1} \tag{4.3}$$

Where h is the membrane thickness, ρ is the mass density of the membrane and η is a parameter of order unity for the spatial overlap of the membrane mode shape and the electrode pattern.

4.4 Performance Comparison

To quantify the performance of the SiN-G membranes compared to the SiN and SiN-Al membranes the response of the membranes when coupled to either the interdigitated electrodes or quadrant electrodes was measured. In the first set of measurements the SiN and SiN-G membranes were coupled to the interdigitated electrodes. In the second set of measurements the SiN-Al and SiN-G membranes were

coupled to the quadrant electrodes. This was done in an effort to compare the responses of the membranes with the geometry of electrodes that should give the best response for that coupling mechanism (dielectric polarization or metallic image charges).

By applying a DC voltage to create a spring softening curve, we can extract the parameter α and from that calculate the electrostatic force constant c using the equation above. The resulting average force constants for the bare SiN and SiN-G membranes on the interdigitated electrode array are shown below. To extract a value for α, the distance dependent function *f(d)* for the interdigitated electrodes is given by:

$$f(d) = A_0^{-1} e^{-\kappa d} \tag{4.4}$$

Where A_0 is a scaling constant, and κ is determined numerically for our setup to be $\kappa = 1.05 \mu m^{-1}$. In Figure 4.4, SiN-G membranes are seen to outperform the bare SiN membranes by a factor of 5.5. For comparison, horizontal lines indicate a theoretical value of the performance of both dielectric and conducting membranes. The SiN-G membrane clearly falls within the expected value for a conducting membrane. The same analysis is performed for the quadrant electrode geometry and the SiN-Al membrane, but only the value for a conducting membrane is relevant in this case. For this electrode geometry the distant dependent function is given by:

$$f(d) = 1/d^2 \tag{4.5}$$

This equation is valid as long as d is smaller than the inter-electrode gap. The error bars on the measurement are due to uncertainties in the gap distance d and the lateral misalignments between the electrodes and the membranes.

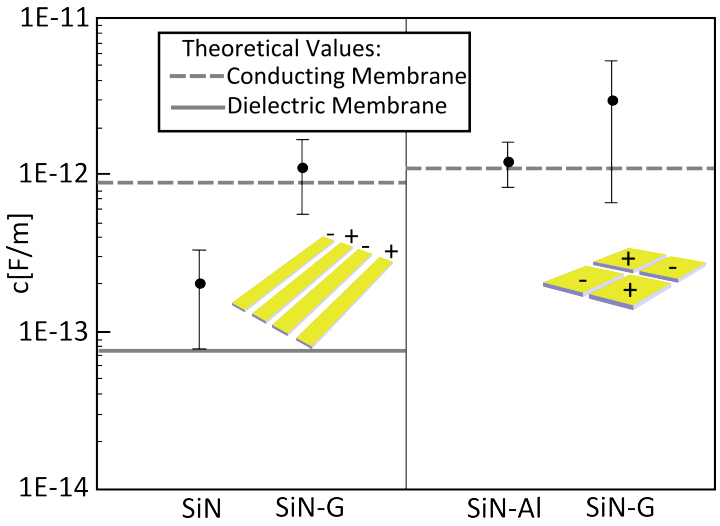

Figure 4.4 Performance Comparison for Membrane Types
SiN-G membranes show a considerably larger coupling constant compared to SiN membranes and are comparable to SiN-Al membranes.

4.5 SiN-G Conclusions

In conclusion we have shown that SiN-G membranes are promising candidates for future optoelectromechanical experiments. The enhanced electromechanical coupling of the conductive membrane as opposed to the dielectric membrane is beneficial for integration into electrical readout circuits [55]. Additionally, the graphene does not degrade the mechanical properties of the membrane, which can be a problem for metallic coatings.

Chapter 5

5. Graphene for Optical Detection and Imaging

5.1 Introduction

Several previous experiments have investigated graphene's optoelectronic properties and in particular the photoresponse of junctions created either electrostatically or via contact doping effects [56]–[58]. In particular, the response at optical and near IR wavelengths was studied for potentially applications to ultra-fast detection of optical modulation. However, since the sensitivity of these devices is limited, they are not well suited for imaging applications. Existing Si based charge transfer devices have very high sensitivities at optical and some of the near-IR wavelengths [59]. In order to replace this technology, graphene must offer some other advantage, either in terms of architecture or performance. This is a difficult criterion to meet since the existing Si processing and design has been optimized for several decades. The two fundamental parameters where graphene does exceed Si is its mobility, which has been measured to be ~100,000 cm^2/Vs for exfoliated samples on

boron nitride substrates [60]. The other is the broadband absorption characteristic of graphene, which hardly varies from UV to far-IR, while Si is limited by its bandgap to wavelengths shorter than ~1μm.

5.2 First Attempts and Devices

Our first attempt to utilize the properties of graphene was in an architecture where a localized p-n junction was created at the intersection of two gates. Based on previous experiments with electrostatically gated samples, it was known that a localized response could be generated in the vicinity of a p-n junction [57]. Additionally, theoretical understanding of the mechanisms behind the photocurrent generation pointed toward even greater possible sensitivities [61]. Our concept was to create an array of intersecting gates that could be turned on and off independently. Wherever two "on" gates crossed, a p-n junction would be generated. This has advantages over a standard CCD array where each pixel line must be read out individually and sequentially. For instance it might be possible to do novel detection and processing of multiplexed optical signals, each wavelength sent to a different point on the array.

Because I was primarily interested in this as a potential technology, I wanted to move away from the exfoliated graphene samples that had been used in almost all of the previous experiments. Recent advancements in graphene synthesis had enabled the growth of graphene on Cu foils [5], and work at MIT had been successful in producing a large area monolayer graphene using these CVD techniques [62]. Significant

challenges remained in the fabrication of structures, especially since in early samples the doping and surface characteristics of the graphene were not as pristine as in the exfoliated samples. After beginning a collaboration with Yong Cheol Shin, a graduate student in Jing Kong's group at MIT, I was able to transfer graphene onto standard Si/SiO_2 substrates, and fabricate basic devices.

5.3 Basic Transfer Recipe

Transfer itself is a complicated and delicate process that requires careful control to get reproducible results. It is crucial enough that I will devote a small amount of space here to explaining the process, and some of the important factors that go into successful transfers. The starting point is a Cu foil with monolayer graphene grown on its surface via a CVD technique. The growth itself is something that I have never done personally, but I have a relatively detailed understanding of the process through numerous conversations.

1. Place the Cu foil onto a backing material such as 0.5mm thick PET film. The PET film should be slightly larger than the copper foil piece and rigid enough to avoid bending or warping during the spinning process.

2. Take the copper foil on top of the PET film, and place on top of a sheet of weighing paper. Tape around the borders of the copper foil with a ~2mm overlap, using scotch tape. Be careful that the scotch tape seals down to the surface of the copper foil

3. Spin-coat the surface of the stack with A4 PMMA, spun at 2500rpm for 60sec.

4. Place in vented curing oven at 75°C for 10min to bake the resist.

5. Cut out the middle copper foil with the PMMA on the surface. Cut at the boundary of the scotch tape, slightly inside so as not to waste the foil. Remove the copper foil from the PET backing, handling it by the edges.

6. Place into an O_2 plasma stripper (Technics Plasma Stripper). The chamber should have been conditioned for ~5min before running the etch recipe. Etch the sample for 3min at 230mTorr/100W/8sccm O_2. After this step sample can be left for several months without significant deterioration.

7. Cut out an appropriate sized piece of the copper foil for your substrate.

8. Place in a petri dish of ferric chloride copper etch (Transene) for 45min

9. Rinse by transferring the PMMA/graphene film between two dishes of DI water, replacing the water each time. Transferring can be done by using a piece of Si wafer to gently scoop up the film, making sure

that the film does not completely touch the surface of the wafer (maintain a water bubble underneath).

10. Place in dilute hydrochloric acid for 45min, then rinse as before.

11. Pickup your film with your substrate, make sure to align it correctly and begin applying gentle pressure with an airgun. Water should be slowly squeezed out from underneath the film and progressively more force can be applied with the airgun. Color changes indicate the final water being removed, but keep applying pressure for a few minutes after that.

12. Bake the sample at 75-100°C for 30min to drive off remaining water and relax the PMMA onto the substrate.

13. Heat acetone to 80°C so that vapor layer rises in a tall beaker. Dip the sample in and out of the vapor boundary to dissolve the edges of the PMMA. If this is not done the PMMA will tear the graphene as it dissolves.

14. Place in hot acetone for 1min, then cold acetone for 10min. Rinse in IPA and blow dry.

After transfer of the graphene layer standard fabrication can be performed although there are a few restrictions that must be observed. First is that photoresist will

dope the graphene significantly so in the event that photolithography is necessary the graphene must be protected with a PMMA layer. Second the graphene can occasionally have adhesion problems to the substrate, especially if further materials are deposited on top of the graphene. It is thus best to avoid depositing high stress materials such as Pt directly on the graphene. Even with relatively low stress materials such as Au, occasionally delamination would occur.

Measurement of transport characteristics using the global Si backgate showed that the graphene tended to be p-doped immediately after transfer (charge neutrality point shifted to large positive voltages). We attempted to remedy this by n-doping the graphene with a layer of ALD Al_2O_3. Previous work on exfoliated samples used nitrous oxide to p-dope the graphene and counter the n-doping of the Al_2O_3, leaving the graphene near neutral with minimal overall doping [63]. By skipping the nitrous oxide, we hoped to counter the effect of the p-doping from the transfer.

The approach was only marginally successful and ended up creating very unpredictable results where the graphene would end up either heavily p or n doped. However, a handful of devices were produced with a single set of crossed gates and contacts at each of the corners.

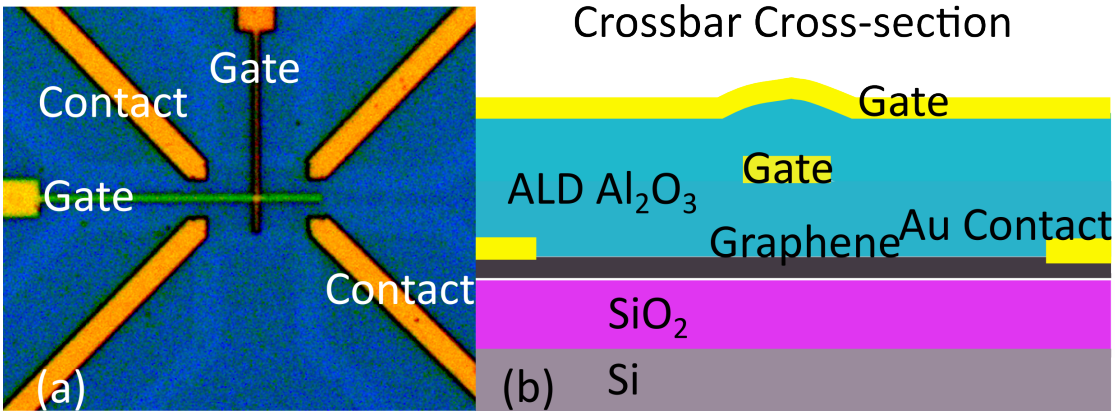

Figure 5.1 Crossbar Device Optical Image and Cross-Section
(a) Optical image of the crossbar device with contacts in each of the four corners of the graphene rectangle and two crossed gates in the middle of the rectangle, separated with ALD layers. (b) Cross-Section showing the contacted graphene covered with ALD and crossed gates.

Heat cleaning of the graphene was attempted in the nanotube growth furnace by heating the sample to 300C under an Ar atmostphere for approximately an hour. It was hoped that this would improve the reproducibility of the graphene doping by removing the volatile dopant material. Unfortunately, testing of these devices showed that they would easily develop leaks to the backgate through the SiO_2 layer. This appeared to happen at the bond pads where the bonder had subjected the substrate to mechanical force. Not all of the devices failed in this manner, but the number of failures indicated that heat cleaning was problematic. From the devices that did survive photocurrent maps were taken in the optical scanning confocal laser setup. This setup allows a diffraction limited laser beam spot to be scanned over the surface of the sample while its electrical response is characterized. For these measurements a supercontinuum laser source (Fianium FemtoPower 1060 Supercontiuum Laser

Source) was used to illuminate the sample and the zero bias current measured with an Ithaco (DL Instruments Model 1212 Current Preamplifier).

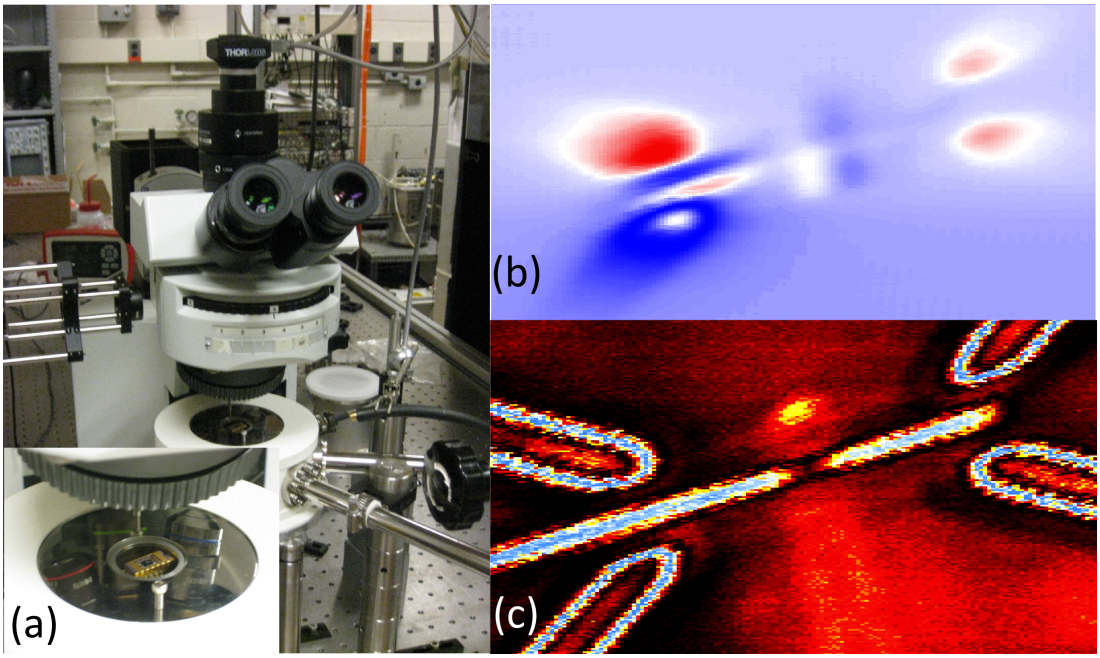

Figure 5.2 Optical Scanning Microscope and Photocurrent Images
(a) Scanning optical laser microscope, inset shows the sample mount inside the cryostat (b) Photocurrent map of the crossbar device (c) Reflection map of the device taken during the photocurrent map.

The photocurrent maps clearly show that there is a local response in the vicinity of the gates and at the contacts. Response at the contacts is due to the doping effect that the contacts have on the graphene [64]. In the initial scans of the device this contact doping created a larger signal than that produced by the electrostatic gates. However, a second generation of devices showed that a semi-isolated pixel could be created where the two top gates on the device intersect over the graphene. One potential issue with this kind of response is that the strongest positive and negative

response was generated in the same vicinity. To make the response measurable in full-scale imagers some kind of mask would have to be applied so that both areas would not be illuminated equally.

5.4 Photodoping

An unfortunate effect that was observed in these measurements is the progressive photodoping of the sample under illumination with the supercontinuum source. Because the source is pulsed it has a high peak-intensity and even when the selected wavelength is in the red part of the spectrum around 600nm, illumination can cause charge traps to screen the electrostatic field from the gates. This effect has been observed in a large variety of graphene samples in our group and although the exact details of the doping are not known, it is a consistent effect. Heating the sample and waiting several hours or even days can allow the charge traps to relax and undo some of the photodoping but it is often difficult to fully recover the properties of our devices and the same position of the Dirac point. The photodoping has the effect of weakening the p-n junction in the graphene and making the signal weaker with progressive scans.

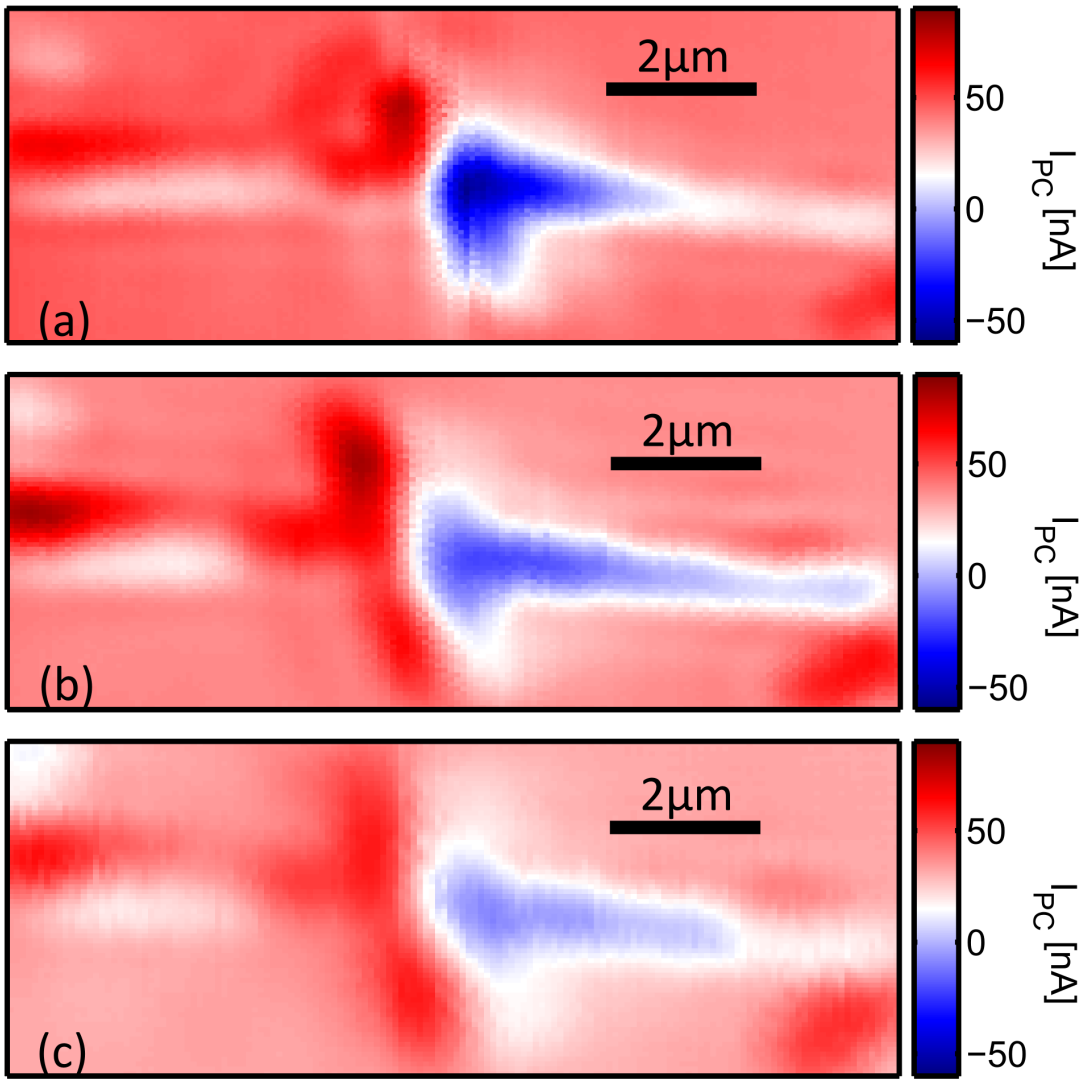

Figure 5.3 Photodoping in Crossbar Device

Scans are taken measuring current between diagonal contacts (upper left and lower right). Vertical gate biased to 2V and horizontal gate biased to -2V (see Figure 5.1) and the laser power was measured at 1.0mW. (a) The first scan shows the strongest response with positive and negative maxima next to the crossing points of the gates. (b) Next scan shows significantly smaller response and (c), taken after several scans, shows a further decreased response. This decrease is attributed to photodoping of charge traps in the oxide screening the electrostatic gates, decreasing the strength of the p-n junction in the graphene.

5.5 Stepping Pixel

The results of this round of experiments convinced me that a more reliable geometry and fabrication recipe had to be developed for a realistic imaging device to succeed. One key advance that was made at this time was the long desorb for cleaning of the graphene. By leaving the PMMA/graphene layer floating in DI water for 24-48 hours many of the surface contaminants are removed from the surface and the doping is drastically reduced, while the mobility increases significantly. The ability to virtually eliminate doping effects obviated the need to perform ALD Al_2O_3 growth on the graphene for the purpose of shifting the charge neutrality point and dramatically increased the reliability of the transfer process. As a result a different approach, using bottom gating was developed. This fabrication shared many of the characteristics that were employed for the Si-Ge nanowire experiment, in that only minimal fabrication was actually preformed after transfer of the graphene.

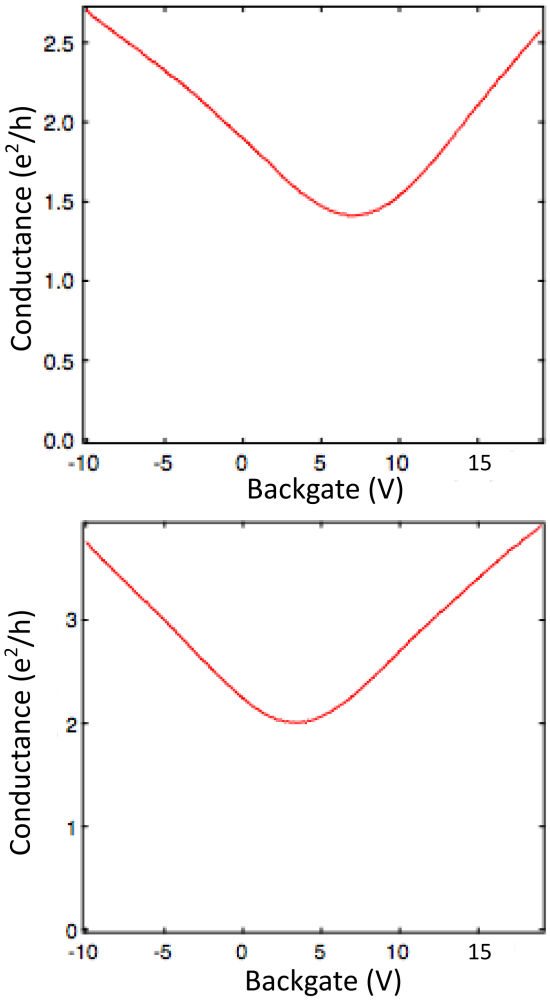

Figure 5.4 Graphene after Long Desorb
After a long desorb these two samples showed extremely low doping and a significantly higher mobility, on the order of ~1000 cm^2/Vs

The geometry of the device was also changed to so that a series of parallel gates lies underneath the graphene, separated by a dielectric layer. By biasing progressive sets of gates it was possible to create a p-n junction at different points along the graphene. By cutting the graphene into parallel ribbons and contacting each ribbon individually, it is possible to create a 2D array of pixels that can be turned on

and off sequentially. The disadvantage of this kind of geometry is that the resistance through the length of ribbon can become a limiting factor in the measurement. However, for small devices this is a not significant problem.

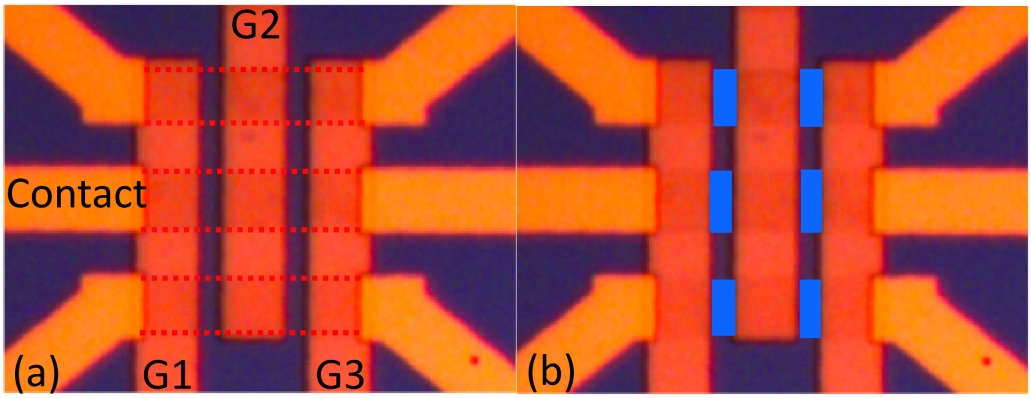

Figure 5.5 Optical Image of Multipixel Device
(a) Three buried gates (G1, G2 and G3) deposited on the chip, covered in ALD Al_2O_3, graphene transferred to the surface, contacts deposited, and the graphene etched into ribbons (ribbons outlined in dotted red). (b) The pixels are indicated by the blue squares, they are created when the buried gates can gate the graphene ribbon into a p-n junction.

Fabrication consisted of:

1. Patterning and deposition of metallic gates
2. Deposition of ALD Al_2O_3 dielectric
3. Transfer of CVD grown graphene
4. Patterning and deposition of Ti/Au contacts
5. Patterning and etching of the graphene into ribbons

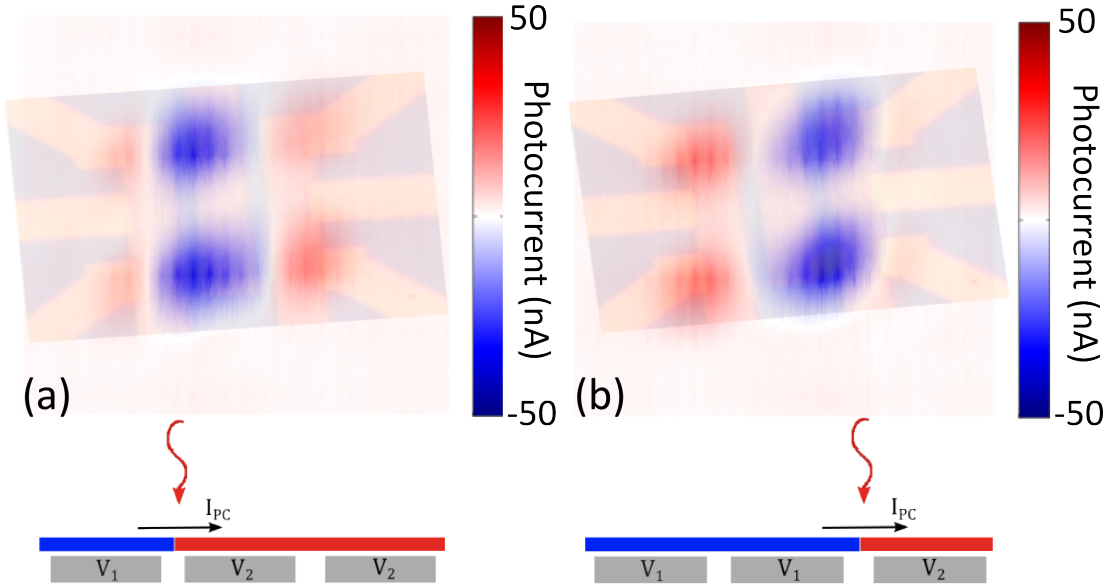

Figure 5.6 Optical Photocurrent from Multipixel Imager
Measuring current from the first and third graphene ribbons, image of the device is overlaid for reference (a) Photocurrent map when the first and second set of gates are biased to create a p-n junction, V_1=7V and V_2=0V, turning on the first column of pixels (b) Photocurrent map when the second and third set of gates are biased, turning on the second column of pixels.

The approach convinced us that this was a viable path forward, however for optical and near-IR measurements the novelty of the approach was not enough for a full line of research. However, since the mid-IR was a relatively uninvestigated part of the spectrum, we began planning for setup similar to the optical scanning microscope, but designed to operate in the mid-IR.

5.6 Considerations in Designing for Mid-IR Experiments

Several factors were considered in the design of this setup. First was the fact that since the wavelength is increased by an order of magnitude over the wavelengths in the optical setup, many physical dimensions must also be increased. In particular,

the scan area must be large enough to accommodate devices with dimensions that are an order of magnitude larger since the diffraction limited beam spot is that much larger. So while the optical setup typically has a maximum scan area of tens of microns, the mid-IR microscope needed to have a scan area on the order of millimeters. To accommodate this scan area, we substituted a galvo cube for the peizo-controlled mirror that was used in the optical setup. The galvo cube consists of two mirrors mounted at right angles to each other, with orthogonal axes of rotation. Each mirror is mounted to a galvonometer that provides precise angular positioning in response to a voltage signal. An optical encoder in the galvonometer itself minimizes hysteresis and stabilizes the positioning of the mirror. In our measurements we never noticed any noise or jitter in the mirror position, however, our experiments were relatively insensitive to position and our resolution much poorer than optical experiments. To ensure good reflectivity of the mirrors, uncoated Au-plated mirrors were selected as the optimal option for the galvo cube since other mirror types typically have some sort of protective coat to prevent oxidation, and this coating was potentially absorptive in the mid-IR.

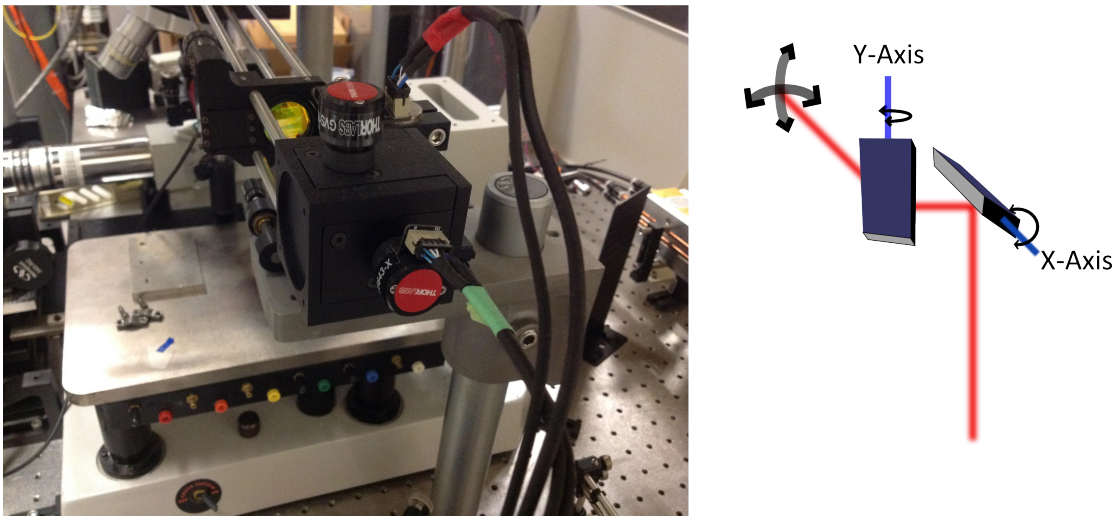

Figure 5.7 Galvonometer Cube and Schematic
Picture and schematic of the galvonometer cube used to produce angular deflections of the laser beam. The center of the deflection should be at the focal point of the first of the confocal lenses (visible just above the housing of the cube). This geometric placement ensures the beam translates within the cage optics but remains parallel to the axis of the cage between the two confocal lenses.

Another consideration was the absorption of the optics. Wavelengths in the mid-IR are typically highly absorbed in SiO_2 (glass) and many plastics also have absorption lines at inconvenient wavelengths. There are several different material choices that are used in the mid-IR. First, metallic salts such as sodium chloride, calcium fluoride, or cesium iodide have good transmission in the mid-IR and are relatively cheap but they are unfortunately highly hygroscopic and will quickly start to pit and dissolve as atmospheric humidity is absorbed. Zinc selenide lenses are not hygroscopic and have good transmission, but they are significantly softer than other optical materials and can have internal stress, especially along their perimeter. Care must be taken not to drop these lenses on any hard surface from any height or they will

chip or shatter. The final category is semiconductor materials such as germanium or silicon, unfortunately these materials are opaque to visible light and are thus not feasible for beam paths where both mid-IR and visible light must be transmitted.

For our setup we chose to use ZnSe lenses, since they posed the fewest compromises. For good transmission in the mid-IR, all of the optics must be anti-reflection coated for the appropriate wavelength regime. This is far more important in the mid-IR than for visible wavelengths since large amounts of the laser power can be lost due to reflection and scattering at the lenses. The wavelength regime that we selected was 7-14μm for the anti-reflection coating.

During the selection of the laser, we took into account the large amount of loss that is typical in mid-IR setups. The two primary types of lasers that we considered for use in our set were quantum cascade lasers (QCL), which are solid state, and CO_2 lasers, which are gas based, cavity lasers. Each has advantages and drawbacks in designing a setup. QCL's are first of all much more expensive than other sources, with prices around $20,000-40,000 at the time of our research for the setup. The prices are decreasing which might make this a more viable choice in the future. The advantage of the QCL sources is that they can often be tuned in wavelength across a relatively large band by controlling their operating temperature very precisely [65]. This ability makes them very attractive for spectroscopy experiments, and several different QCL sources, each covering a different wavelength band, can be linked together to form a source capable of tuning from near to far IR. The power emitted by these sources is much

smaller than from CO_2 lasers, on the order of tens of milliwatts, so it's necessary to be extremely careful during the design stage to consider how much power will actually reach your sample. Based on our experiences, it is difficult to get more than ~10% of the entire laser power through the optics and down to the sample.

The other source that is typically available at these wavelengths is a CO_2 gas laser. The primary use of these lasers is for industrial cutting purposes. The problem that we encountered was thus the opposite as for the QCL sources; it was actually difficult to find a company that supplied a laser with less than a 10W output. Typically, the lasers that we encountered were designed to output between 1kW and 100W. This is obviously far too much for our purposes and would be extremely dangerous to work with. The costs are substantially lower, with a reasonable laser costing between $2,000-7,000.

The laser that we ultimately selected was a power-stabilized 1W laser from Access Laser (model L4S) with water-cooling to provide more precise mode and power stabilization. This laser, along with a peltier based water-chiller unit, were the primary single item costs of the setup (Figure 5.8). Many other parts were scavenged and/or borrowed but total costs for the setup were around $14,000.

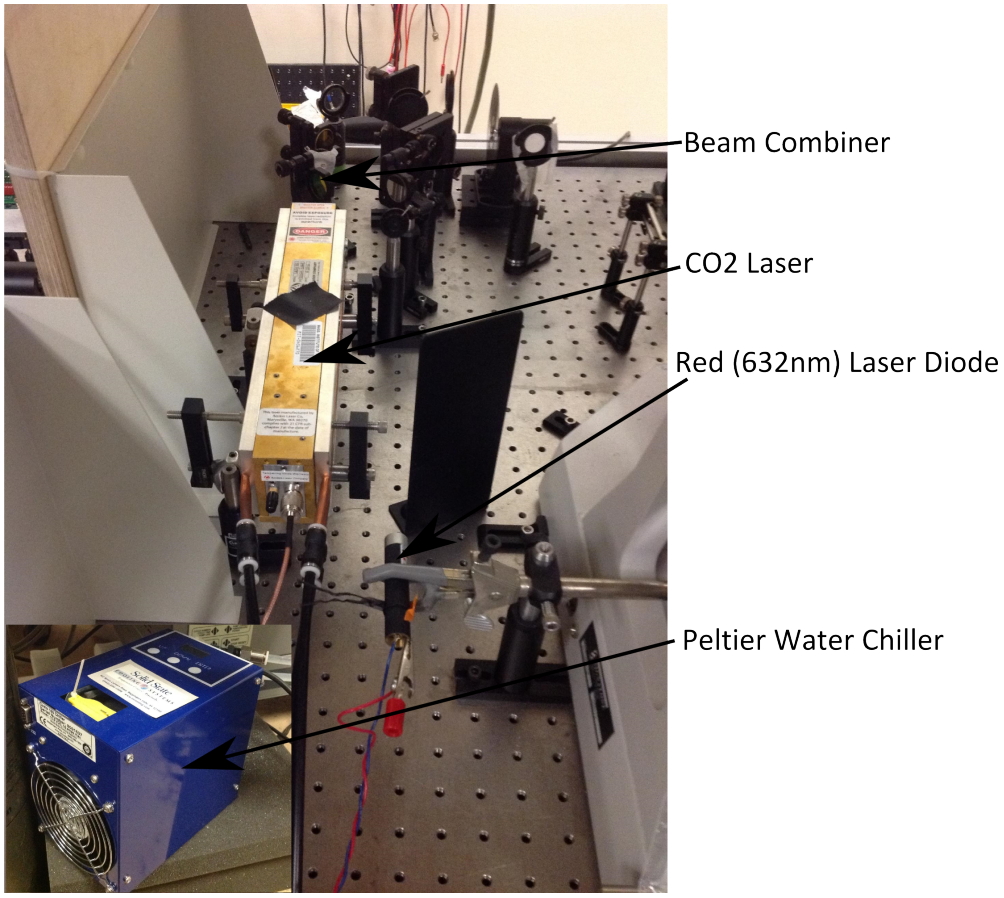

Figure 5.8 CO_2 Laser and chiller
CO2 laser and 632nm laser diode are mounted side by side and optics at the top of the picture combine the two beams and attenuate the CO2 laser power to avoid damaging optics later in the beam path. Inset shows the water chiller that stabilizes the water temperature in the cooling loop to within ~0.1°C of the target temperature (normally 20°C).

One of the primary problems encountered in assembling the setup was the difficulty in aligning and monitoring an invisible laser source. While there are viewer cards for near-IR wavelengths, the sensitivities of these cards are normally limited to wavelengths shorter than 1.5μm. The options for viewing the 10μm are much more limited and generally quite expensive, the whole reason that we were researching this

wavelength range. Instead, thermally sensitive paper (used in thermal printers) was used to detect the heating that occurs at the focal point of the laser. Use of apertures also improved the alignment process. However, to guide the laser through the glavo cube and subsequent lenses it was necessary to add a co-linear visible laser (630nm). This was done with a beam combiner optic from ULO Optics, this optic reflects 10μm and passes 600nm light with very little loss. After this addition, alignment was considerably easier. A summary of the experimental setup and techniques is also included in Section 6.4.

5.7 Initial Mid-IR Experiments

Initial experiments were done with a variety of different devices as we sought to identify the signal and response at these wavelengths. Several contact-doping devices were measured as a first step, since these will generate signal without the application of any gate voltage. Signal from these devices was extremely weak, but did convince us that we were seeing signal from the laser excitation. However, to be sure that the response was due to graphene it was necessary to test that gating the graphene would alter the signal strength. Using a simple two contact device with a global backgate we were able to show a large response as the graphene was gated to large positive voltages.

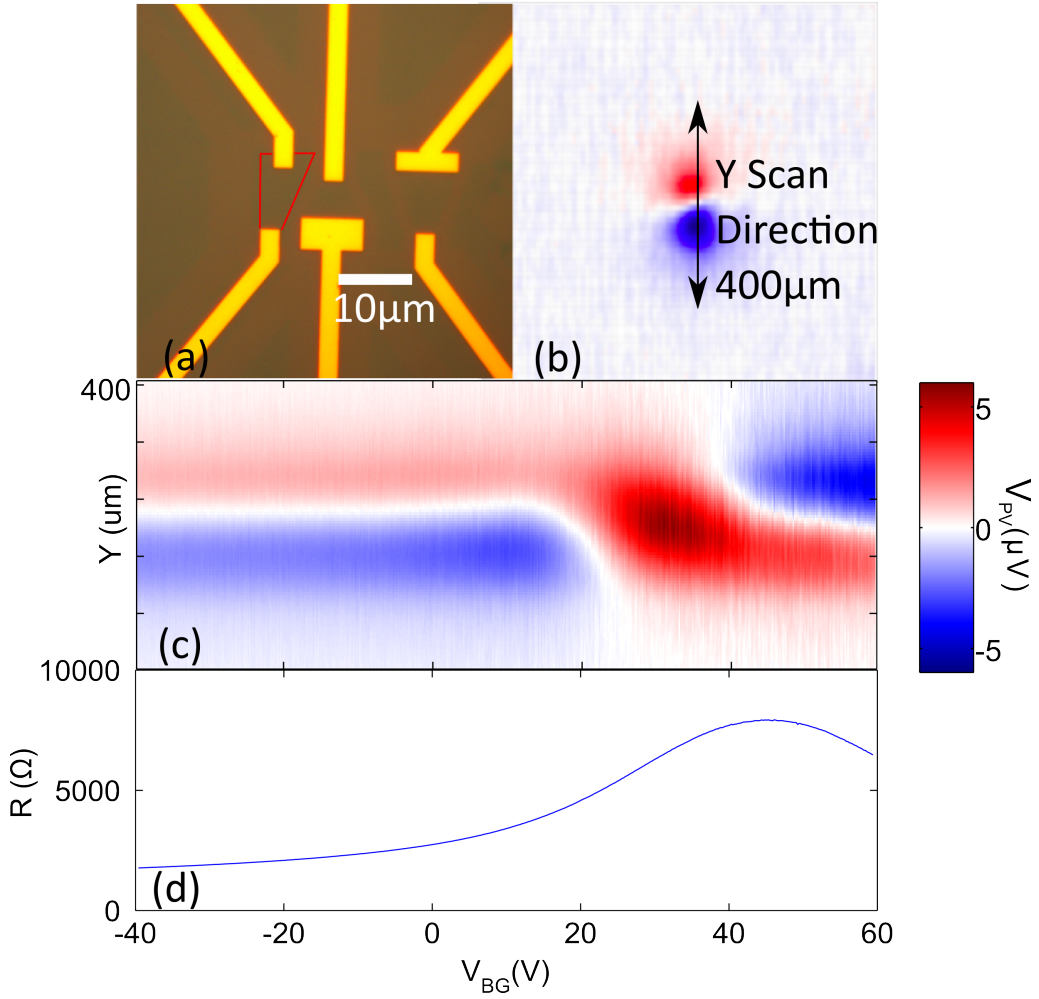

Figure 5.9 Initial Mid-IR Scan of Two Contact Device with Global Backgate
(a) Optical image of the simple two terminal device with graphene strip outlined in red. (b) A photovoltage map of the device showing the strong response in the vicinity of the device with the scan line indicated. (c) A measurement of the photovoltage, the y-axis is the spatial scan direction and the x-axis is the backgate voltage. (d) Resistance of the device as a function of the backgate voltage.

This was a convincing demonstration that the graphene was involved in the primary signal generation mechanism since no other material in the device would be altered by the application of the gate voltage. The next step was to determine the

response of a p-n junction to illumination. Based an inventory of devices that we had fabricated previously we tested a simple rectangular graphene device with contacts at each edge and a buried gate that controlled half of the device. The other half of the device was controlled by the global backgate, and the graphene was exposed on the surface (no dielectric coverage). Figure 5.10 shows the layout of the device.

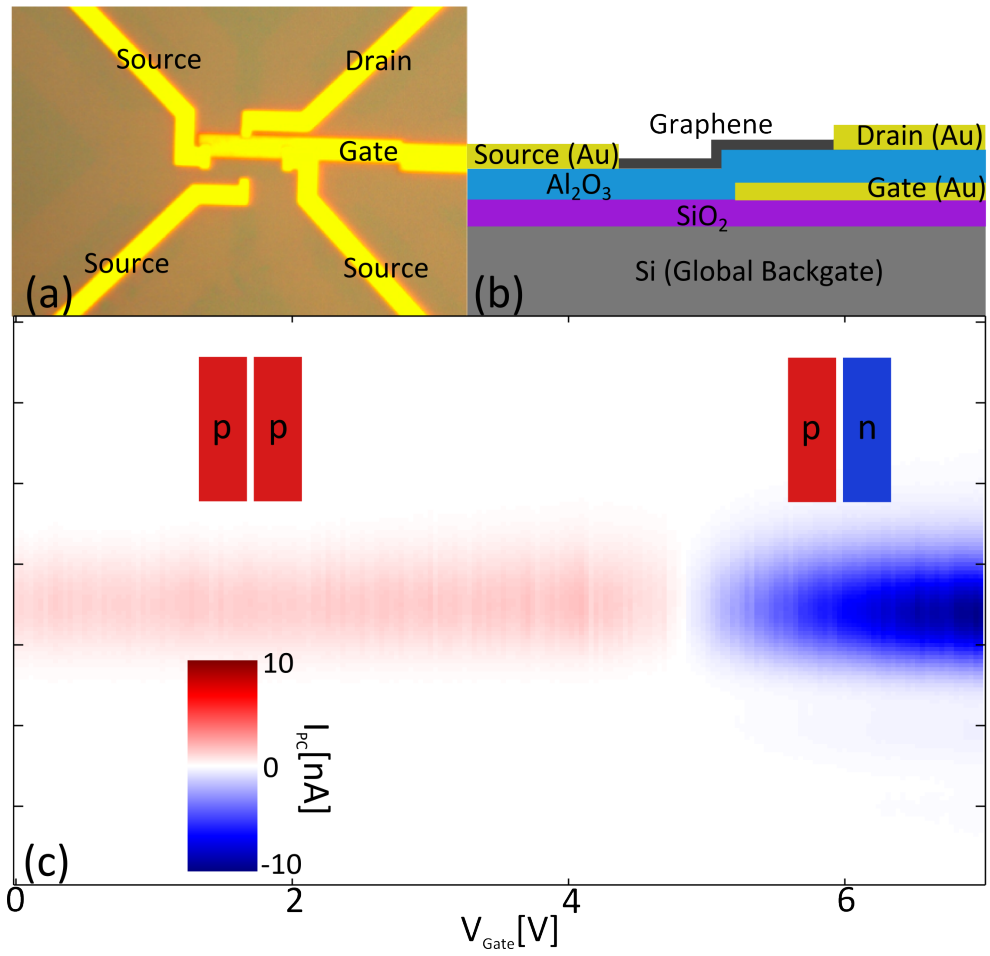

Figure 5.10 Optical Half-Gate Device
(a) Optical image of half-gate device (b) Cross-section schematic showing gates and contacts (c) Spatial line cut through the device on the vertical axis, local gate voltage on the x-axis. Response increases dramatically as p-n junction is formed.

The response of this device was significantly larger than from the simple two terminal device and was dramatically enhanced when the device was gated to form a p-n junction. The dimension of the graphene rectangle was 5x10μm so the device was significantly sub-wavelength. Although this might have significant applications in the future, for the purpose of the experiment we were unable to determine exactly the mechanism and cause of the photoresponse. In particular, it was impossible to separate the response of the contact-graphene junction from the electrostatically gated junction. In order to better determine the mechanism of the response and how it differed from the optical response it was necessary to better understand what portions of the device contributed signal and how that signal varied with gate voltage, temperature and design of the device.

To address these problems we created a scaled-up version of our device with two split buried gates and a length of ~200μm. This allowed the signal from the p-n junction in the middle to be clearly separated from the contact junctions at the ends of the device. Initially we also included additional side contacts to make simultaneous 4-point probe measurements. However, after trying to perform measurements with these devices we fond that it the extraneous contacts made the measurement significantly more complicated, making us uncertain about the circuit pathway that was being investigated and the additional contacts were prone to failure. In subsequent devices they were eliminated.

5.8 Conclusions

Based on the initial data gathered from these devices we were able to determine that the photoresponse of the device was thermoelectric in nature, however we were unable to determine exactly where the radiation was absorbed and how much energy was directly deposited in the graphene. We also sought ways to increase the sensitivity of the device. Since the device was behaving thermoelectrically in response to power deposited, it was crucial to understand which materials were limiting the thermal conductance. Finally, we needed to determine under what conditions the response was thermoelectric and if photovoltaic mechanism started to compete in certain regimes.

Chapter 6

6. Electrically Tunable Ambipolar Infrared Thermocouple

6.1 Introduction

We explore the photoresponse of an ambipolar graphene infrared thermocouple at photon energies close to or below monolayer graphene's optical phonon energy and electrostatically accessible Fermi energy levels. The ambipolar graphene infrared thermocouple consists of monolayer graphene supported by an infrared absorbing material, controlled by two independent electrostatic gates embedded below the absorber. Using a scanning infrared laser microscope, we characterize these devices as a function of carrier type and carrier density difference controlled at the junction between the two electrostatic gates. Based on these measurements, conducted at both mid- and near-infrared wavelengths, the primary detection mechanism can be modeled as a thermoelectric response. By studying the effect of different infrared absorbers, we

determine that the optical absorption and thermal conduction of the substrate play the dominant role in the measured photoresponse of our devices. These experiments indicate a path toward hybrid graphene thermal detectors for sensing applications such as thermography and chemical spectroscopy.

6.2 Graphene in Mid-IR Detectors and Devices

Exploring photoactive materials and devices in the mid-infrared (MIR) regime has garnered tremendous recent attention because the IR spectrum ($0.08 < E_{ph} < 0.25eV$) is an energy band useful for many technologies ranging from thermography and night vision systems to nanoscale chemical spectroscopy[66]. In atomically thin monolayer graphene (MLG), broad band photo-detectors and optical modulators have been demonstrated in the *near* infrared (E_{ph}=0.8-1.6eV), and have been shown to be capable of ultra-fast response times (>10GHz) [67], [68]. However, these experiments focused on photon energies that are much larger than the intrinsic energies of the system, such as the optical phonon energy ($E_{op} = 0.2eV$) or the electrostatically controllable Fermi Energy of MLG ($E_f \approx 0.5eV$) [20], [57], [68], [69]. For MLG photo-excited in the MIR, very recent work has shown active modulation due to Pauli blocking [70], [71] as well as interesting plasmonic effects [72]–[74]. Many experiments have begun to explore MLG's unique opto-electronic properties while attempting to make use of its unusual broadband optical absorption from the far-infrared all the way to the visible [22], [75]–[79]. However, unlike detectors for visible wavelengths, which predominately operate using photovoltaic effects, detectors

for infrared wavelengths can operate either by photovoltaic or thermal effects [80]. Therefore, distinguishing the physical photo-detection mechanisms at low energies is critical for illuminating MLG's potential role as a MIR photodetector.

Unlike photovoltaic detectors where only photons absorbed by the active material (MLG) can generate a signal, here we find that MLG acts as the key element in a novel hybrid ambipolar infrared thermocouple, converting a temperature gradient into a voltage signal at the thermocouple junction. We experimentally identify the energy conversion mechanism of the electrostatically controlled device and the key parameters for engineering the MIR (E_{ph} = 0.117eV) photo-response. We measure the photovoltage response of these devices as a function of carrier density (n_s), carrier density difference (Δn_s), substrate material, and temperature, and find that MIR detection is well described within a thermoelectric framework. Of key importance, extrinsic properties of the surrounding environment must be included to fully understand the photovoltage response. We show that these highly sensitive ambipolar graphene infrared thermocouples can perform on par with many other conventional thermoelectric technologies, and that the device response can be improved by choosing substrates that support large temperature gradients.

To locally photo-excite MLG at low photon energies below 0.2eV, we constructed a CO_2 (λ = 10.6μm, E_{ph} = 0.117eV) scanning laser microscope capable of measuring the spatial photo-response of our devices as a function of temperature and gate bias (Figure 6.1(a)). All measurements (optical and electrical) were done using an AC lock-in technique (see Section 6.4).

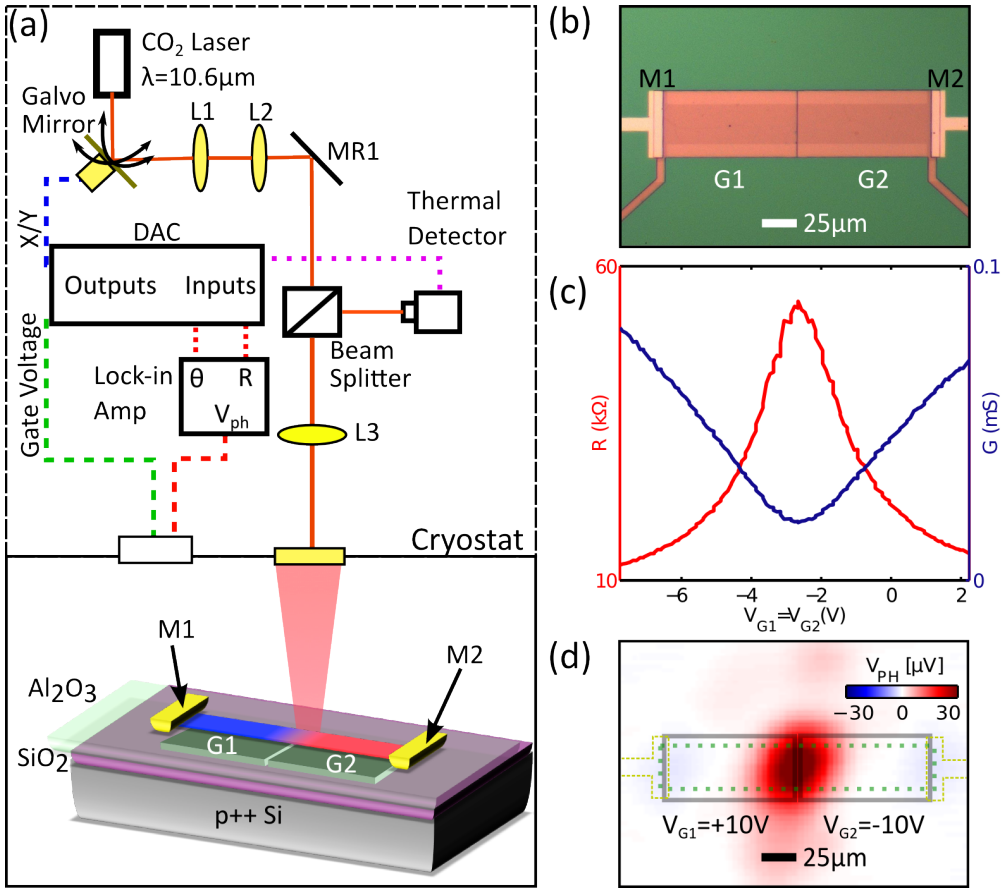

Figure 6.1 Mid-IR Schematic and Measurement

(a) Schematic of the scanning MIR laser microscope. CO_2 laser is scanned across the sample using a galvo-mirror and fed into a cryostat through lens, L1 to L3. A schematic of the ambipolar graphene infrared thermocouple is shown in the lower left hand corner. (b) Optical picture of the fabricated device. M1 and M2 are the ohmic contacts to the MLG; G1 and G2 are the local electrostatic gates. (c) Resistance-Gate Voltage measurements of the device, where $V_{G1} = V_{G2}$, are shown in red. Shown in blue is the conductance versus gate voltage on the right axis. (d) Spatial map of photovoltage response from the device. The MLG is outlined by a dotted green line, while the local electrostatic gates are outlined in grey. The contacts are outlined by a dotted gold line. The gate voltages are biased to form a p-n junction (V_{G1} = +10 V and V_{G2} = -10 V).

Figure 6.1(a) shows the structure of the ambipolar graphene infrared thermocouple, composed of a large area MLG p-n junction device supported on top of

an aluminum oxide (Al_2O_3) infrared absorber. The underlying substrate consisted of 300nm of thermally grown oxide on heavily doped p^+ silicon. Two independent titanium-platinum gate electrodes (V_{G1} and V_{G2}) were then patterned by electron beam-lithography and encapsulated by the deposition of the infrared absorber, which also acts as a gate dielectric (60nm ALD Al_2O_3). The gap between the gate electrodes was designed to be 300-500nm (sub-wavelength across all photon energies used). MLG grown on copper foils, using a chemical vapor deposition (CVD) technique, was then transferred on top using poly(methyl methacrylate) (PMMA) [5]. Atomic force microscopy (AFM) confirmed that the sample was a uniform monolayer while Raman spectroscopy confirmed that there was minimal sample doping due to the high 2D-band ($\omega_{2D} \approx 2680$ cm^{-1}) to G-band ($\omega_G \approx 1580$ cm^{-1}) intensity ratio ($I_{2D}/I_G = 8.5$) and a low concentration of defects by the low D-band to G-band intensity ($I_D/I_G \approx 0$). Finally, electron beam lithography and reactive oxygen etching defined the titanium-gold ohmic contacts (M1 and M2) and the graphene channel respectively (Figure 6.1(b)).

We first characterize the ambipolar graphene infrared thermocouple by measuring the gate voltage dependent resistance (R) and the photovoltage (V_{PH}). We measured R (shown in Figure 6.1(c)) by applying 25μV between M1 and M2 while simultaneously measuring the current. The voltage V_{G1} and V_{G2} were kept equal during the resistance sweep ($V_{G1} = V_{G2}$). The maximum transconductance (g_m) calculated from Figure 6.1(c), allows us to estimate the hole carrier mobility (μ_p) of our MLG to be 800±100 cm^{2}V^{-1}s^{-1}. To form an ambipolar thermocouple in our device, the gates were then biased oppositely ($V_{G1} = 10$V, $V_{G2} = -10$V) to create a p-n junction.

Figure 6.1(d) shows the photovoltage V_{PH} measured between M1 and M2 while the laser is scanned over the device. Due to the diameter of our laser spot ($\approx$20μm), we chose the dimensions of our device (L=200μm, W=30μm) to allow us to spatially resolve the photoresponse. Figure 6.1(d) shows that the photoexcitation in the region near the p-n junction results in a large, positive photovoltage, while the contacts contribute negligible signal.

The photovoltage mechanism can be identified by measuring the response as a function of charge carrier density (n_s) and carrier density difference (Δn_s) at the p-n junction. Figure 6.2(a) shows the dual gate resistance map of our devices. The cross shape in Figure 6.2(a) indicates that the two gates are independent and can electrostatically control each half of the MLG channel. The peak or maximum resistance occurs when both gates are biased at the charge neutrality point (V_D) at approximately V_{G1} = -3V, V_{G2} = -3V, while the resistance of the device decreases as the number of charge carriers increases due to electrostatic doping. Due to the long geometry of our device and small lateral gap between gates, the resistance of the p-n junction itself is negligible compared to the bulk resistance of the MLG channel [81]–[83]. Figure 6.2(b) shows V_{PH} when we fix the laser spot at the p-n junction and sweep over the same gate voltages as in Figure 6.2(a). The four distinct charge carrier configurations in each half of the device are labeled in Figure 6.2(b): p-n, n-n', n-p, p-p'. A distinctive 6-fold pattern of alternating photovoltage polarity is observed due to the sign change when V_{G1} or V_{G2} crosses either a charge neutrality point or the diagonal where $\Delta n_s = 0$ [20], [57].

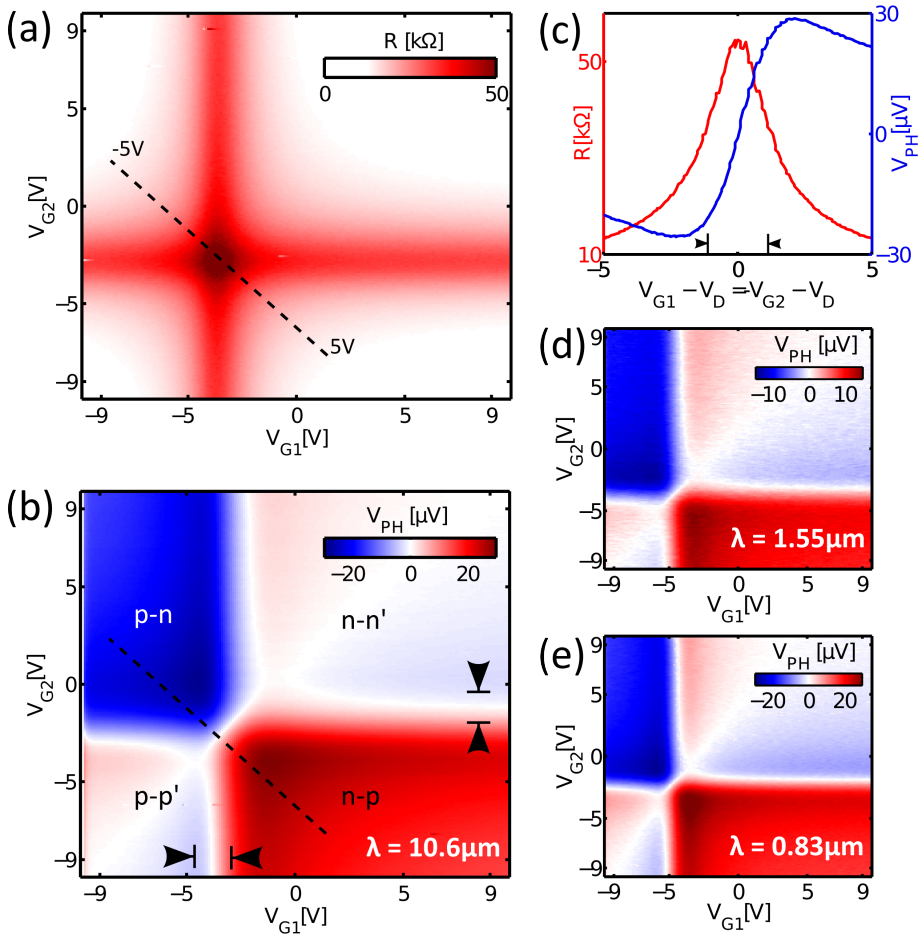

Figure 6.2 Mid-IR Resistance and Photovoltage Gate Maps

(a) Dual gate resistance map of the ambipolar graphene infrared thermocouple. The dashed line indicates the position of the line cut shown in (c) that corresponds to increasing Δn_s (b) Dual gate photovoltage map of the ambipolar graphene infrared thermocouple with λ=10.6μm photoexcitation. The gate voltage range between the arrows is where transitions are not Pauli blocked. The four carrier quadrants are labeled p-n, n-n', p-p', n-p. (c) Line cuts through the resistance and photovoltage maps in the positions indicated by the dashed line in Figure 6.2(a) and (b). (d)&(e) Dual gate photovoltage maps of the ambipolar graphene infrared thermocouple with a λ=1.55 μm and 0.83 μm excitation. Photovoltage at 1.55 μm is smaller due to lower power transmitted to the sample. All measurements taken at 300 K.

We can use the inherent symmetry of the photovoltage gate map to extract line cuts of the data set that contain the most relevant information. While previously in

Figure 6.1(c), we plotted the line cut where $V_{G1} = V_{G2}$, which corresponds to $\Delta n_s=0$, in Figure 6.2(c) we plot the line cut $V_{G1}=-V_{G2}$ cutting through the charge neutrality point in both the resistance map and the photovoltage map. This line cut corresponds to fixing the junction's carrier density at the charge neutrality point, while the MLG to the left and the right is doped so that Δn_s varies from negative to positive. As mentioned before, the resistance line cut (shown in red in Figure 6.2(c)) looks quite similar to our previous line cut in Figure 6.1(c) thus confirming that the p-n junction is a small contribution to the resistance of our devices. Furthermore, the line cut (shown in blue in Figure 6.2(c)) through the photovoltage map shows a roll off at large Δn_s and a positive and negative maximum located near the charge neutrality point. Also in Figure 6.2(c), under MIR photoexcitation of the p-n junction, we observe *no* noticeable transition between Pauli allowed (high absorption $E_f < ½E_{ph}$) and Pauli blocked (suppressed absorption $E_f > ½E_{ph}$) regime. The threshold gate voltages where Pauli-allowed transitions can occur at 10.6μm (0.117eV) are indicated in Figure 6.2(b)&(c). While these experiments were done to probe very low photon energies, we also took the same device and repeated the experiments (photovoltage maps) at λ = 1.55μm (E_{ph}=0.8 eV) and at λ = 0.83μm (E_{ph}=1.49 eV) shown in Figure 6.2(d) and (e) respectively. The data sets at both higher photon energies also show the distinctive 6 fold pattern that indicates a thermoelectric mechanism. Comparative line cuts through the wavelength dependent photovoltage are provided as supplementary information (Figure 6.6).

In the ambipolar graphene infrared thermocouple, the incident radiation is absorbed near the p-n junction and increases the local temperature (T_{hot}) relative to the contacts (T_{cold}). The thermal gradient is established across both the MLG and within the infrared absorber. Photons are absorbed optically and are converted into a thermal bath composed of both phonons and electrons. The thermal gradient ($\Delta T = T_{hot} - T_{cold}$) between the p-n junction and the contacts results in holes and electrons near the Fermi energy level diffusing away from the junction, thereby establishing a photo-induced voltage via the thermoelectric effect (Figure 6.3(a)) [84]. The difference between MLG's Seebeck coefficients (S_1 and S_2) on each side of the junction results in the six fold symmetry observed in previous work [20], [69]. The gate dependence of the photovoltage signal can be written as:

$$V_{PH}[V_{G1},V_{G2}] = [S_1(V_{G1}) - S_2(V_{G2})]\Delta T \tag{6.1}$$

The gate tunable Seebeck Coefficient ($S(V_G)$) of MLG follows from Mott's relation [84], [85], and exhibits a sign change as V_{Gi} crosses the charge neutrality point (embedded in the term dR/dV_G):

$$S_i(V_{Gi}) = \frac{\pi^2}{3}\frac{k_B^2 T}{q}\frac{1}{R}\frac{dR_i}{dV_{Gi}}\frac{dV_{Gi}}{dE}\bigg|_{E_f} \tag{6.2}$$

Here, k_B is the Boltzmann constant, T is the temperature, q is electron charge, E_f is Fermi energy and V_{Gi} (i=1,2) is the bias on the left and right gate embedded in the infrared absorber. The magnitude of the Seebeck coefficient can be increased by decreasing the disorder near the charge neutrality point, leading to a larger derivative

term. Optical absorption deposits power in the device and creates a thermal gradient, which we can write as:

$$\Delta T = \frac{1}{\kappa_{eff}} P_{in}[1 - \exp(-\alpha t)] \tag{6.3}$$

Here P_{in} is the incident laser power, κ_{eff} is the effective thermal conductance between the p-n junction and the contacts, taking into account the parallel thermal paths, t is the thickness of material at the device junction, and α is the optical absorption of the material. As evidenced by the absence of Pauli blocking, optical absorption through the formation of electron-hole pairs is not the dominant mechanism for establishing a temperature gradient ΔT.

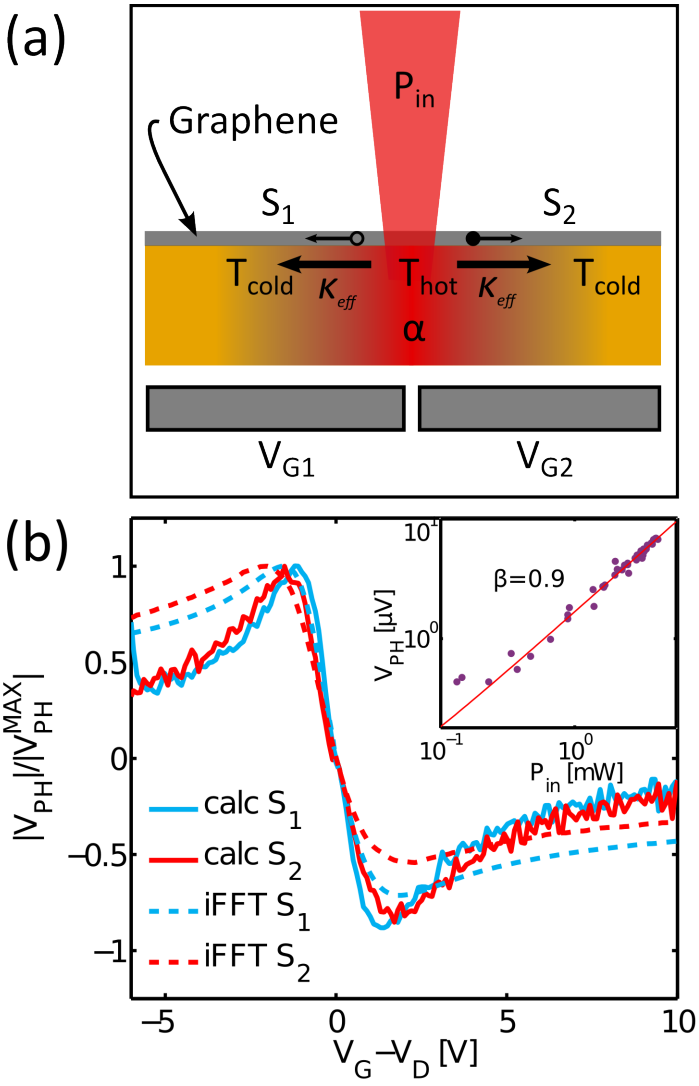

Figure 6.3 Model Schematic and Fourier Analysis of Seebeck Coefficient

(a) Schematic of our thermoelectric device. Hot carriers at the junction (solid circle represents electrons, empty circle represents holes) diffuse away from the local heat spot generated by the laser. The temperature difference between the junction temperature (T_{hot}) and the ambient temperature (T_{cold}) is controlled by the optical absorption (α) and thermal conductance (κ_{eff}) of the substrate. (b) Seebeck coefficients calculated from the resistance map in Figure 6.2(a) using Mott's relation (solid lines) and independently extracted from the photo-voltage map in Figure 6.2(b) using a Fourier transformation analysis technique (dashed lines). The inset shows the photo-voltage as a function of incident optical power (P_{in}) at λ=10.6 μm. The fit line is $\log(V_{PH})=\beta\log(P_{in})+c$ with a coefficient (β) of 0.9.

We note that the length of our devices (L=200μm) is much longer than the estimated electronic cooling length (≈2μm), allowing us to neglect hot-carrier mechanisms that have been reported previously [20]. Based on this physical understanding, we can make several predictions to validate our model and engineer improved sensitivity.

We first compute the expected gate-dependent Seebeck coefficient (S_1 and S_2) purely from the resistance map using equation (6.2). Independently, we also extract the two Seebeck coefficients from our photo-voltage map using a Fourier transform (FT) of equation (6.1) with respect to V_{G1} and V_{G2} [20]. This is possible since the two Seebeck coefficients in equation (6.1) are assumed to be linearly independent with respect to gate bias (V_{G1} and V_{G2}). Filtering the data along the x and y axis in Fourier space and then inverting the FT, we can find the experimentally measured Seebeck coefficients from Figure 6.2(b) (shown in Figure 6.3(b) as dotted lines). The agreement between extracted and calculated coefficients further supports our thermoelectric model since these coefficients are responsible for the multiple sign reversals (6 fold pattern) observed in our map, as opposed to single sign reversal expected from photovoltaic effects [61]. Furthermore, the inset of Figure 6.3(b) shows the photovoltage response as a function of incident power (P_{in}). The linear power dependence that we observe (β=0.9) is consistent with Fourier's law (equation (6.3)) in this range of optical powers.

Given its thickness, MLG is an excellent thermal conductor as well as a broad band absorber [86]–[88]; however, the infrared absorber material has an absolute bulk

thermal conductance and optical absorption that can be equally as important, depending on the geometries involved. Within our model, the thermal conductance (κ_{eff}) and the optical absorption (α) are central to the photo-response mechanism of our devices. However, two questions naturally arise: (1) does the laser primarily heat up the MLG (optical free carrier absorption) or the infrared absorber around the MLG (substrate optical absorption, etc.) and (2) what thermal conductance dominates our device (the MLG's or the infrared absorber's thermal conductance)?

Our model predicts that increasing the optical absorption in our devices should lead to an increased photovoltage signal. To test this, we fabricated identical devices as previously shown in Figure 6.1(b); however, we replaced the Al_2O_3 infrared absorber with SiN, which has a larger optical absorption (α =1.3μm^{-1}) than Al_2O_3 (α =0.34μm^{-1}) at λ=10.6μm [89]. Figure 6.4(a) shows the transport behavior (V_{G1}=-V_{G2}) of the SiN devices compared to the previously discussed Al_2O_3 devices, taken at temperatures ranging from 100K to 300K. The resistance curves of both devices exhibit weak temperature dependence and the calculated Seebeck coefficients (equation (6.2)) are similar in magnitude for both devices (Figure 6.4(b)).

In contrast, the measured photovoltage signal is twice as large at room temperature for the ambipolar graphene infrared thermocouple supported on SiN (with larger MIR absorption), compared to Al_2O_3 (Figure 6.4(c)), even though the transport behavior is highly similar in both devices. From this, we conclude that the optical absorption mainly occurs in the infrared absorber ($\alpha \approx \alpha_{SUB}$).

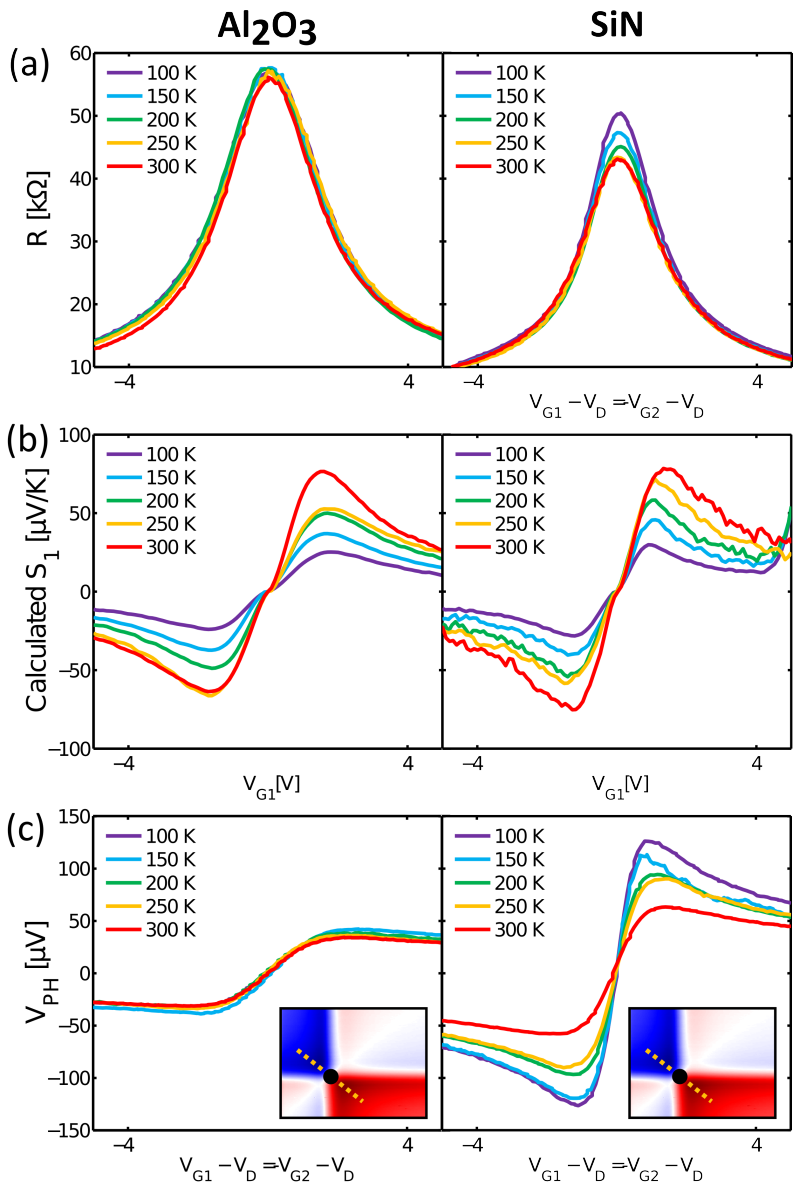

Figure 6.4 Substrate Comparison and Response

(a) Resistance-Gate Voltage measurements of the ambipolar graphene infrared thermocouple utilizing different infrared absorbers (ALD Al_2O_3 on the left and PECVD SiN on the right) at various temperatures (100K – 300K) (b) The Seebeck coefficients computed from the transport data in Figure 6.4(a); for simplicity we plot the dependence on one gate only due to the symmetric behavior of the resistance maps. (c) The measured photo-voltage response as a function of temperature for each infrared absorber. The inset shows schematically where the line cuts were taken in the complete dual gate response at 300K.

As heat is deposited and diffuses away, the magnitude of the temperature gradient (equation (6.3)) will be determined primarily by the highest thermal conductance. To study this effect we measure the temperature dependence of both devices, and find distinct trends for each infrared absorber material. Our model (equations (6.1)-(6.3)) states that the temperature dependence follows $V_{PH} \propto T/\kappa(T)$, where $\kappa(T)$ is the temperature dependent thermal conductance and α is temperature independent (no thermo-optic effect). In Figure 6.5, we plot the normalized maximum photovoltage (V_{PH}^{MAX}) and the quantity $\langle \kappa_{eff} \rangle \propto T/V_{PH}^{MAX}$ (normalized effective conductance) as a function of temperature for both Al_2O_3 and SiN. As a function of temperature, the photovoltage increases with decreasing temperature, but at a much larger rate for devices with a SiN infrared absorber. Within that temperature range, the quantity $\langle \kappa_{eff} \rangle$ exhibits a decreasing trend with distinct slopes for Al_2O_3 vs. SiN, regardless of the illumination wavelength. Fitting this data to a power law $\langle \kappa_{eff} \rangle \propto T^{\gamma}$, we find that $\gamma \approx 1$ for Al_2O_3 ($T^{1.14}$ at 0.83μm and $T^{0.99}$ at 10.6μm) and $\gamma \approx 1.5$ for SiN ($T^{1.41}$ at 0.83μm and $T^{1.55}$ at 10.6μm). These values show excellent agreement with thermal conductivity measurements for amorphous dielectric solids in the regime where strong phonon scattering limits thermal conductance [90], [91].

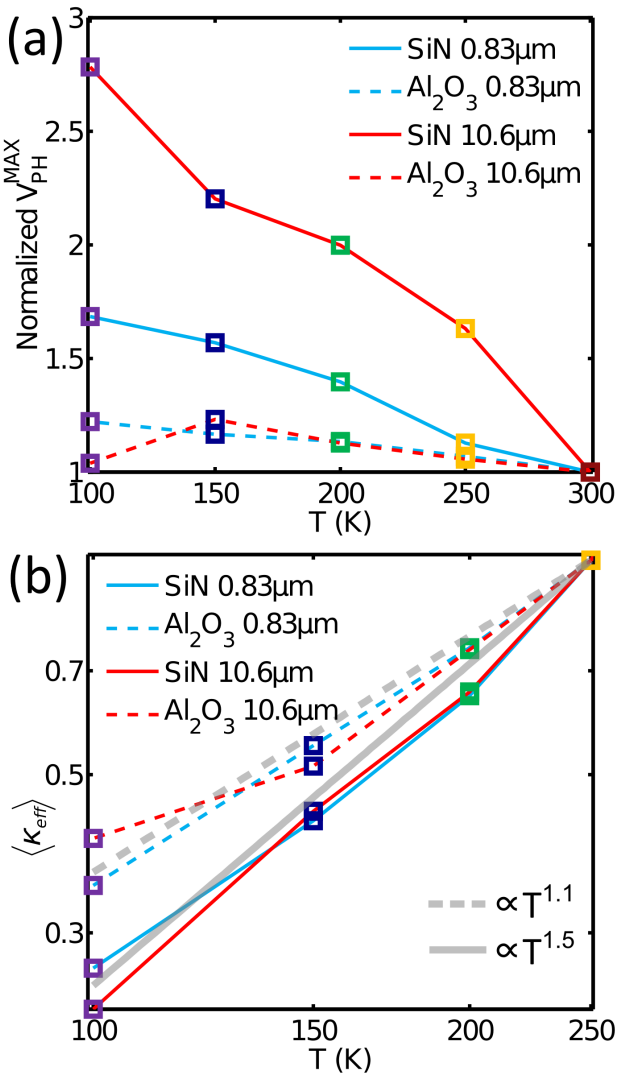

Figure 6.5 Temperature Dependence of Response

(a) The maximum V_{PH} normalized with respect to the maximum V_{PH} taken at 300 K as a function of temperature. The solid lines represent measurements taken for SiN while the dotted lines represent the data for Al_2O_3. The color indicates the excitation source for the measurements (red is λ=10.6 μm, while blue is λ=0.83 μm). (b) Temperature dependence of the normalized effective thermal conductance $\langle \kappa_{eff} \rangle$ for both SiN and Al_2O_3 substrates plotted on a log-log scale. The grey lines show the power law (T^{γ}) fitting to the data. γ is 1.1 and 1.5 for SiN and Al_2O_3 respectively.

6.3 Summary and Future Directions

By integrating electrostatically controlled MLG with carefully chosen infrared absorbers, we construct a highly sensitive ambipolar graphene infrared thermocouple. The device sensitivity can be engineered by choosing substrate materials with a high MIR absorption and low thermal conductance. A thermoelectric description captures important aspects of the device response for a wide variety of conditions: temperatures (100-300K), photon energies (0.117-1.49eV), and substrate materials. While MLG can exhibit a Seebeck coefficient (± 50μV/K) similar to a variety of other standard thermoelectric detectors such as poly Si, Sb, and Bi [66], MLG embedded into a hybrid thermal device has one major advantage: an atomic layer of graphene adds a negligible thermal mass, yet generates significant MIR photovoltage signal. This work provides a significant step towards engineering MLG devices that extract energy from thermal gradients, a technology that may have applications in human positioning detectors, passive sensors such as nanoscale monitors of chemical reactions, as well as transparent and flexible thermal sensors and energy harvesting device.

Experimental Details and Supplementary Information

6.4 Infrared Scanning Microscope

The light source was a temperature stabilized 1W CO_2 laser (Access Laser Company) providing a collimated light source at a wavelength (λ) of 10.6 μm. After mechanical chopping, the laser power on the sample was typically ≈8mW as

determined by a reference thermal power meter (Thorlabs). A beam combiner optic (ULO optics) was used to add a collinear 632 nm diode laser for alignment (not shown in Figure 6.1(a). A set of galvanometer controlled mirrors produces angular deflections centered at the focal point of lens 1 (L1 in Figure 6.1(a)). These deflections were then mapped through a relay of confocal optics (L1 and L2) onto the back focal plane of the objective. The confocal optics direct the beam to strike the objective at the same position, but at a variable angle set by the galvanometer mirrors, producing distortion free scanning over a large (>1mm^2) area. The beam was then passed through a ZnSe anti-reflection coated window into an optical cryostat (Janis) allowing measurements to be done under vacuum and at low temperatures (77K< T<300K). To reduce noise in our measurements, the laser is modulated with an optical chopper wheel operating at 368Hz before it is sent to the galvo mirrors. A lock-in amplifier operating in differential voltage mode is connected across the two contacts of the device (M1 and M2) and synced to the output reference from the chopper wheel. The surface reflectance image of the chip was simultaneously recorded as a function of laser position by the reference thermal detector. The metallic bond pads provide high contrast features on the chip to orient our device and to align our laser spot to the junction signal. The reflected signal also provides feedback on the stability of the laser power and alignment during scanning. Laser power attenuation was achieved by utilizing a Brewster window attenuator (ULO optics) and by feeding the input beam through a series of cross polarizers. We also measured the response of the device

purely as a function of laser polarization and saw no change in the signal, ensuring that we measured the effect of only the power dependence using the attenuator.

6.5 Visible Scanning Photovoltage System

The visible scanning photo-voltage system was identical to the one reported in [20]. The laser source used in our experiment, however, was a near infrared laser diode (λ= 0.83 μm) from Thorlabs, while the 1.55 μm laser source was a standard telecom laser source from Agilent fed through an eribium doped fiber amplifier (EDFA) from Broadcom. Both lasers were free space coupled to the scanning piezo mirror. The power density and overall power of the laser at 1.55 μm is lower than at 0.83 μm. The spot diameter for the 0.83 μm laser was $\approx$2 μm ($\approx$5 mW total power) and the spot size for the 1.55 μm is $\approx$4-5 μm ($\approx$1.2 mW total power). The lower power density of the 1.55 μm laser source is mainly due to the less efficient transmission through the optics.

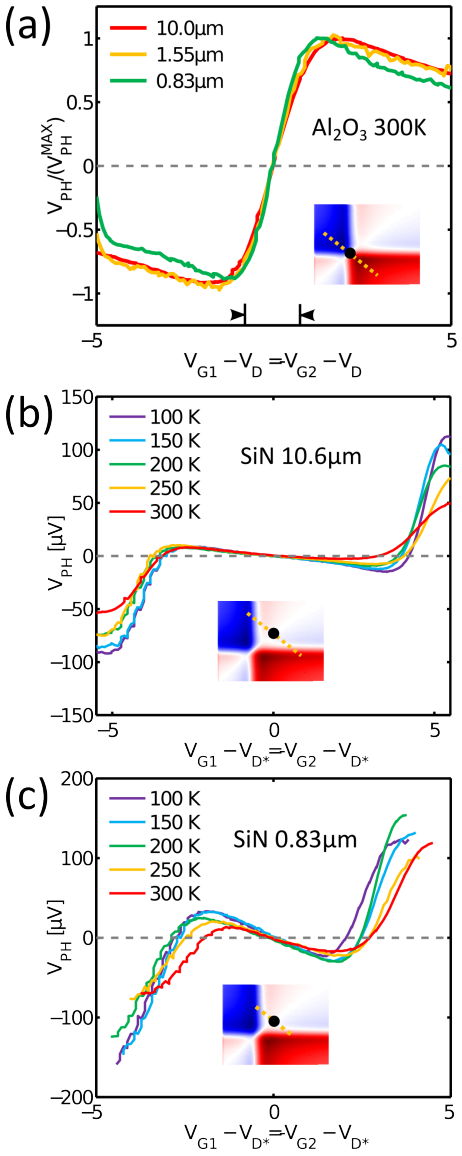

Figure 6.6 Temperature and Wavelength Dependent line cuts through Photovoltage Maps.

(a) Line cut through the charge neutrality point with varying laser excitation (λ=10.6 μm, 1.55 μm, 0.83 μm) represented by red, orange, and green respectively. Pauli allowed transitions for λ=10.6 μm are denoted by tick marks (b) and (c) Line Cuts parallel to the line cut of changing carrier density gradient in the photovoltage map at λ=10.6 μm and 0.830 μm respectively. The junction is now offset away from the charge neutrality point while increasing the Fermi Energy gradient between both sides. The 3 sign changes in the line cuts indicate that the same 6 fold pattern is present at all temperatures and at both wavelengths.

6.6 Device Fabrication

Our devices were fabricated on a Si/SiO_2 substrate (thermally grown oxide 300 nm on p-type silicon – SQI). The split metallic gates (300-500nm gate separation) were composed of 5 nm of Ti and 35 nm of Pt using e-beam lithography (Elionix 125 keV). 60 nm of Al_2O_3 was deposited by atomic layer deposition (ALD) in a Cambridge Nanotech tool. The PECVD SiN was deposited at 300°C using a Surface Technology Systems (STS) deposition tool. MLG grown by chemical vapor deposition (CVD) on metallic copper foils was then transferred to the chips using a PMMA support film, producing conformal MLG over the surface of the sample [5]. The PMMA was removed by dipping in acetone overnight. Ohmic contacts (1 nm Ti/ 30 nm Au) were patterned using e-beam lithography and metal evaporation. The graphene was etched to electrically isolate devices, using PMMA as an etch mask and a reactive oxygen ion etcher from Plasmatherm. The final devices were then wire bonded with Al wire into the ceramic chip carriers (Spectrum) and aligned to the scanning area.

6.7 Half-Gated Devices

In addition to the devices with two split gates as shown in Figure 6.1, we fabricated devices with only one of the of the metallic gates present. The other half of the graphene channel was controlled instead by the Si backgate. In all other respects, this device was identical to the other devices that we measured. The purpose of this device was to test if the metallic gates reflected a significant amount of the radiation

and if allowing a deeper penetration into the SiO_2 would increase the absorption and thus the temperature gradient and signal from the device. The skin depth of Pt metal at 10μm wavelength is approximately 30nm, which is smaller than the thickness of our gate, indicating that most of the radiation should be reflected from the gate. Also, the gap between the gates is significantly smaller than the wavelength, indicating that there should not be appreciably larger absorption at the junction, i.e. the gates should appear to be a continuous, conductive sheet for our laser. We also checked the polarization dependence of our device to ensure that the gates were not acting as an antenna. Under all polarizations, the response of the device appeared identical in our gate sweep maps.

Some initial measurements of this type of device showed an anomalous response where the signal would undergo several shifts spatially as the gate voltage was varied. Movies created of the photovoltage maps as a function of gate voltage showed this behavior clearly. However, closer inspection of these devices revealed a small delamination of the metal gate at its perimeter. Ultimately, this was traced to etching of the Ti adhesion layer at the edges of the metal stack and subsequent ALD deposition peeling up the Pt metal. This created a raised lip at the edge of the gate and led us to conclude that the graphene was being suspended at the junction for some short distance.

Once this problem was solved the devices behaved as expected and standard gate sweep maps were obtained in Figure 6.7. The maximum response of the half gated devices was slightly lower than for the split gate geometry, indicating that the

absorption in the SiO_2 was small compared to the absorption directly beneath the graphene and that the dielectric layer had a dominant effect on the device characteristics.

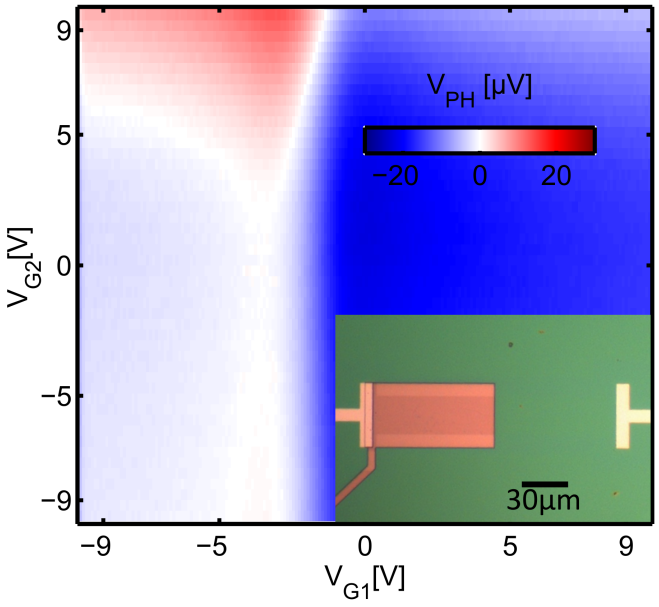

Figure 6.7 Mid-IR Half Gated Device
Slightly smaller response (~22μV) is found when one of the gates is removed so that half of the graphene is controlled by the global backgate. Vertical axis is stretched compared to other gate sweep maps since the capacitive coupling through the 300nm oxide is lower. Inset shows optical image of the device.

Chapter 7

7. Applications of a Graphene Thermocouple

7.1 Introduction

After determining the physical mechanism that underlay the response of our devices and the material properties that were most advantageous to increasing the sensitivity of these graphene detectors, we sought to demonstrate our work as a technology with potential applications. To this end, we pursued different subprojects, each of which expanded the capability of our sensor in different ways. One of the most obvious ways of improving the sensitivity of our device was to eliminate the bulk Si material directly underneath the p-n junction. This material acted as a very efficient heat sink and in our modeling the diffusion of heat vertically through our structure was a major limitation on the thermal gradient that was possible given the input power and device dimensions. Removal of the Si would leave the SiN dielectric layer suspended with the associated gate structure embedded within it and the graphene lying across it. Suspension, although problematic, was made easier in this case because of the high

tensile strength of the SiN material and the fact that a thicker layer (~2-3μm) of SiN was actually advantageous since it also acted as an infrared absorber. In addition, the use of thermopile geometries, where multiple junctions in series produced signal, promised in increase the sensitivity of our devices.

In parallel with this direction, we pursued a project to take full advantage of graphene's transparent and flexible qualities as well as its scalability [92]. The concept was to create a thermal sensor that could be deposited on a clear plastic substrate material, in an application where other thermocouple materials would be opaque and mechanically rigid or prone to failure [93]. Integration into large-scale products would provide an opportunity to utilize integration of an active electronic element and the scale of reel-to-reel processing.

Finally, we sought to produce a focal plane array of graphene detectors with an integrated set of lock-in circuits fabricated on a CMOS chip (TSMC).

7.2 Suspended Graphene Thermocouples

There are several trade-offs when attempting to increase the detection sensitivity of our graphene devices. In attempting to suspend our devices we were effectively trading sensitivity for response time. In our original devices, the larger thermal heat sink of the underlying Si decreased the response time of our devices (made them faster) due to the faster thermal equilibration time, however, the maximum temperature gradient produced was smaller. By suspending our devices we increased the time that it would take for thermal equilibration (i.e. the time that it

would take to register a new IR intensity) but increased the signal that we would receive from that IR intensity (increasing the thermal gradient produced in steady state). We estimated that our original devices on Si had a time constant on the order of microseconds, we were unable to measure this directly since we did not have a method of modulating the laser beam at MHz frequencies, but we observed no significant difference between measuring at 1kHz (direct modulation of the laser via gating voltage) and 368Hz (modulating with the optical chopper wheel).

The most obvious time scale for imaging applications is close to video frame rates of 30-60Hz so there was significant room for improvement of the response of our devices. For the first set of devices that we designed, the geometry was effectively unchanged, with two metallic gates controlling each half of a graphene channel. However, instead of standard SiO_2/Si substrate materials we used a bare Si substrate and deposited a SiO_2/SiN layer, patterned metal gates, and deposited a SiO_2 dielectric layer. All dielectric materials were deposited using a PECVD tool as described in chapter 6. Graphene transfer, patterning and contacting were performed as before, with an additional final step of Si etching. The SiO_2 is necessary to prevent thinning of the SiN during the Si etching process, since it has a better etch selectivity than SiN. The etching process or "release" of the structure was a dry process, using XeF_2 gas chemistry to selectively etch the Si and avoiding the capillary forces that often collapse MEMs structures [94]. Windows patterned in the SiO_2/SiN/SiO_2 allow the gas to access the underlying Si and etch around and beneath the structure (Figure 7.1).

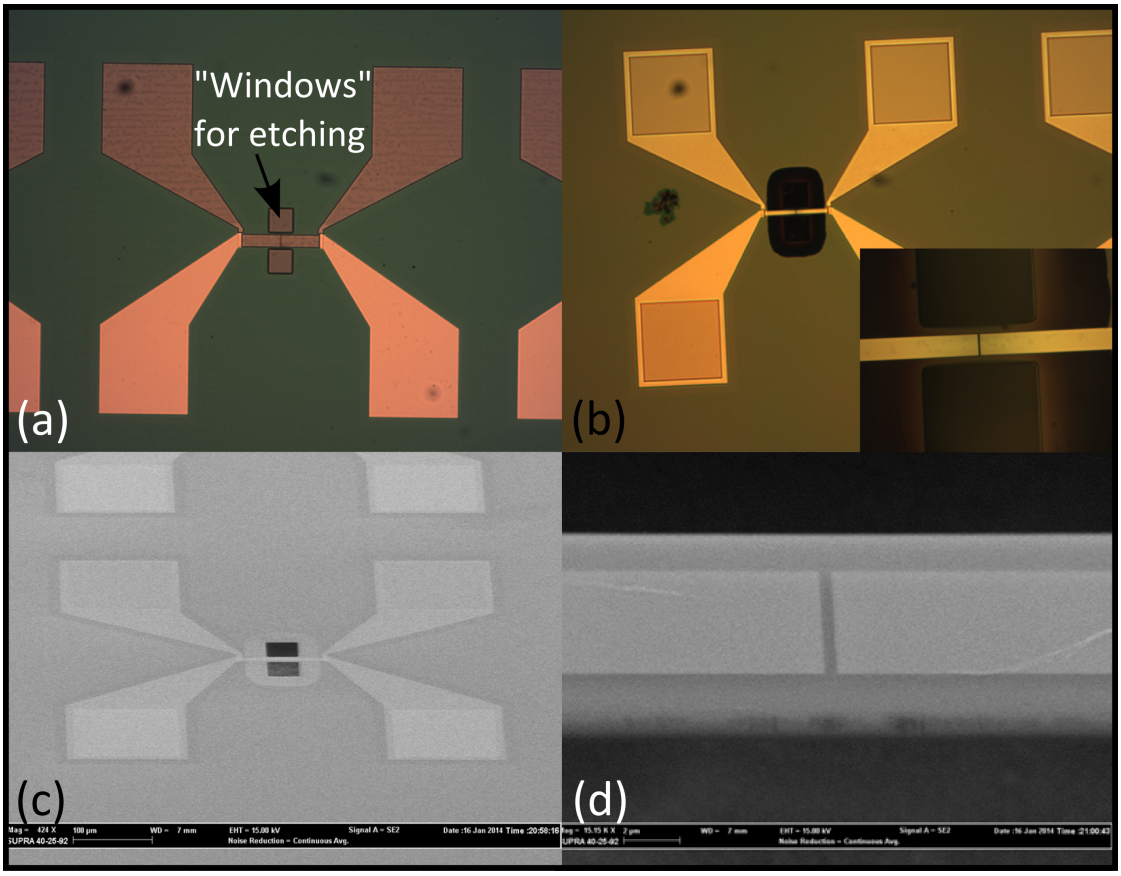

Figure 7.1 Suspended Device Before and After Release

(a) Completed device before XeF_2 release with metal gates, contacts, and windows on either side of the device for gas to access the Si substrate. (b) Device after etching with holes where the windows allowed etching, inset shows a close-up of the bridge formed over the etch cavity. (c) SEM of the device with the windows, gate structure and etch cavity visible. (d) SEM close-up of the bridge structure.

7.3 Improved Sensitivity

Several different versions of the suspended devices were fabricated with different dimensions in an attempt to determine the optimum profile and aspect ratio for etching and suspension. After suspension of the graphene channel on the SiN bridge structure, we attempted to bond the resulting devices and measure their response. We found that most or all of the devices with a long aspect ratio (a

suspended length of ~90μm) had breaks either in the graphene channel (failed open) or the metal gates that controlled the channel making it impossible to create a p-n junction. The shorter devices were much more likely to be functional. These failures were almost certainly due to the stress in the SiN film cracking the graphene or gate during the suspension process. Additionally, these devices were substantially more sensitive to electrostatic discharge for the same reason. However, several good devices were identified and tested. Spatial photovoltage maps showed a strong response at the center of the device when applied gate voltages formed the p-n junction. Focusing the laser on this spot at the center of the junction and measuring the response shown in Figure 7.2(b) we found a peak response of ~1.5mV, for a laser power of 1.5mW.

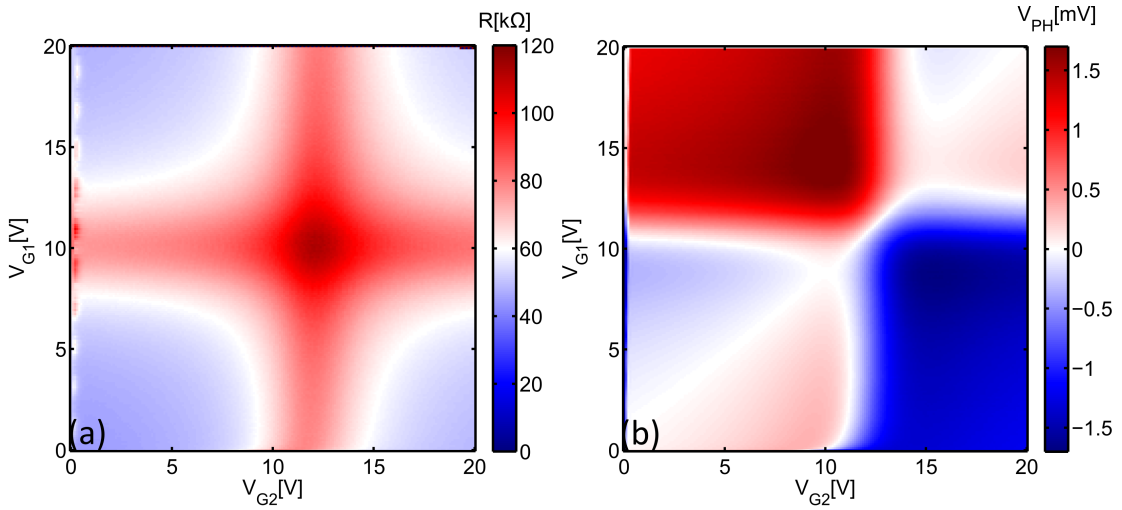

Figure 7.2 Gate Maps of the Suspended Device Resistance and Photovoltage
(a) The device resistance as a function of both gate voltages, using a high voltage amplifier to expand the range of the standard -10V to 10V DAC output. (b) The photovoltage response of the device with the laser focused at the center of the junction, sweeping over the same gate voltages. The laser power was measured at the objective to be 1.5mW.

The laser power was measured after the final objective, using a pyrometer (Thorlabs) with the chopper wheel off (i.e. steady state power output). This translates into a roughly ~1V/W sensitivity. To measure the thermal time constant of the device we varied the frequency of the chopper wheel and measured the magnitude of the photovoltage with the junction biased to create the maximum p-n junction on the photovoltage map. Based on a rough approximation of the detector response as the solution to a first order differential equation, we can write:

$$V_{PH}(\omega) = \frac{V_0}{\sqrt{1+(\omega\tau)^2}} \tag{7.1}$$

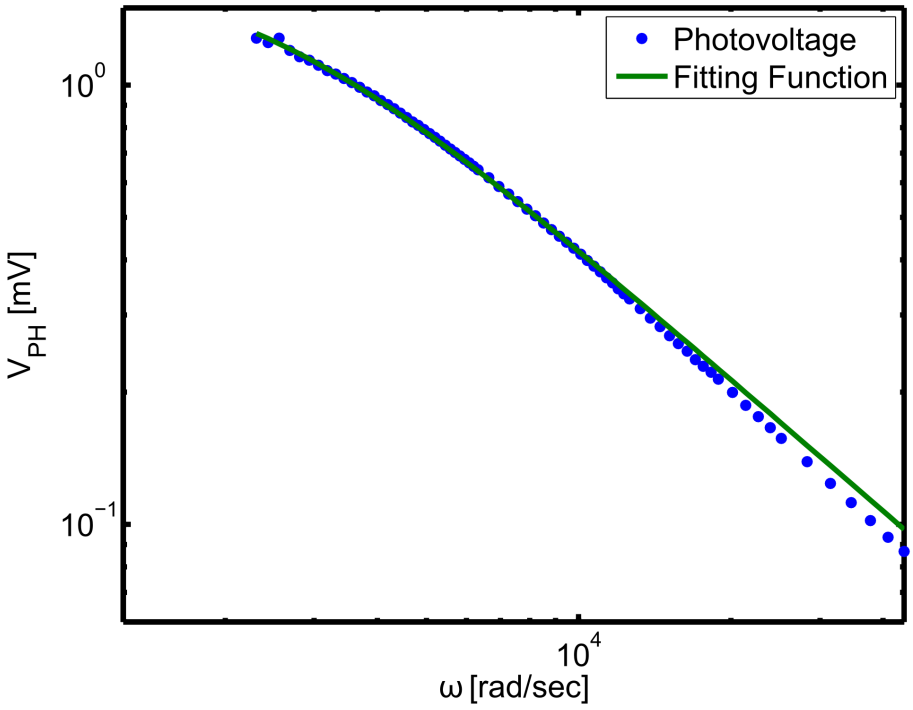

Figure 7.3 Frequency Response and Fitted Thermal Bandwidth
For the suspended devices shown in Figure 7.1 and Figure 7.2 the thermal time constant can be extracted by fitting the photovoltage response as a function of optical modulation frequency (ω). Here we fit a thermal time constant of τ=0.43ms

The sensitivity of our device can also be improved by creating a lateral thermopile, where multiple graphene p-n junctions are arranged in series. Each section of the device has a hot and a cold end and in a series arrangement, should add signal together. We also incorporated an infrared absorber "pad" suspended in the middle of the device to increase temperature experienced by the hot end of each thermocouple in the device. Fabrication of these devices was more difficult due to the more complex geometry allowing the stress of the SiN film to crack the device at the corners and connection points in the suspended part of the film. By making the connection to each section of the thermocouple external via wirebonds, it was possible to measure the response of one junction, and the response of two junctions in series, while avoiding the portions of the device that were damaged due to cracking (Figure 7.4).

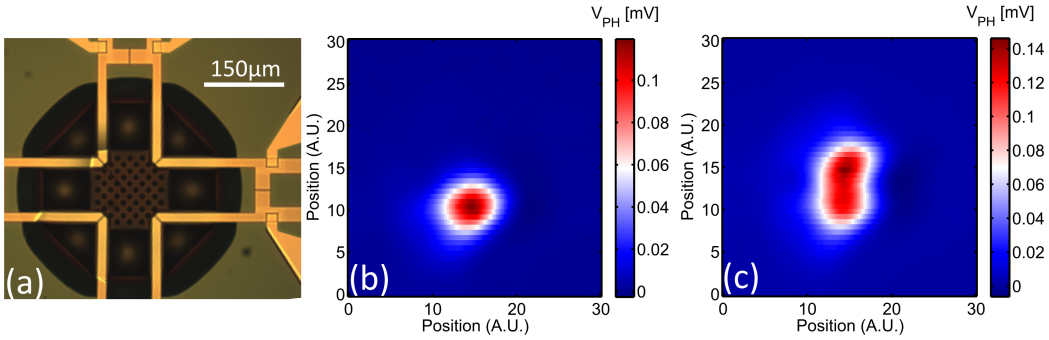

Figure 7.4 Thermopile device with Two Junctions
(a) Optical image of the device, the left two junctions are broken due to stress fractures, but the right two are functional (b) Spatial photovoltage map with one junction connected (c) Spatial photovoltage map with both junctions connected in series.

With the two junctions wired in series, there is a substantially higher resistance through the device and the thermoelectric pattern is not as clear in the gate sweep

maps. However, the device can be controlled and the response is larger for the two junctions. We can also measure the response as a function of frequency and find that the thermal time constant is substantially longer as shown in Figure 7.5 (calculated from equation 7.1), indicating that the device would be better operated at something approaching video frame rates (30-60Hz) where it has ~6 V/W sensitivity.

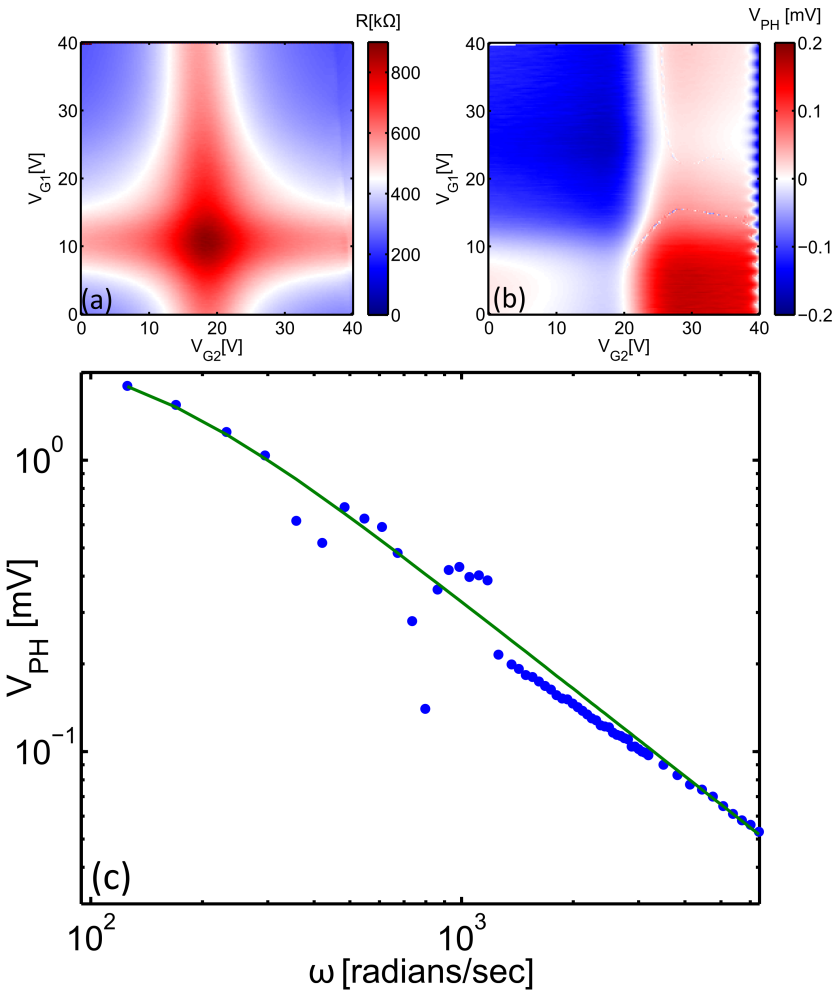

Figure 7.5 Gate Voltage and Frequency Response of Thermopile Device
(a) Resistance and (b) photovoltage of the device as a function of gate voltage, measured at 368Hz modulation and 280μW laser power (c) Magnitude of the photovoltage as function of frequency, showing a time constant of ~7.5ms.

7.4 Transparent and Flexible Graphene Thermocouples

Our original concept was to produce a large-scale version of our graphene thermocouple, replacing the rigid, ceramic materials with plastic and spin-on polymers, and the metallic gate material with a highly doped graphene layer, etched into the appropriate shape. Several challenges presented themselves. First, in the vertical gate structure, two graphene layers must be separated with a dielectric material of uniform thickness over a large area. Any defects in the dielectric layer can lead to a short between the two layers, rendering the device useless. Additionally, the plastics had to withstand the temperatures and chemicals involved in the processing and transfer of the graphene. Finding a spin-on, acetone resistant plastic was one of the most challenging problems. We attempted to use PECVD SiN initially, as well as ALD Al_2O_3, however both of these materials ended up flaking off of the surface. Encapsulating a layer of PMMA with Al_2O_3 was also unsuccessful since acetone would penetrate at cracks and dissolve the PMMA. We eventually settled on a UV cured SU-8 material, diluted to spin to a thickness of 1μm and treated with an O_2 plasma to enhance the graphene adhesion. To provide a simple test of the process, we deposited a metallic gate on a borosilicate glass substrate, then spun-on the SU-8 dielectric and transferred the graphene and etched it into strips. As shown in FIGURE REF, it was possible to gate the graphene strip and to measure the photoresponse of the ribbon at each edge of the gate.

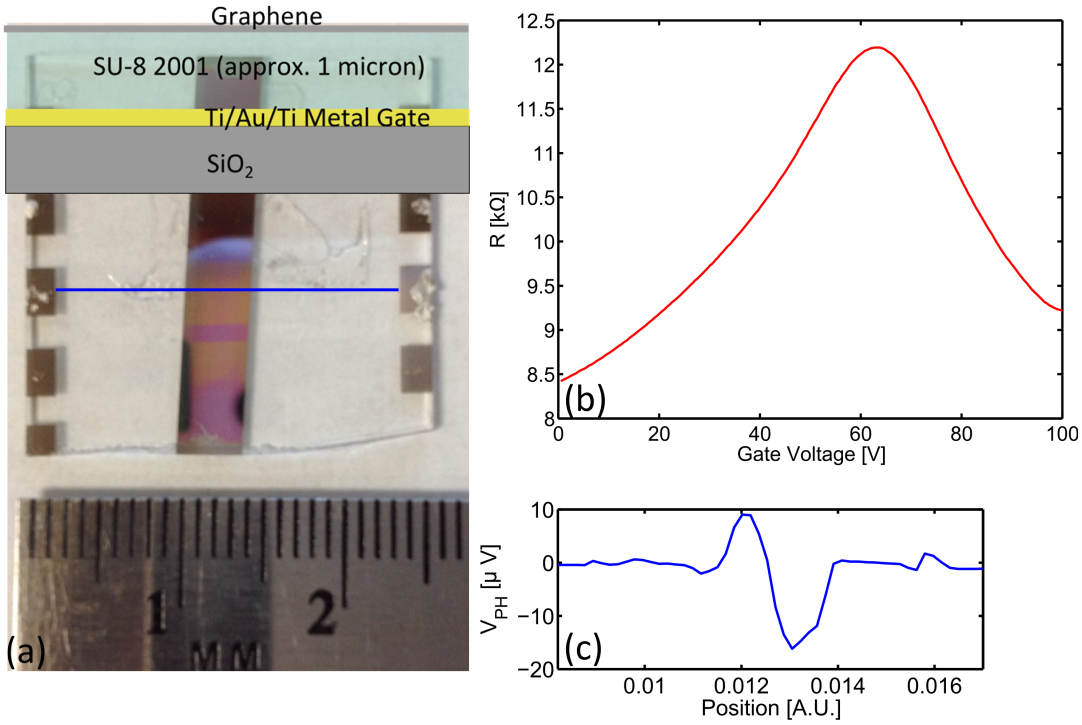

Figure 7.6 Metal-SU8-Graphene Sensor
(a) Image and cross section schematic of the sensor, blue line indicates where the position trace was taken (b) The resistance of the sensor as voltage is applied to the metallic gate shows clear modulation and (c) by tracing the laser spot over the sensor a response is seen at each edge of the metal gate.

In conjunction with this we tried fabricating devices that utilized contact doping from a few nanometer (2-8nm) thick layer of Al to produce a junction in the graphene. This approach has the advantage that since no voltages are necessary to produce the junction, the junction is always on, and no dielectric layer is necessary. For an appropriate thickness of the aluminum layer (~5nm), oxidation is nearly complete and the device remains transparent. Response from these devices was found to be on the order of 100μV after heating the junction with a hot air gun for ~1-2

seconds. We are in the process of developing more quantitative evaluations of the response of this kind of device.

7.5 Conclusion

After fabricating suspended devices we have found that there is a significantly improved response (on the order of 100 times larger) for these devices as compared to the on-substrate devices characterized in chapter 6. Additionally, creating thermopile geometry substantially improves the magnitude of the sensitivity, at the cost of increasing the thermal response time; a trade-off that might be exploited to create effective imaging arrays for thermal viewing applications. We have also been able to create large area graphene devices that are sensitive to temperature gradients between a junction in the middle and contacts at the edges. These transparent, and potentially flexible graphene sensors could provide an application of graphene as an active electronic element beyond the current near term prospects of its use as a transparent electrode material.

Bibliography

[1] S. J. Blanksby and G. B. Ellison, “Bond Dissociation Energies of Organic Molecules,” *Acc. Chem. Res.*, vol. 36, no. 4, pp. 255–263, Apr. 2003.

[2] M. S. Dresselhaus, G. Dresselhaus, P. C. Eklund, and A. M. Rao, “Carbon Nanotubes,” in *The Physics of Fullerene-Based and Fullerene-Related Materials*, W. Andreoni, Ed. Springer Netherlands, 2000, pp. 331–379.

[3] J. Kong, H. T. Soh, A. M. Cassell, C. F. Quate, and H. Dai, “Synthesis of individual single-walled carbon nanotubes on patterned silicon wafers,” *Nature*, vol. 395, no. 6705, pp. 878–881, Oct. 1998.

[4] Y. Horikoshi, M. Kawashima, and H. Yamaguchi, “Low-Temperature Growth of GaAs and AlAs-GaAs Quantum-Well Layers by Modified Molecular Beam Epitaxy,” *Japanese Journal of Applied Physics*, vol. 25, no. Part 2, No. 10, pp. L868–L870, 1986.

[5] X. Li, W. Cai, J. An, S. Kim, J. Nah, D. Yang, R. Piner, A. Velamakanni, I. Jung, E. Tutuc, S. K. Banerjee, L. Colombo, and R. S. Ruoff, “Large-Area Synthesis of High-Quality and Uniform Graphene Films on Copper Foils,” *Science*, vol. 324, no. 5932, pp. 1312–1314, Jun. 2009.

[6] X. Li, C. W. Magnuson, A. Venugopal, R. M. Tromp, J. B. Hannon, E. M. Vogel, L. Colombo, and R. S. Ruoff, “Large-Area Graphene Single Crystals Grown by Low-Pressure Chemical Vapor Deposition of Methane on Copper,” *J. Am. Chem. Soc.*, vol. 133, no. 9, pp. 2816–2819, Mar. 2011.

[7] M. R. Falvo, G. J. Clary, R. M. Taylor, V. Chi, F. P. Brooks, S. Washburn, and R. Superfine, “Bending and buckling of carbon nanotubes under large strain,” *Nature*, vol. 389, no. 6651, pp. 582–584, Oct. 1997.

[8] M. M. Shulaker, G. Hills, N. Patil, H. Wei, H.-Y. Chen, H.-S. P. Wong, and S. Mitra, “Carbon nanotube computer,” *Nature*, vol. 501, no. 7468, pp. 526–530, Sep. 2013.

[9] S. J. Kang, C. Kocabas, T. Ozel, M. Shim, N. Pimparkar, M. A. Alam, S. V. Rotkin, and J. A. Rogers, “High-performance electronics using dense, perfectly aligned arrays of single-walled carbon nanotubes,” *Nat Nano*, vol. 2, no. 4, pp. 230–236, Apr. 2007.

[10] K. S. Kim, Y. Zhao, H. Jang, S. Y. Lee, J. M. Kim, K. S. Kim, J.-H. Ahn, P. Kim, J.-Y. Choi, and B. H. Hong, “Large-scale pattern growth of graphene films for stretchable transparent electrodes,” *Nature*, vol. 457, no. 7230, pp. 706–710, Jan. 2009.

[11] J. Claudon, J. Bleuse, N. S. Malik, M. Bazin, P. Jaffrennou, N. Gregersen, C. Sauvan, P. Lalanne, and J.-M. Gérard, “A highly efficient single-photon source based on a quantum dot in a photonic nanowire,” *Nat Photon*, vol. 4, no. 3, pp. 174–177, Mar. 2010.

[12] J. R. Petta, A. C. Johnson, J. M. Taylor, E. A. Laird, A. Yacoby, M. D. Lukin, C. M. Marcus, M. P. Hanson, and A. C. Gossard, "Coherent Manipulation of Coupled Electron Spins in Semiconductor Quantum Dots," *Science*, vol. 309, no. 5744, pp. 2180–2184, Sep. 2005.

[13] G. Balasubramanian, P. Neumann, D. Twitchen, M. Markham, R. Kolesov, N. Mizuochi, J. Isoya, J. Achard, J. Beck, J. Tissler, V. Jacques, P. R. Hemmer, F. Jelezko, and J. Wrachtrup, "Ultralong spin coherence time in isotopically engineered diamond," *Nat Mater*, vol. 8, no. 5, pp. 383–387, May 2009.

[14] S. A. Cook, "The Complexity of Theorem-proving Procedures," in *Proceedings of the Third Annual ACM Symposium on Theory of Computing*, New York, NY, USA, 1971, pp. 151–158.

[15] L. Fortnow, "The status of the P versus NP problem," *Communications of the ACM*, vol. 52, no. 9, p. 78, Sep. 2009.

[16] R. L. Rivest, A. Shamir, and L. Adleman, "A Method for Obtaining Digital Signatures and Public-key Cryptosystems," *Commun. ACM*, vol. 21, no. 2, pp. 120–126, Feb. 1978.

[17] P. W. Shor, "Polynomial-Time Algorithms for Prime Factorization and Discrete Logarithms on a Quantum Computer," *SIAM Review*, vol. 41, no. 2, pp. 303–332, Jan. 1999.

[18] C. L. Colyer and M. Cocivera, "Thin-Film Cadmium Mercury Telluride Prepared by Nonaqueous Electrodeposition," *J. Electrochem. Soc.*, vol. 139, no. 2, pp. 406–409, Feb. 1992.

[19] L. A. L. De Almeida, G. S. Deep, A. M. N. Lima, I. A. Khrebtov, V. G. Malyarov, and H. Neff, "Modeling and performance of vanadium #x2013;oxide transition edge microbolometers," *Applied Physics Letters*, vol. 85, no. 16, pp. 3605–3607, Oct. 2004.

[20] N. M. Gabor, J. C. W. Song, Q. Ma, N. L. Nair, T. Taychatanapat, K. Watanabe, T. Taniguchi, L. S. Levitov, and P. Jarillo-Herrero, "Hot Carrier–Assisted Intrinsic Photoresponse in Graphene," *Science*, vol. 334, no. 6056, pp. 648–652, Nov. 2011.

[21] S. Piscanec, M. Lazzeri, F. Mauri, and A. C. Ferrari, "Optical phonons of graphene and nanotubes," *Eur. Phys. J. Spec. Top.*, vol. 148, no. 1, pp. 159–170, Sep. 2007.

[22] F. Bonaccorso, Z. Sun, T. Hasan, and A. C. Ferrari, "Graphene photonics and optoelectronics," *Nature Photonics*, vol. 4, no. 9, pp. 611–622, Aug. 2010.

[23] R. Van Noorden, "Production: Beyond sticky tape," *Nature*, vol. 483, no. 7389, pp. S32–S33, Mar. 2012.

[24] F. Kuemmeth, H. O. H. Churchill, P. K. Herring, and C. M. Marcus, "Carbon nanotubes for coherent spintronics," *Materials Today*, vol. 13, no. 3, pp. 18–26, Mar. 2010.

[25] J. H. Hafner, M. J. Bronikowski, B. R. Azamian, P. Nikolaev, A. G. Rinzler, D. T. Colbert, K. A. Smith, and R. E. Smalley, "Catalytic growth of single-wall carbon nanotubes from metal particles," *Chemical Physics Letters*, vol. 296, no. 1–2, pp. 195–202, Oct. 1998.

[26] R. L. Puurunen, "Surface chemistry of atomic layer deposition: A case study for the trimethylaluminum/water process," *Journal of Applied Physics*, vol. 97, no. 12, p. 121301, Jun. 2005.

[27] D. B. Farmer and R. G. Gordon, "Atomic Layer Deposition on Suspended Single-Walled Carbon Nanotubes via Gas-Phase Noncovalent Functionalization," *Nano Lett.*, vol. 6, no. 4, pp. 699–703, Apr. 2006.

[28] X. Wang, S. M. Tabakman, and H. Dai, "Atomic Layer Deposition of Metal Oxides on Pristine and Functionalized Graphene," *J. Am. Chem. Soc.*, vol. 130, no. 26, pp. 8152–8153, Jul. 2008.

[29] X.-H. Zhang, B. Domercq, X. Wang, S. Yoo, T. Kondo, Z. L. Wang, and B. Kippelen, "High-performance pentacene field-effect transistors using Al2O3 gate dielectrics prepared by atomic layer deposition (ALD)," *Organic Electronics*, vol. 8, no. 6, pp. 718–726, Dec. 2007.

[30] J. Kong, N. R. Franklin, C. Zhou, M. G. Chapline, S. Peng, K. Cho, and H. Dai, "Nanotube Molecular Wires as Chemical Sensors," *Science*, vol. 287, no. 5453, pp. 622–625, Jan. 2000.

[31] Z. Zhang, X. Liang, S. Wang, K. Yao, Y. Hu, Y. Zhu, Q. Chen, W. Zhou, Y. Li, Y. Yao, J. Zhang, and L.-M. Peng, "Doping-Free Fabrication of Carbon Nanotube Based Ballistic CMOS Devices and Circuits," *Nano Lett.*, vol. 7, no. 12, pp. 3603–3607, Dec. 2007.

[32] W.-S. Jeon, S. Yang, C. Lee, and S.-W. Kang, "Atomic Layer Deposition of Al2 O 3 Thin Films Using Trimethylaluminum and Isopropyl Alcohol," *J. Electrochem. Soc.*, vol. 149, no. 6, pp. C306–C310, Jun. 2002.

[33] N. Mason, M. J. Biercuk, and C. M. Marcus, "Local Gate Control of a Carbon Nanotube Double Quantum Dot," *Science*, vol. 303, no. 5658, pp. 655–658, Jan. 2004.

[34] B. M. Maune, M. G. Borselli, B. Huang, T. D. Ladd, P. W. Deelman, K. S. Holabird, A. A. Kiselev, I. Alvarado-Rodriguez, R. S. Ross, A. E. Schmitz, M. Sokolich, C. A. Watson, M. F. Gyure, and A. T. Hunter, "Coherent singlet-triplet oscillations in a silicon-based double quantum dot," *Nature*, vol. 481, no. 7381, pp. 344–347, Jan. 2012.

[35] R. Hanson, V. V. Dobrovitski, A. E. Feiguin, O. Gywat, and D. D. Awschalom, "Coherent Dynamics of a Single Spin Interacting with an Adjustable Spin Bath," *Science*, vol. 320, no. 5874, pp. 352–355, Apr. 2008.

[36] F. Kuemmeth, S. Ilani, D. C. Ralph, and P. L. McEuen, "Coupling of spin and orbital motion of electrons in carbon nanotubes," *Nature*, vol. 452, no. 7186, pp. 448–452, Mar. 2008.

[37] I. H. Jafri, H. Busta, and S. T. Walsh, "Critical point drying and cleaning for MEMS technology," 1999, vol. 3880, pp. 51–58.

[38] A. Javey, H. Kim, M. Brink, Q. Wang, A. Ural, J. Guo, P. McIntyre, P. McEuen, M. Lundstrom, and H. Dai, "High-κ dielectrics for advanced carbon-nanotube transistors and logic gates," *Nat Mater*, vol. 1, no. 4, pp. 241–246, Dec. 2002.

[39] L. J. Lauhon, M. S. Gudiksen, D. Wang, and C. M. Lieber, "Epitaxial core–shell and core–multishell nanowire heterostructures," *Nature*, vol. 420, no. 6911, pp. 57–61, Nov. 2002.

[40] W. Lu, J. Xiang, B. P. Timko, Y. Wu, and C. M. Lieber, "One-dimensional hole gas in germanium/silicon nanowire heterostructures," *PNAS*, vol. 102, no. 29, pp. 10046–10051, Jul. 2005.

[41] A. Fuhrer, L. E. Fröberg, J. N. Pedersen, M. W. Larsson, A. Wacker, M.-E. Pistol, and L. Samuelson, "Few Electron Double Quantum Dots in InAs/InP Nanowire Heterostructures," *Nano Lett.*, vol. 7, no. 2, pp. 243–246, Feb. 2007.

[42] S. Roddaro, A. Fuhrer, P. Brusheim, C. Fasth, H. Q. Xu, L. Samuelson, J. Xiang, and C. M. Lieber, "Spin States of Holes in Ge/Si Nanowire Quantum Dots," *Phys. Rev. Lett.*, vol. 101, no. 18, p. 186802, Oct. 2008.

[43] A. V. Khaetskii, D. Loss, and L. Glazman, "Electron Spin Decoherence in Quantum Dots due to Interaction with Nuclei," *Phys. Rev. Lett.*, vol. 88, no. 18, p. 186802, Apr. 2002.

[44] D. R. Lide, *CRC Handbook of Chemistry and Physics, 85th Edition*. CRC Press, 2004.
[45] "Interactive Chart of Nuclides." [Online]. Available: http://www.nndc.bnl.gov/chart/reCenter.jsp?z=60&n=83. [Accessed: 04-Mar-2014].
[46] Y. Hu, H. O. H. Churchill, D. J. Reilly, J. Xiang, C. M. Lieber, and C. M. Marcus, "A Ge/Si heterostructure nanowire-based double quantum dot with integrated charge sensor," *Nat Nano*, vol. 2, no. 10, pp. 622–625, Oct. 2007.
[47] S. Nadj-Perge, S. M. Frolov, E. P. a. M. Bakkers, and L. P. Kouwenhoven, "Spin-orbit qubit in a semiconductor nanowire," *Nature*, vol. 468, no. 7327, pp. 1084–1087, Dec. 2010.
[48] K. D. Petersson, C. G. Smith, D. Anderson, P. Atkinson, G. A. C. Jones, and D. A. Ritchie, "Charge and Spin State Readout of a Double Quantum Dot Coupled to a Resonator," *Nano Lett.*, vol. 10, no. 8, pp. 2789–2793, Aug. 2010.
[49] D. J. Wilson, C. A. Regal, S. B. Papp, and H. J. Kimble, "Cavity Optomechanics with Stoichiometric SiN Films," *Phys. Rev. Lett.*, vol. 103, no. 20, p. 207204, Nov. 2009.
[50] J. D. Thompson, B. M. Zwickl, A. M. Jayich, F. Marquardt, S. M. Girvin, and J. G. E. Harris, "Strong dispersive coupling of a high-finesse cavity to a micromechanical membrane," *Nature*, vol. 452, no. 7183, pp. 72–75, Mar. 2008.
[51] P.-L. Yu, T. P. Purdy, and C. A. Regal, "Control of Material Damping in High-Q Membrane Microresonators," *Phys. Rev. Lett.*, vol. 108, no. 8, p. 083603, Feb. 2012.
[52] A. Venugopal, L. Colombo, and E. M. Vogel, "Contact resistance in few and multilayer graphene devices," *Applied Physics Letters*, vol. 96, no. 1, p. 013512, Jan. 2010.
[53] S. Schmid, K. D. Jensen, K. H. Nielsen, and A. Boisen, "Damping mechanisms in high-Q micro and nanomechanical string resonators," *Phys. Rev. B*, vol. 84, no. 16, p. 165307, Oct. 2011.
[54] S. Schmid, C. Hierold, and A. Boisen, "Modeling the Kelvin polarization force actuation of micro- and nanomechanical systems," *Journal of Applied Physics*, vol. 107, no. 5, p. 054510, Mar. 2010.
[55] J. M. Taylor, A. S. Sørensen, C. M. Marcus, and E. S. Polzik, "Laser Cooling and Optical Detection of Excitations in a LC Electrical Circuit," *Phys. Rev. Lett.*, vol. 107, no. 27, p. 273601, Dec. 2011.
[56] T. Mueller, F. Xia, and P. Avouris, "Graphene photodetectors for high-speed optical communications," *Nat Photon*, vol. 4, no. 5, pp. 297–301, May 2010.
[57] M. C. Lemme, F. H. L. Koppens, A. L. Falk, M. S. Rudner, H. Park, L. S. Levitov, and C. M. Marcus, "Gate-Activated Photoresponse in a Graphene p–n Junction," *Nano Lett.*, vol. 11, no. 10, pp. 4134–4137, Oct. 2011.
[58] F. Xia, T. Mueller, Y. Lin, A. Valdes-Garcia, and P. Avouris, "Ultrafast graphene photodetector," *Nat Nano*, vol. 4, no. 12, pp. 839–843, Dec. 2009.
[59] S. M. Sze and K. K. Ng, *Physics of Semiconductor Devices*. John Wiley & Sons, 2006.
[60] C. R. Dean, A. F. Young, I. Meric, C. Lee, L. Wang, S. Sorgenfrei, K. Watanabe, T. Taniguchi, P. Kim, K. L. Shepard, and J. Hone, "Boron nitride substrates for high-quality graphene electronics," *Nat Nano*, vol. 5, no. 10, pp. 722–726, Oct. 2010.
[61] J. C. W. Song, M. S. Rudner, C. M. Marcus, and L. S. Levitov, "Hot Carrier Transport and Photocurrent Response in Graphene," *Nano Lett.*, vol. 11, no. 11, pp. 4688–4692, Nov. 2011.
[62] S. Bhaviripudi, X. Jia, M. S. Dresselhaus, and J. Kong, "Role of Kinetic Factors in Chemical Vapor Deposition Synthesis of Uniform Large Area Graphene Using Copper Catalyst," *Nano Lett.*, vol. 10, no. 10, pp. 4128–4133, Oct. 2010.

[63] J. R. Williams, L. DiCarlo, and C. M. Marcus, "Quantum Hall Effect in a Gate-Controlled p-n Junction of Graphene," *Science*, vol. 317, no. 5838, pp. 638–641, Aug. 2007.
[64] E. J. H. Lee, K. Balasubramanian, R. T. Weitz, M. Burghard, and K. Kern, "Contact and edge effects in graphene devices," *Nature Nanotechnology*, vol. 3, no. 8, pp. 486–490, 2008.
[65] B. G. Lee, M. A. Belkin, R. Audet, J. MacArthur, L. Diehl, C. Pflügl, F. Capasso, D. C. Oakley, D. Chapman, A. Napoleone, D. Bour, S. Corzine, G. Höfler, and J. Faist, "Widely tunable single-mode quantum cascade laser source for mid-infrared spectroscopy," *Applied Physics Letters*, vol. 91, no. 23, p. 231101, Dec. 2007.
[66] A. Rogalski, *Infrared Detectors*. CRC Press, 2000.
[67] M. Liu, X. Yin, E. Ulin-Avila, B. Geng, T. Zentgraf, L. Ju, F. Wang, and X. Zhang, "A graphene-based broadband optical modulator," *Nature*, vol. 474, no. 7349, pp. 64–67, May 2011.
[68] T. Mueller, F. Xia, and P. Avouris, "Graphene photodetectors for high-speed optical communications," *Nature Photonics*, vol. 4, no. 5, pp. 297–301, Mar. 2010.
[69] X. Xu, N. M. Gabor, J. S. Alden, A. M. van der Zande, and P. L. McEuen, "Photo-Thermoelectric Effect at a Graphene Interface Junction," *Nano Lett.*, vol. 10, no. 2, pp. 562–566, Feb. 2010.
[70] F. Wang, Y. Zhang, C. Tian, C. Girit, A. Zettl, M. Crommie, and Y. R. Shen, "Gate-Variable Optical Transitions in Graphene," *Science*, vol. 320, no. 5873, pp. 206–209, Apr. 2008.
[71] Z. Q. Li, E. A. Henriksen, Z. Jiang, Z. Hao, M. C. Martin, P. Kim, H. L. Stormer, and D. N. Basov, "Dirac charge dynamics in graphene by infrared spectroscopy," *Nat Phys*, vol. 4, no. 7, pp. 532–535, Jul. 2008.
[72] J. Chen, M. Badioli, P. Alonso-González, S. Thongrattanasiri, F. Huth, J. Osmond, M. Spasenović, A. Centeno, A. Pesquera, P. Godignon, A. Zurutuza Elorza, N. Camara, F. J. G. de Abajo, R. Hillenbrand, and F. H. L. Koppens, "Optical nano-imaging of gate-tunable graphene plasmons," *Nature*, vol. advance online publication, Jun. 2012.
[73] Z. Fei, A. S. Rodin, G. O. Andreev, W. Bao, A. S. McLeod, M. Wagner, L. M. Zhang, Z. Zhao, M. Thiemens, G. Dominguez, M. M. Fogler, A. H. C. Neto, C. N. Lau, F. Keilmann, and D. N. Basov, "Gate-tuning of graphene plasmons revealed by infrared nano-imaging," *Nature*, vol. 487, no. 7405, pp. 82–85, Jul. 2012.
[74] M. Jablan, H. Buljan, and M. Soljačić, "Plasmonics in graphene at infrared frequencies," *Phys. Rev. B*, vol. 80, no. 24, p. 245435, Dec. 2009.
[75] J. Yan, M.-H. Kim, J. A. Elle, A. B. Sushkov, G. S. Jenkins, H. M. Milchberg, M. S. Fuhrer, and H. D. Drew, "Dual-gated bilayer graphene hot-electron bolometer," *Nature Nanotechnology*, vol. 7, no. 7, pp. 472–478, Jun. 2012.
[76] K. C. Fong and K. C. Schwab, "Ultrasensitive and Wide-Bandwidth Thermal Measurements of Graphene at Low Temperatures," *Phys. Rev. X*, vol. 2, no. 3, p. 031006, Jul. 2012.
[77] L. Vicarelli, M. S. Vitiello, D. Coquillat, A. Lombardo, A. C. Ferrari, W. Knap, M. Polini, V. Pellegrini, and A. Tredicucci, "Graphene field-effect transistors as room-temperature terahertz detectors," *Nat Mater*, vol. 11, no. 10, pp. 865–871, Oct. 2012.
[78] G. Konstantatos, M. Badioli, L. Gaudreau, J. Osmond, M. Bernechea, F. P. G. de Arquer, F. Gatti, and F. H. L. Koppens, "Hybrid graphene-quantum dot phototransistors with ultrahigh gain," *Nat Nano*, vol. 7, no. 6, pp. 363–368, Jun. 2012.

[79] B. Y. Zhang, T. Liu, B. Meng, X. Li, G. Liang, X. Hu, and Q. J. Wang, "Broadband high photoresponse from pure monolayer graphene photodetector," *Nat Commun*, vol. 4, p. 1811, May 2013.
[80] R. S. Balcerak, "Uncooled infrared sensors: rapid growth and future perspective," in *Proc. of SPIE*, 2000, vol. 4028, pp. 36–39.
[81] J. R. Williams, L. DiCarlo, and C. M. Marcus, "Quantum Hall Effect in a Gate-Controlled p-n Junction of Graphene," *Science*, vol. 317, no. 5838, pp. 638–641, Aug. 2007.
[82] B. Özyilmaz, P. Jarillo-Herrero, D. Efetov, D. A. Abanin, L. S. Levitov, and P. Kim, "Electronic Transport and Quantum Hall Effect in Bipolar Graphene p-n-p Junctions," *Phys. Rev. Lett.*, vol. 99, no. 16, p. 166804, Oct. 2007.
[83] B. Huard, J. A. Sulpizio, N. Stander, K. Todd, B. Yang, and D. Goldhaber-Gordon, "Transport Measurements Across a Tunable Potential Barrier in Graphene," *Phys. Rev. Lett.*, vol. 98, no. 23, p. 236803, Jun. 2007.
[84] Y. M. Zuev, W. Chang, and P. Kim, "Thermoelectric and Magnetothermoelectric Transport Measurements of Graphene," *Phys. Rev. Lett.*, vol. 102, no. 9, p. 096807, Mar. 2009.
[85] N. W. Ashcroft and N. D. Mermin, *Solid state physics*. Saunders College, 1976.
[86] A. A. Balandin, S. Ghosh, W. Bao, I. Calizo, D. Teweldebrhan, F. Miao, and C. N. Lau, "Superior Thermal Conductivity of Single-Layer Graphene," *Nano Lett.*, vol. 8, no. 3, pp. 902–907, 2008.
[87] S. Chen, Q. Wu, C. Mishra, J. Kang, H. Zhang, K. Cho, W. Cai, A. A. Balandin, and R. S. Ruoff, "Thermal conductivity of isotopically modified graphene," *Nature Materials*, vol. 11, no. 3, pp. 203–207, 2012.
[88] E. Pop, V. Varshney, and A. K. Roy, "Thermal properties of graphene: Fundamentals and applications," *MRS Bulletin*, vol. 37, no. 12, pp. 1273–1281, 2012.
[89] E. Palik, *Handbook of Optical Constants of Solids*. Elsevier, 1998.
[90] I. Stark, M. Stordeur, and F. Syrowatka, "Thermal conductivity of thin amorphous alumina films," *Thin Solid Films*, vol. 226, no. 1, pp. 185–190, Apr. 1993.
[91] R. Sultan, A. D. Avery, G. Stiehl, and B. L. Zink, "Thermal conductivity of micromachined low-stress silicon-nitride beams from 77 to 325 K," *Journal of Applied Physics*, vol. 105, no. 4, pp. 043501–043501–7, Feb. 2009.
[92] G. Eda, G. Fanchini, and M. Chhowalla, "Large-area ultrathin films of reduced graphene oxide as a transparent and flexible electronic material," *Nat Nano*, vol. 3, no. 5, pp. 270–274, May 2008.
[93] H. C. Ko, M. P. Stoykovich, J. Song, V. Malyarchuk, W. M. Choi, C.-J. Yu, J. B. Geddes Iii, J. Xiao, S. Wang, Y. Huang, and J. A. Rogers, "A hemispherical electronic eye camera based on compressible silicon optoelectronics," *Nature*, vol. 454, no. 7205, pp. 748–753, Aug. 2008.
[94] P. B. Chu, J. T. Chen, R. Yeh, G. Lin, J. C. P. Huang, B. A. Warneke, and K. S. J. Pister, "Controlled pulse-etching with xenon difluoride," in *, 1997 International Conference on Solid State Sensors and Actuators, 1997. TRANSDUCERS '97 Chicago*, 1997, vol. 1, pp. 665–668 vol.1.